COVER PAGE

Federal Agency to which Report is submitted: DOE NE – Nuclear Energy University Program

Recipient: University of Florida

Award Number: DE-NE0000731

Project Title: Innovative coating of nanostructured vanadium carbide on the F/M cladding tube inner surface for mitigating the fuel cladding chemical interactions

Project Period: Jan 2014 to Aug 31 2017

Principle Investigator: Yong Yang, University of Florida, yongyang@ufl.edu, 352-846-3791

Report Submitted by: Yong Yang, University of Florida

Date of Report: 11/29/2017

Covering Period: Jan 15, 2015 -Aug 31, 2017

Report Frequency: Final

Collaborator: Simon Phillpot, University of Florida, sphil@mse.ufl.edu

Cost-Sharing Partners: NA

DOE Project Team: DOE TPOC – James Cole

DOE Federal Reviewer –

Signature of Submitting Official:

(Electronic signature is acceptable)

Executive Summary/Abstract

Fuel cladding chemical interactions (FCCI) have been acknowledged as a critical issue in a metallic fuel/steel cladding system due to the formation of low melting intermetallic eutectic compounds between the fuel and cladding steel, resulting in reduction in cladding wall thickness as well as a formation of eutectic compounds that can initiate melting in the fuel at lower temperature. In order to mitigate FCCI, diffusion barrier coatings on the cladding inner surface have been considered. In order to generate the required coating techniques, pack cementation, electroplating, and electrophoretic deposition have been investigated. However, these methods require a high processing temperature of above 700 °C, resulting in decarburization and decomposition of the martensites in a ferritic/martensitic (F/M) cladding steel. Alternatively, organometallic chemical vapor deposition (OMCVD) can be a promising process due to its low processing temperature of below 600 °C.

The aim of the project is to conduct applied and fundamental research towards the development of diffusion barrier coatings on the inner surface of F/M fuel cladding tubes. Advanced cladding steels such as T91, HT9 and NF616 have been developed and extensively studied as advanced cladding materials due to their excellent irradiation and corrosion resistance. However, the FCCI accelerated by the elevated temperature and high neutron exposure anticipated in fast reactors, can have severe detrimental effects on the cladding steels through the diffusion of Fe into fuel and lanthanides towards into the claddings. To test the functionality of developed coating layer, the diffusion couple experiments were focused on using T91 as cladding and Ce as a surrogate lanthanum fission product.

By using the customized OMCVD coating equipment, thin and compact layers with a few micron between 1.5 μm and 8 μm thick and average grain size of 200 nm and 5 μm were successfully obtained at the specimen coated between 300°C and 500 °C, respectively. The coating layer contains both carbon and vanadium elements as quantified by WED, and the phases mainly consist of a mixture of V_2C and VC, which was confirmed using X-ray diffraction patterns. In addition, the ratio between V and C varies with processing temperature, and it was observed that a higher temperature promotes the carbon adsorption and increases thickness of the coating. With optimized deposition conditions, we can apply the coating technique toward the actual T91 cladding materials, and provide the possibilities for the real application in sodium-cooled fast reactors (SFRs).

Diffusion couple experiments were performed at both 550 °C and 690 °C, which corresponds to normal and aggressive operating temperatures, respectively. The results show that vanadium carbide coating with wider thickness (8 μm) and lower carbon concentration (27 at.%) reduced

the width of the inter diffusion region, indicating that vanadium carbide coating can mitigate FCCI effectively. In specific, inter-diffusion between Fe and Ce was prohibited over most area, but Ce diffusion occurred toward the coating and the Fe substrate through thinner coating layer, which needs further optimization in terms of uniform coating thickness. Overall, it is concluded that this coating process can be successfully applied onto the inner surface of HT9 cladding tubes and the FCCI can be effectively mitigated if not totally eliminated.

For the part of atomistic modeling, self-diffusion and impurity diffusion behavior of vanadium carbide was modeled using static density functional theory calculations. Three ordered structures were chosen to represent the V_2C coating: two ordered phases α-V_2C and β'-V_2C known experimentally and a low-energy ordered V_2C structure predicted by first-principles calculations. The structural, electronic and elastic properties of the three structures are calculated and compared to available experimental and theoretical data. Data from experiments suggest that carbon and vanadium diffuse separately on each respective sub-lattice. Vanadium is expected to diffuse via a standard vacancy-assisted mechanism, whereas an abundance of structural vacancies on the carbon sub-lattice suggests an interstitial mechanism for carbon. Minimum energy pathways (MEPs) for jumps to nearest-neighbor sites are calculated for each mechanism using the climbing image nudged elastic band (CI-NEB) method. Self-diffusion coefficients were then calculated using expressions derived from transition state theory. Entropic contributions to the free energies from phonons were calculated within the harmonic approximation; entropic contributions from thermal excitation of electrons are ignored as they are expected to be minor. Theoretical activation energies and diffusion prefactors for self-diffusion in V_2C were compared to available experimental data. Impurity diffusion behavior was investigated for Fe and Ni representing major components of the cladding, U representing a major component of the fuel and Ce and Nd representing typical fission products. Defect formation energies are calculated for both substitutional and interstitial impurities to determine site preference. It was found that all impurity atoms prefer substitutional sites and, therefore, should diffuse through the vanadium sub-lattice by a vacancy-assisted mechanism. MEPs for jumps to nearest-neighbor sites were calculated for each impurity species using the CI-NEB method. The resultant transition states were used to estimate activation energies for impurity diffusion for each of the three ordered V_2C structures.

Table of Contents

1. Introduction and Research Motivation

Metallic fuels are being considered as a fuel form for the sodium-cooled fast reactors (SFRs) because of their high thermal conductivity, proliferation resistance, good compatibility with sodium, and ease of fabrication. In conjunction with the fuel, ferritic/martensitic (F/M) steels are candidate materials for fuel cladding [1, 2]. HT9, for example, allows for fuel burnups greater than 200 GWd/MTHM (or 20 at.%). A crucial concern, however, is the reaction between actinide elements in a metallic fuel such as U and Pu, and the inner surface of the F/M steel cladding [2, 3]. This phenomenon is known as Fuel Chemical-Cladding Interaction (FCCI), and is accompanied by the formation of lower melting point eutectic compounds at above 650°C in the U-Pu-Fe system and 725 °C in the U-Fe system. Additionally, FCCI reduces the effective cladding thickness so that the mechanical integrity of the cladding gradually decreases as burnup increases. The fuel cladding inter-diffusion can eventually result in the changes in heat transfer characteristics and the failure of cladding with further breach of fuel into the coolant. In the past four decades, both out-of-pile diffusion couples and in-pile irradiation experiments have been extensively performed to study the mechanism of FCCI. As reported by Hofman [4], for the U-19Pu-10Zr/HT9 diffusion couples, at temperatures above 725°C, several levels of interaction were observed, ranging from incipient molten phase formation to complete melting of fuel and part of the steel in some diffusion couples at temperatures above 800°C. Figure 1-1 shows cross-sectional photomicrographs of a metallic fuel pin before and after irradiation. The image on right reveals the formation of low-meting phase, and the right one shows the chemical interaction between the fuel-cladding and rare-earth fission products along with plutonium. It also shows that the initial 600μm radial gap had completely closed due to the fuel swelling from large fission-gas bubbles, which can further accelerate the FCCI as the direct physical contacts were established [5].

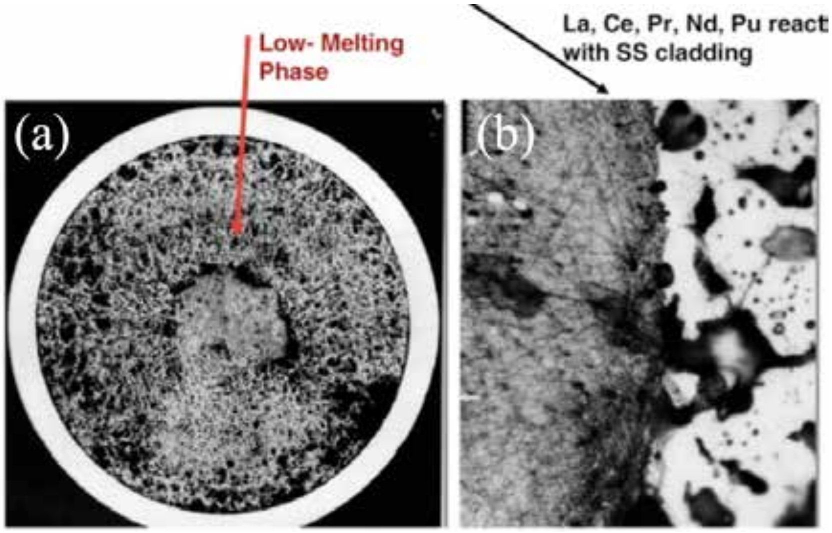

Figure 1-1. Photomicrographs of SFR fuel after irradiation (a) cross-section image with low-melting phase in the fuel (b) high magnification image between fuel and the cladding [5].

Early diffusion tests of Pu containing fuels and austenitic stainless steel identified Zr as an effective alloying addition to prevent formation of the low melting-point phase in the diffusion zone. The selection of the present U-Pu-Zr fuel composition is based on reported work and additional irradiation tests [6]. The role of Zr in raising the temperatures at which the molten phases form well above those of U-Pu-Fe (Ni) eutectic compositions is clear. Moreover, the diffusion of Fe and Ni into the fuel no longer presents a problem because the presence of Zr in the fuel prevents the formation of the low melting eutectic composition. However, the extent of diffusion of Pu and other fission products into the steel cladding without accompanying diffusion of Zr is the key problem in fuel-cladding compatibility. One possible solution to minimizing the FCCI is to place a physical barrier between the fuel and cladding. Such a barrier material has to be unsusceptible to interaction at both the fuel and cladding interface. By using V or Zr, which have good neutronic characteristics, no low melting phases would form between the fuel or fission products and the cladding constituents, based on binary phase diagrams. The diffusion couple experiments performed by Keiser, et al. [7, 8] at 700°C using a cast U-based alloy with added fission products show that both V and Zr appear to be good candidate materials to serve as barriers to FCCI in metallic fuels, while the V diffusion couple has an interdiffusion zone of around 10µm, which is twelve times less than that of fuel/Zr couple, as shown in Figure 1-2. Additionally, in-reactor tests conducted by Argonne in the 1960's also indicated that vanadium alloy cladding had excellent metallurgical compatibility with U-Pu-Zr alloys.

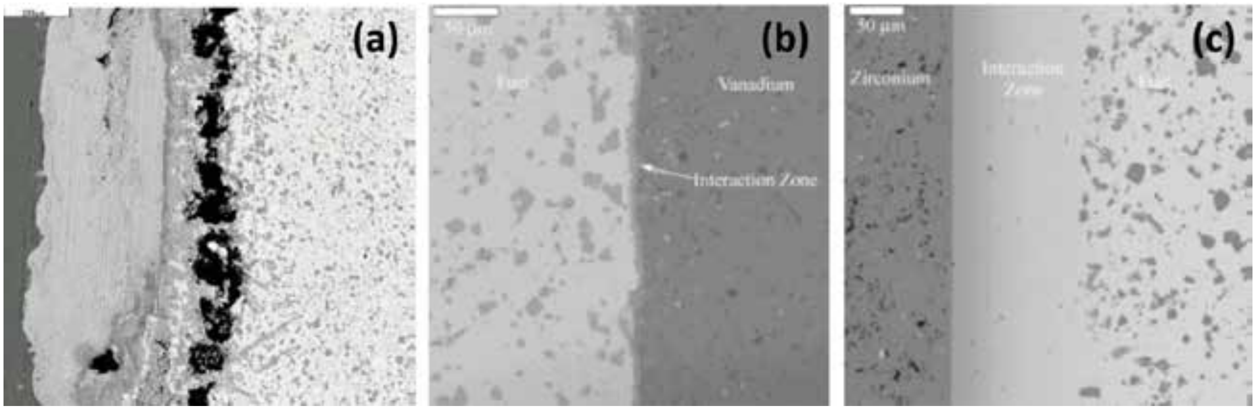

Figure 1-2. Interdiffusion zones formed between the fuel doped with fission products with (a) ODS, (b) Vanadium and (C) Zirconium, respectively [7, 8].

There may be several methods by which a vanadium barrier can be placed between the fuel and cladding, e.g., casting the fuel into a mold of the barrier material and then placing the casting and the mold into the steel cladding, and electro-spark depositing a coating layer directly on the surface of fuel slug. While those methods might have been expected to have some significant advantages, they did not prove to provide an effective barrier for fuel/cladding interaction. More recently, strategies are mainly focusing on producing a lined or "duplex" cladding and placing the cast fuel ingot into the duplex cladding [9, 10]. In such a structure, the lining layer has to be thin and compact to minimize the temperature gradient across the coating-cladding system. Currently, the fabrication of this thin liner is being developed using a cold-drawing technology along with intermediate annealing; using this approach, an average thickness of ~85µm has been achieved [10]. Diffusion bonded interfaces and gaps were observed between the cladding and the liner. For heat transfer purposes, the spacing between the vanadium and cladding has to be minimized, because a large gap could lead to unacceptably high fuel temperatures with consequent unsatisfactory fuel performance. There are additional structural processes that have to be considered, including microstructural changes from decarburization of cladding adjacent to the liner interface, grain growth, carbide precipitation, and decomposition of tempered martensite.

In addition to vanadium or vanadium alloys, it has been speculated that vanadium carbide could also function effectively as a FCCI barrier since vanadium acts as an inhibitor for stopping the inter-diffusion between fuel and cladding steel. The decarburization of the cladding could potentially be eliminated since the pre-existing carbon in vanadium carbide would limit the diffusion of carbon from martensitic substrate into coating layer. At the operating temperature and oxygen partial pressure of metal fuel in a SFR, vanadium carbide is stable from aggressive oxidation and can inhibit the steel claddings from scavenging oxygen. Our preliminary study using a pack cementation diffusion coating (PCDC) technique shows that a thin vanadium rich layer, which was lately proved to be vanadium carbide (V_2C), can be successfully deposited on the inner wall of the cladding tube. The diffusion couple experiments between cerium and coated/uncoated HT9 steels demonstrate that vanadium carbide is extremely effective for mitigating the FCCI, as shown in the Figure 1-3. The V_2C with a thickness of ~1.7µm can prevent the inter-diffusion between HT9 substrate and cerium annealed at 650°C for 100 hours. The EDS line-scan results in Figure 1-4 shows that there was no Fe or Ce in the V_2C coating layer of diffusion couple.

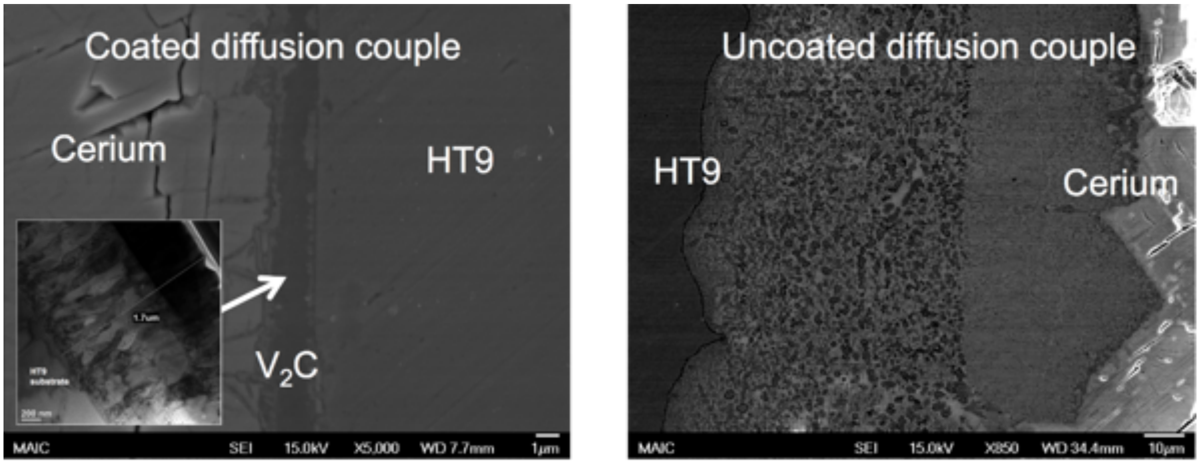

Figure 1-3. Comparison between the diffusion couples of coated HT9/Cerium and uncoated HT9/Cerium annealed at 650°C for 100 hours.

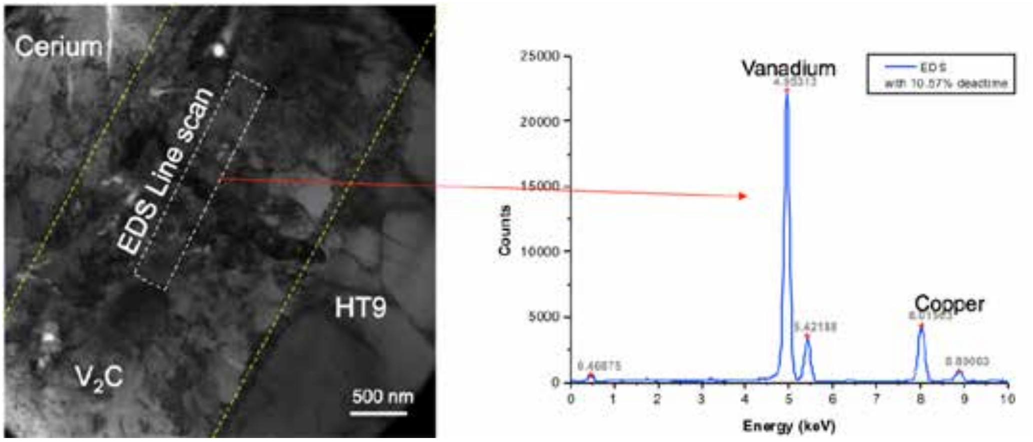

Figure 1-4. EDS/STEM line-scan over the V_2C coating layer in a diffusion couple.

Unfortunately, this pack cementation coating method can only work in practice at a temperature above 730°C and a growth rate of less than 0.1μm/hour, which significantly promotes the decarburization (Figure 1-5, [11]) and decomposition of martensitic microstructure [12]. Other chemical vapor deposition techniques (CVD, LCVD or PCVD) commonly used for producing vanadium carbide from a gas mixture of hydrogen, methane and vanadium chloride also generally require a high processing temperature (800-1200°C), at which the martensitic microstructure of F/M claddings will decompose and decarburization can take place. Moreover, the high aspect ratio geometry of long and thin cladding tube (>4' length and 0.18" ID) presents a significant practical challenge for conventional CVD coating processes. Therefore, an alternative coating process that can keep processing temperature below 650 ^{o}C is crucial. A low temperature organometallic CVD (OMCVD) process, which uses a less stable organometallic precursor that decomposes into vanadium carbide at a lower temperature, offers this possibility.

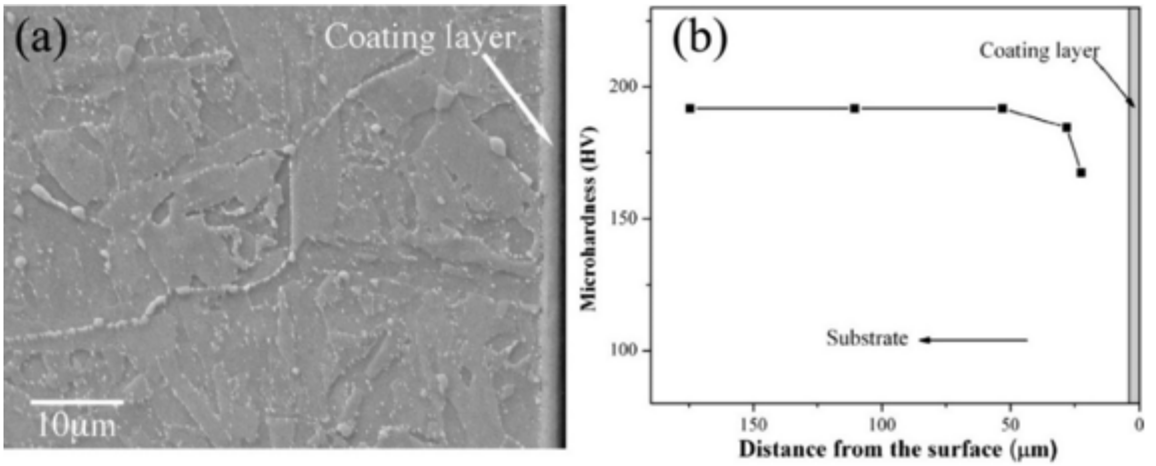

Figure 1-5. (a) SEM image of the HT9 substrate and (b) micro-hardness measurements on the HT9 substrate after diffusion coating process at 730 °C for 120 h [11].

2. Scientific Approach

2.1. Advantage of Organo-Metallic Chemical Vapor Deposition (OMCVD)

The low temperature deposition process can be achieved in a conventional CVD apparatus if using less stable precursors such as organometallic compounds. This process is known as the Organo-metallic chemical vapor deposition (OMCVD). The OMCVD is a technique that is used to deposit very thin layers of atoms onto a substrate. To deposit the thin films, the precursors are vaporized and transported into the reactor together with other gases. In there, the critical chemical reaction takes place that turns the precursors into the desired crystal structures through thermal decomposition. The precursor for low temperature CVD deposition of vanadium carbide is very rare, and only dicyclopentadienyl vanadium (vanadocene or Cp_2V) was reported to decompose into V_4C_3 at temperatures as low as 400°C [13]. Cp_2V will be an ideal precursor for this development and it is commercially available or can be readily made in our research lab. Compared with mechanical lining and conventional CVD technologies, the proposed low temperature process can offer several advantages: i) no significant residual stress or axial texture from cold-drawing; ii) no detrimental effects on the martensitic substrate, and iii) a strongly bonded thin and uniform vanadium carbide coating can be readily obtained. In addition, as compared with the PCDC method [11], the grain structures are expected to be more equiaxed, which is beneficial for eliminating the possible fast diffusion paths from columnar grain boundaries.

2.2. Fundamentals of OMCVD

Thermal decomposition (pyrolysis) is the primary mechanism for the OMCVD process using metal organic precursors. Figure 2-1 shows a schematic illustration of the key OMCVD steps during deposition. In general, the CVD process involves the following key steps [14]:

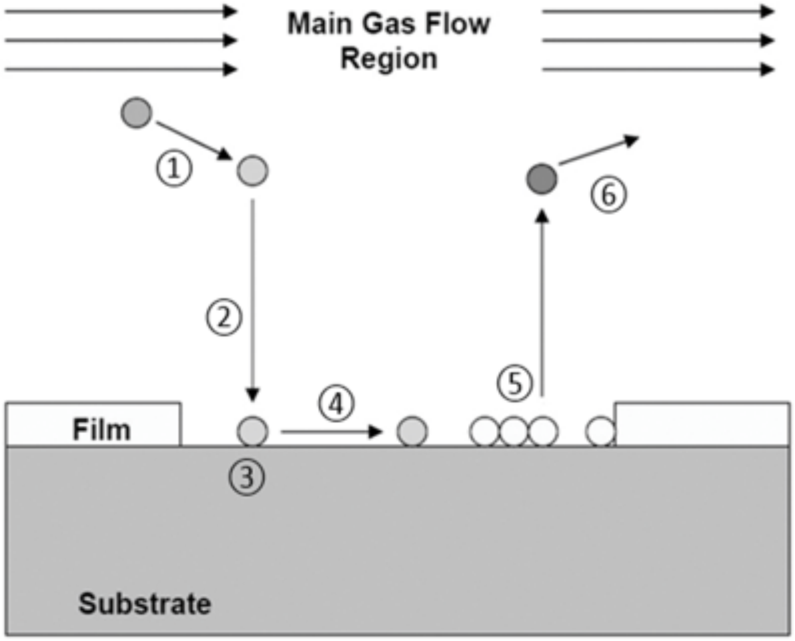

Figure 2-1. A schematic illustration of the key CVD steps during deposition.

(1) Generation of active gaseous reactant species, and transportation of the gaseous species into the reaction chamber.
(2) Transportation of the gaseous reactants onto the surface.
(3) Absorption of gaseous reactants onto the heated substrate, and the heterogeneous reaction occurs at the heated substrate which produces the deposit and by-product species.
(4) The deposits will diffuse along the heated substrate surface forming the crystallization and growth of the coating.
(5) Gaseous by-products are removed from the boundary layer through diffusion (desorption).
(6) The unreacted gaseous precursors and by-products will be transported away from the deposition chamber.

2.3. Factors that Influence on the Deposition Process

Among the numerous factors that may have significant influence on the deposition process, the temperature of the substrate is one of the most important CVD parameters and is of special interest in the case of the use of organometallic precursors. In addition, based on the observations from Poirier [13], there are more experimental parameters that need to be precisely controlled, including the hydrogen carrier gas flow rate, evaporating temperature of the precursor, and the partial pressure of Cp_2V vapor near the substrate surface. As a result, the deposition rate, grain size and composition of the coating can be manipulated.

2.4. Inter-Diffusion Study

The occurrence of composition-dependent diffusivities is encountered in many practical diffusion problems. The fuel-cladding system in a fast reactor is a great example since it involves multiple elements and high temperatures. Inter-diffusion between fuel and cladding is often affected by compositional formation (e.g. eutectic phases or precipitations). In this project, inter-diffusion between the F/M steels and lanthanide fission products are of the primary interest. The closed-form expression for inter-diffusion coefficients could be derived by using the Dayananda's formulism of Fick's second law. The corresponding diffusion coefficients were calculated using the following equation [15]:

$$\mathrm{x} = \sqrt{2Dt}$$

where x is the diffusion length, D is the diffusion coefficient, and t is the total annealing time. Diffusion couple experiments were widely performed in the past, to study the inter-diffusion and intermetallic formation between lanthanides (or actinides) and the claddings [11, 15, 16]. The experimental data was fit to an Arrhenius relationship given by the following equation:

$$\mathrm{D} = D_0 \times exp\frac{-E_a}{kT}$$

where D is the diffusion coefficient, D_0 is the diffusivity, E_a is the activation energy, k is Boltzmann's constant, and T is the absolute temperature.

3. Proposed Scope of the Present Project

The goal of the proposed project is to conduct applied and fundamental research towards the development of diffusion barrier coatings on the inner surface of F/M fuel cladding tubes. Advanced cladding steels such as T91, HT9 and NF616 have been developed and extensively studied as advanced cladding materials due to their excellent irradiation and corrosion resistance. However, the FCCI accelerated by the elevated temperature and high neutron exposure anticipated in fast reactors, can have severe detrimental effects on the cladding steels through the diffusion of Fe and Ni into fuel and lanthanides towards into the claddings. For this proposed study, the diffusion couple experiments will be focused on T91, NF616 and HT9 for clad, and both surrogate and uranium bearing fuel.

The proposed work is aimed at developing a low temperature coating process using organometallic precursor, vanadocene Cp_2V ($Cp=C_5H_5$). An innovative coating setup will be built to deposit a uniform nanostructured vanadium carbide layer (less than 10μm in thickness and nano-sized grain structure) on the inner surface of long F/M cladding tube. Compared with mechanical lining and conventional CVD technologies, the proposed low temperature process can offer several advantages: 1) no significant residual stress or axial texture from cold-drawing, 2) no detrimental effects on the martensitic substrate, and 3) a strongly bonded thin and uniform vanadium carbide coating can be readily obtained. The functionality of the coating as FCCI barrier will be examined experimentally using diffusion couple tests (e.g. cerium). These results will provide benchmark against to which compare atomistic modeling. Even though vanadium carbide has been identified as one of most effective FCCI barrier element, the fundamental underlying mechanisms have not been fully understood. The proposed atomistic modeling will help understand these fundamentals processed.

4. Experimental System Set Up Used in the Present Project

The low temperature CVD system set for this research consists of three main components: the CVD reaction chamber, a chemical vapor precursor supply system, and an effluent gas handling system. Figure 4-1 shows the schematic set up of the low temperature OMCVD coating system.

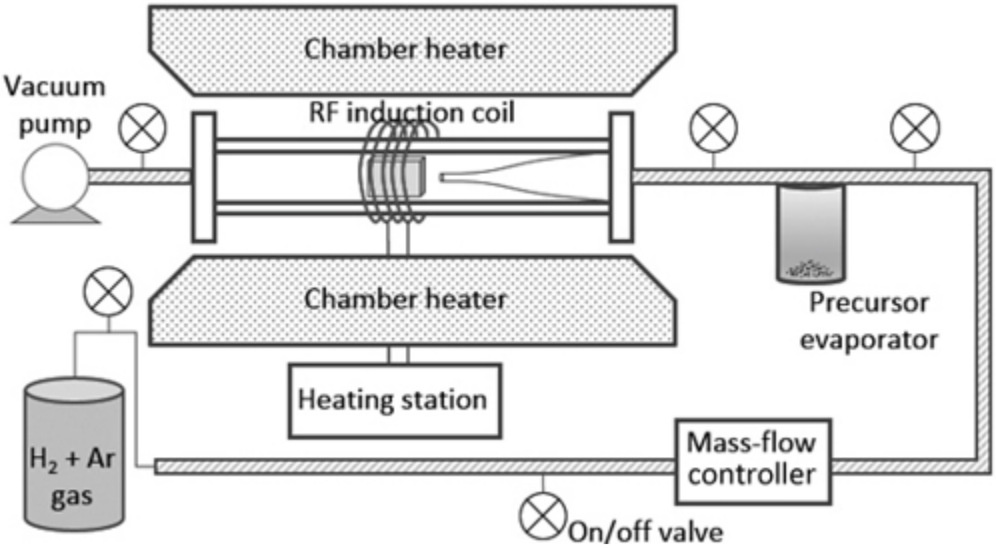

Figure 4-1. Schematic set up for low temperature CVD system on the T91 flat coupon specimen.

4.1. Induction Power Supply Equipped with a Remote Workhead

A new induction power supply equipped with remote workhead and cooling reservoir with a pump was installed as well as an infrared temperature detector, Pirani pressure sensor, flow meter, and the safety shut off mechanism that is controlled by a programmable device. Since the materials to be coated are ferromagnetic Fe based steels, a radio-frequency (RF) induction heater can be easily used to raise the substrate temperature by eddy current heating. After a few initial experiments a proper induction power supply (Ambrell, EASYHEAT 0112 bench model) equipped with remote workhead (Ambrell, EASYHEAT model 150) was installed along with the required data acquisition system. This induction power supply has 1.2 kW output and frequencies of a range from 150 to 400 kHz. In order to verify the performance of the system, a single layer split coil was used to generate the required heating the application. Initial tests were conducted to optimize the power delivered to the part. The part was simply placed into the coil and the power was turned on. A temperature controller unit (Yokogawa, UT55A) was used to raise to a desired temperature (Figure 4-2). The test result shows that the specimen can be heated to 600 ^{o}C in 10 seconds or less using the 1.2 kW power supply at frequency of 267 kHz.

Therefore, it is confirmed the heating process for heating F/M steel specimen to 600 °C for my application using a solid-state induction power supply is feasible.

Figure 4-2. Heating application laboratory test with F/M steel using induction power supply, 3-turn helical coil, and a temperature controller.

4.2. Temperature Measurement on the T91 Sample

To control the sample substrate temperature using an infra-thermometer, the calculation of a sample surface emissivity needs to be performed. The calibration was conducted in the following procedure. Sample was heat up using a heat plate, and the surface temperature of the sample was detected by using infrared (IR) thermometer as well as a k-type thermo couple. As the distance between IR detector and surface of the specimen is a critical factor that affects the emissivity, the distance was set to be the same as that of real coating processing. Emissivity of the IR pyrometer was adjusted in the control panel so that the temperature reading from IR pyrometer matches that from K type thermo couple. The emissivity was calibrated in this way. The emissivity calibration on T91 sample was conducted. As shown in Figure 4-3, a glass mount was constructed to filter the radiation heat emitted from the plate heater. The pyrometer was mounted at < 5 inches above the T91 substrate at a normal angle. The emissivity is plotted in Figure 4-4 as a function of temperature for the as-polished T91 substrate. A similar calibration was also performed for the substrate after being coated with vanadium carbide, and a slightly high emissivity was observed as compared with uncoated substrate, as shown in Figure 4-5.

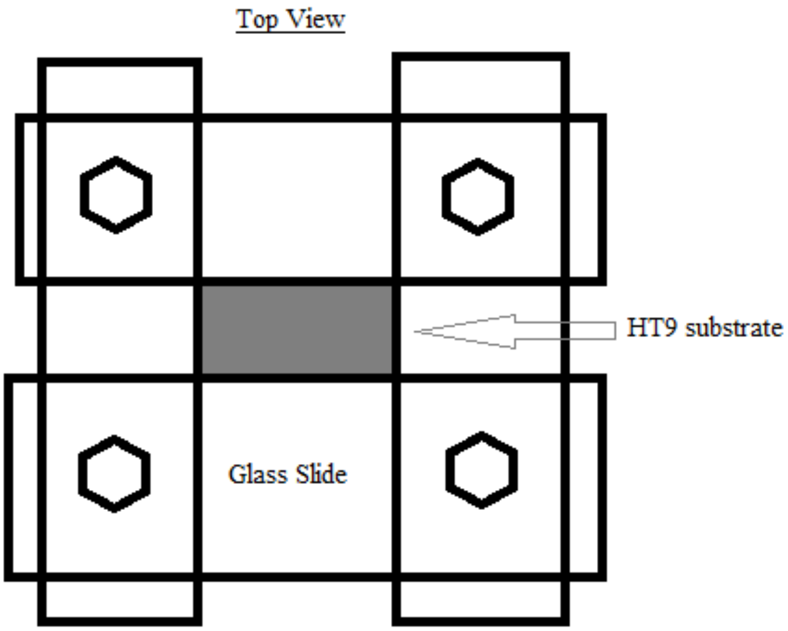

Figure 4-3. Top view of the experimental setup for the calibration of the pyrometer.

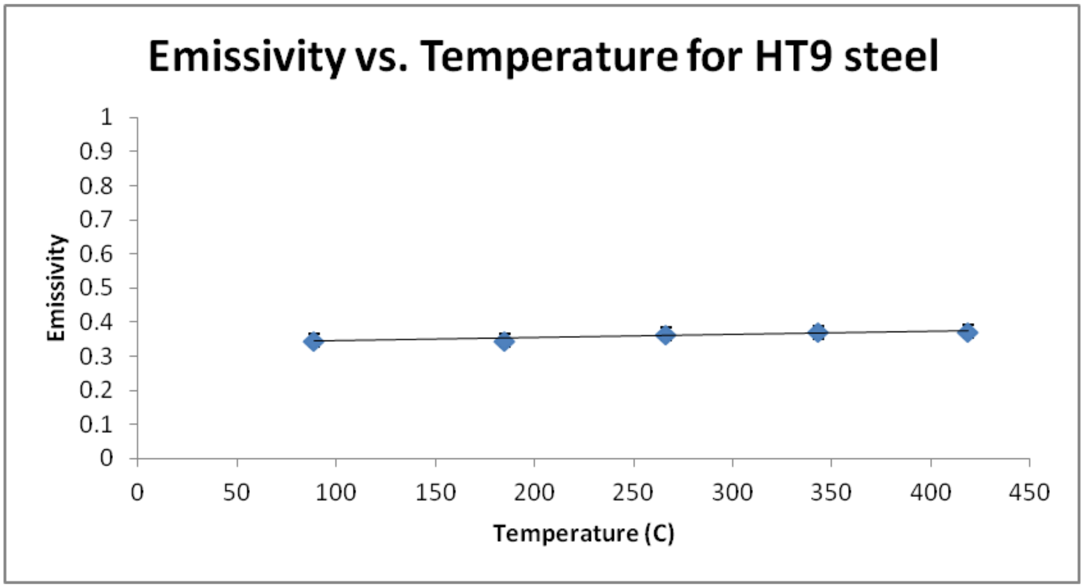

Figure 4-4. Emissivity as a function of temperature for T91 steel after polishing.

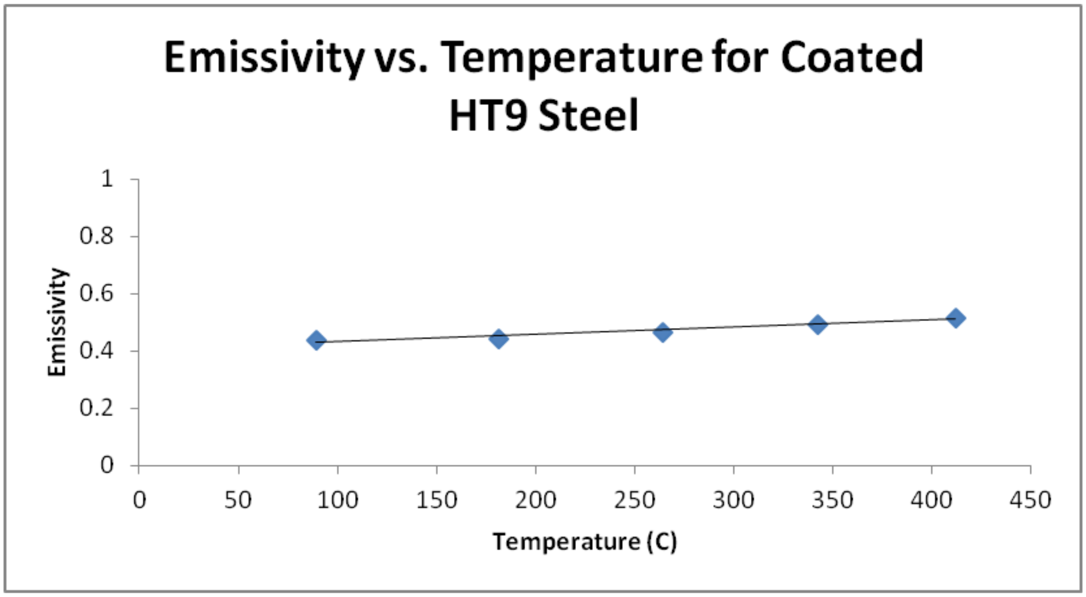

Figure 4-5. Emissivity as a function of temperature for T91 steel after being coated with vanadium carbide.

Due to the limit of the hot plate temperature range, the measured data only covers the temperature in the range of 89 to 420 ºC. The emissivity data from the as-polished and coated substrates were linearly fitted into Eq. (4-1) and Eq. (4-2), respectively. For the temperature about 420ºC, such as 650ºC used in our experiments, the value of emissivity was extrapolated from those two equations.

$$\varepsilon = 1 * 10^{-4} * T + 0.3344 \qquad (4\text{-}1)$$

$$\varepsilon = 2 * 10^{-4} * T + 0.4089 \qquad (4\text{-}2)$$

However, it was found that there was a change of emissivity along with coating time, which indicates a temperature variation of the substrate. Figure 4-6 shows the change in substrate temperature vs. coating time when the temperature was originally set to 550 ^{o}C. It is thought that this measurement causes a larger error in temperature controlling since the value of the emissivity was not adjusted continuously as the temperature increased. In addition, inaccurate measurement of the temperature may happen when the specimen was not exactly perpendicularly aligned towards the IR sensor due to the gas flow interference or any external forces.

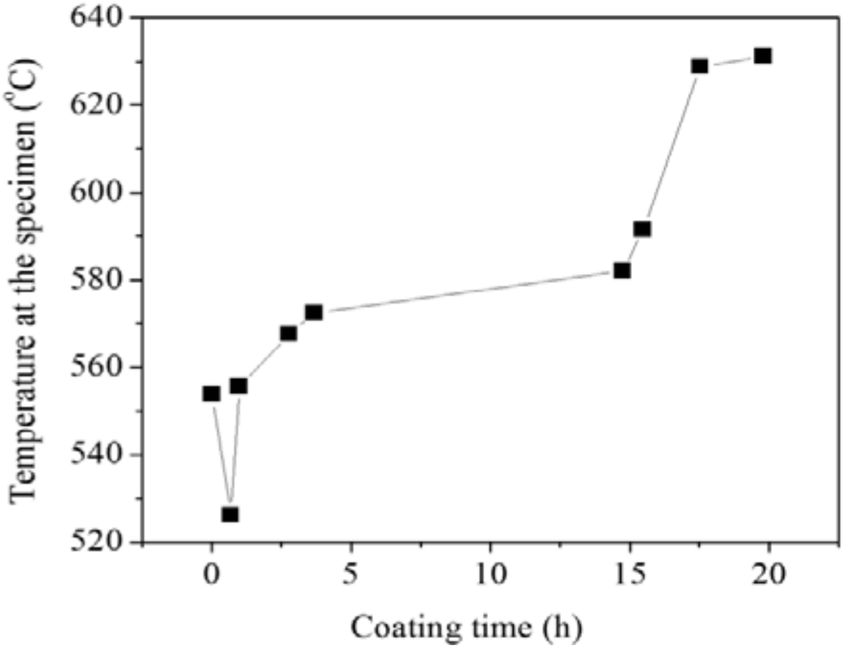

Figure 4-6. Specimen temperature readout changes with coating time.

Therefore, in this project, a direct measurement of the temperature would be suitable for the accurate temperature measurement. In addition, the graphite susceptor, which has relatively high thermal conductivity, was attached with thermo couple, and the sample was placed on the graphite (Figure 4-7a). The cutting angle of the graphite, which is the same with the sample orientation, is approximately 30°, which shows the best performance compared to other literature [14, 17]. Then, the specimen as well as susceptor were heating up by using an RF induction heater. By adopting the graphite susceptor, we expected to get an accurate temperature reading by maintaining same orientation and position of the sample during the experiment. However, due to a big difference in thermal conductivity between the graphite (25 ~ 470 W/m·K) and the T91 steel (33 W/m·K [18]), the temperatures of the specimen and the graphite boat were quite different during a heat-up process. As a result, the specimen became a red-hot, which indicates the temperature of the specimen was too high and not accurate (Figure 4-7b).

Finally, a direct measurement of substrate temperature using an embedded thermo couple (Lesker, KF16) was adopted (Figure 4-8). The thermo couple wire was inserted from an additional arm of the reaction chamber. Then, the thermo couple junction was welded, and directly contacted with the bottom of the specimen. The temperature value measured using a k-type thermo couple was inputted to the RF induction heater temperature controller. The temperature controller would take a difference between actual temperature and desired temperature and multiply it by some gain depending on the PID values and that signal is feed into the induction power supply. The power supply is able to bring the sample up to desired temperature and hold it for a significant number of hours. Therefore, it is thought that this new temperature measurement set up can help to obtain a much more stable substrate temperature during the process.

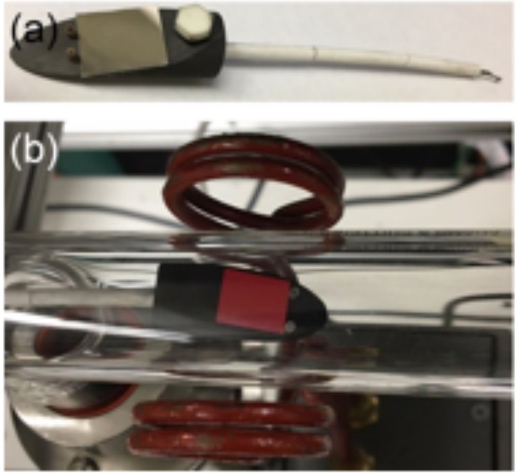

Figure 4-7. (a) The actual graphite susceptor with a thermo couple connection. (b) Chamber-loaded specimen with a graphite susceptor.

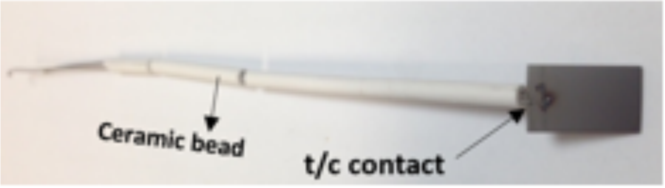

Figure 4-8. Flat coupon specimen used in the present study. A thermo couple sheathed with ceramic beads was welded at the bottom of the specimen.

4.3. Tubular Reaction Chamber

The development of coating process consists of two stages: first one for flat coupon samples and the second is the process for the actual EBR-II HT9 cladding tube. The two stages are complimentary to each other. By using the flat coupon sample, the kinetics (temperature, time) of the coating experiment can be studied. After obtaining the optimized experimental conditions with the flat coupon, it will be applied to the high aspect ratio geometry of a long and thin cladding tube (>2’ length and 0.18” ID) to evaluate the validity for the actual cladding tube. In order to apply a coating on the sample with different geometry, we need to design a reaction chamber differently for each specimen. Figure 4-9 shows a new chamber for the flat coupon specimen, which can incorporate a thermocouple feedthrough from the end of the chamber in horizontal direction that provides the easiness for the loading the specimen. With our new chamber, getting a better-quality laminar flow of the carrier gas is expected. In addition, another reaction chamber for the tubular specimen was also designed (Figure 4-10). The tubular T91 sample attached with welded thermos couple was inserted from the additional arm through the NW16 flange. Then, the sample can be inserted to the right tapered tip, and then covers over the left tip (The carrier gas flow direction is from left to right). The 2” long samples were heated up to programed temperature which was maintained as constant during the deposition.

Figure 4-9. New reaction chamber for the flat coupon sample.

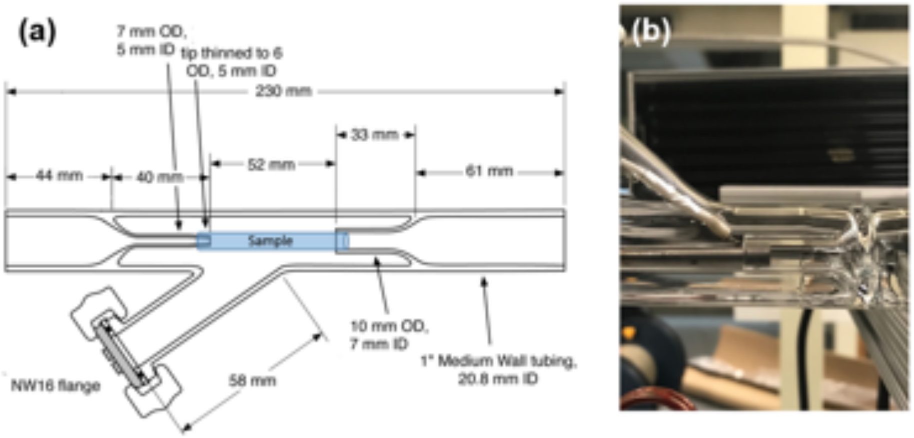

Figure 4-10. (a) Reaction chamber sketch for the tubular specimen with a diameter of 0.25” and the length of 2”. (b) Actual reaction chamber with loaded tubular sample.

4.4. Other System Built-Up

In this research, solid state vanadocene was used as a precursor, which is known to be decomposed V_xC_y [19]. It was reported that the vaporization temperature, carrier gas pressure, and flow rate are critical factors for the deposition process [17, 19]. This vanadocene organometallic precursor is known to be extremely moisture and oxygen-sensitive, and there might be potential leaks at each fitting since not all fittings provide perfect sealing of the system.

Therefore, in this study, the system was developed by welding most parts (Figure 4-10a and b) and using VCR fittings and O-ring sealing to provide a leak-tight positive pressure gas environment. As a result, it is applicable to reach at higher vacuum with leak-tight sealing, implying that crude precursors are ensured to be evaporated and to be delivered into the chamber. During the experiment, to achieve a suitable precursor vapor residence time in the chamber [17, 19, 20], it is found that the adequate gas flow and pump rates need to be balanced. When the pump rate was too high, a crude precursor powder was directly injected into the chamber by the carrier gas. In order to resolve this issue, the pump rate controlling valve was added at the end of the system. It is expected that the increase of residence time in the chamber would result in a higher chance for the vaporized precursor to deposit onto the specimen. Lastly, a water bath was added to achieve a very controlled evaporation temperature of the solid crude precursor. The actual CVD system set up is shown in Fig 4-10 (d) and (e). In addition, it was confirmed that the carrier gas with high purity should be considered in this CVD experiment, since this CVD set up and the vanadocene precursor are extremely oxygen- and moisture-sensitive [17, 19]. Typical, gas cylinder always contains a small amount of moisture. To remove the moisture in the carrier gas at its maximum level, we also added a high-performance gas purifier (Figure 4-11). Overall, a leak-tight OMCVD system with a stable supply of the precursor into the chamber was developed successfully. It is applicable for depositing a vanadium carbide coating onto the surface of the steel cladding substrate.

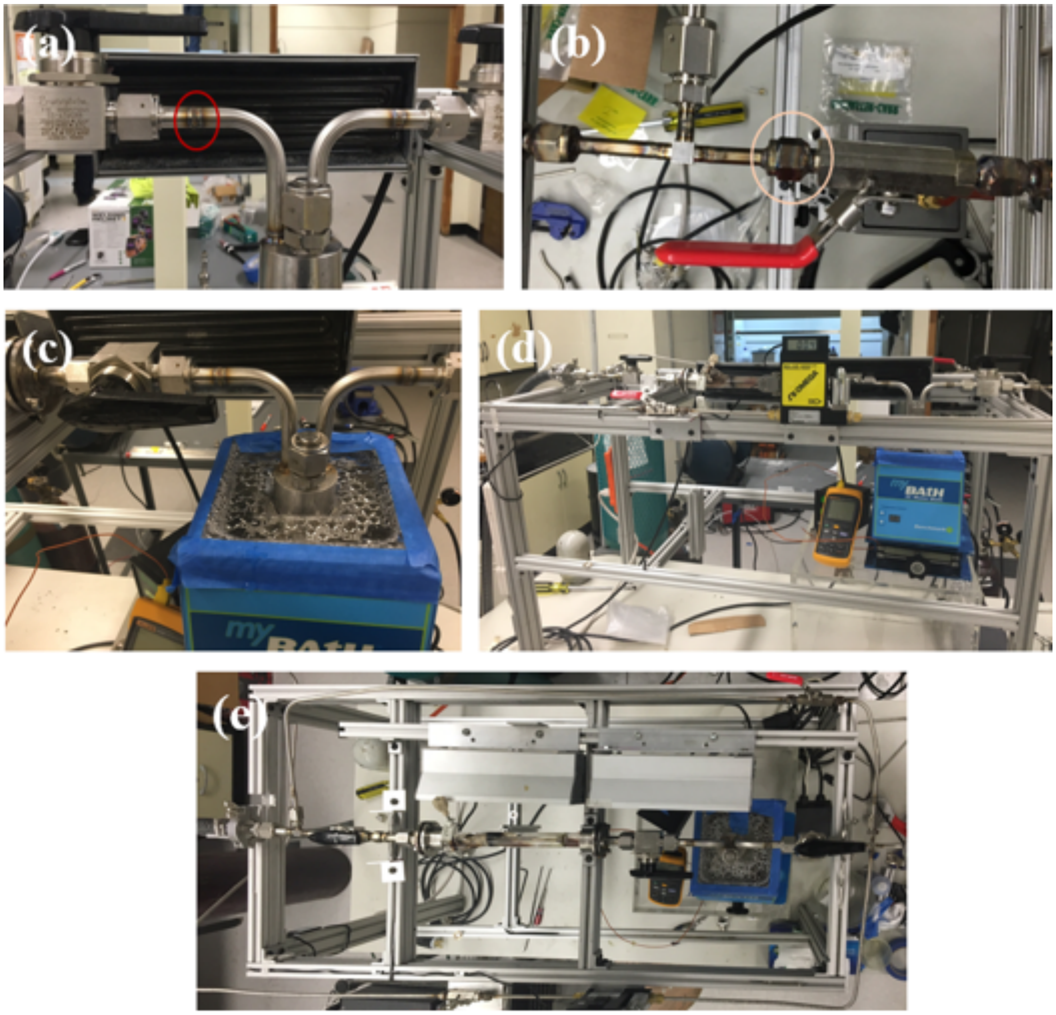

Figure 4-10. (a) Butt-welded assemblies in order to minimize the leakage. (b) Yor-lok welded assemblies at pump rate controlling valve. (c) Water bath set up to evaporate the crude precursor powder. (d and e) The actual CVD system that has been set up.

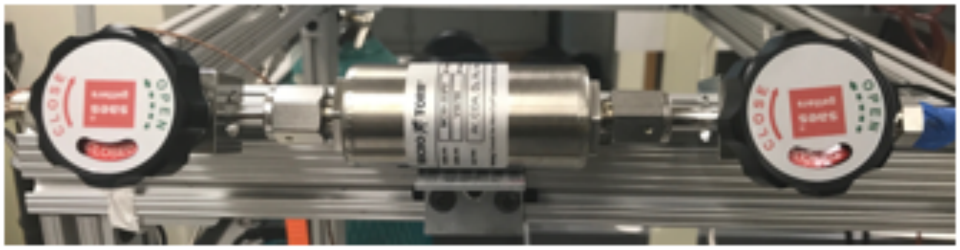

Figure 4-11. The gas purifier used for inert argon gas.

5. Materials Selection and General Deposition Procedures

Commercial T91, with the chemical compositions are Fe-8.63Cr-0.97Mo-0.1C-0.37Si-0.45Mn-0.31Ni and the actual EBR-II HT9 cladding tubes were used in our study. Prior to the coating experiment, the sample surface was polished and finished with an aqueous solution containing the colloidal silica particles. After obtaining the optimum experimental conditions with the flat coupon, it was applied onto the high aspect ratio geometry of a long and thin cladding tube (>2' length and 0.18" ID) to evaluate the feasibility for coating the actual cladding tube. Dicyclopentadienyl vanadium (vanadocene or Cp_2V, $Cp=C_5H_5$) was reported to decompose into V_4C_3 at temperatures as low as 400 ^oC [17]. In addition, the pre-existing C in the vanadium carbide layer limited the diffusion of C from a martensitic substrate into the coating layer, which resulted in inhibiting decarburization of the cladding [11]. Therefore, it is thought that Cp_2V will be an ideal precursor for this development and OMCVD using vanadium carbide precursor can be applied for a low temperature CVD process.

To start the coating process, the system was vacuumed down and then baked at 90 ^oC for 4 h in a gas mixture of 5% hydrogen balanced with argon. During the coating process, a flow rate between 10 and 200 sccm (standard cubic centimeter per minute) of carrier gas was used, and the steel substrates were heated to different temperatures between 300 and 500^oC using a RF induction heater. The deposition times varied between 4 and 10 hrs. The precursor evaporation temperature was maintained at 90^oC. The chamber pressure varied between 1 and 6 Torr controlled by carrier gas flow rate and pumping rate. Mass-flow controller (MFC) was used to control the flow rate of the carrier gas in standard cubic centimeter per minute (sccm) unit.

6. Diffusion Couple Study Procedures

The diffusion couple fixture as shown in Figure 6-1 is the key component for this experiment. The material of the fixture is Kovar alloy, which exhibits a similar thermal expansion coefficient with those of T91 and HT9, and cerium metal. The fixture was custom made by Shular Tool (Oak Ridge, TN 37830) using EDM (electrical discharge machining).

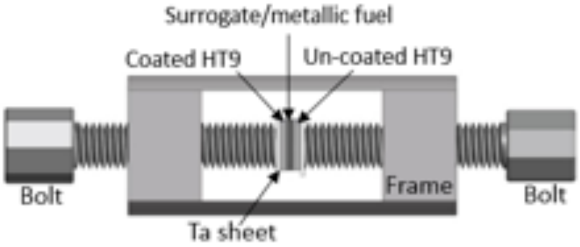

Figure 6-1. Diffusion couple fixture and the sample configuration.

Before the diffusion couple experiments, the as-received fixture was annealed in 800 °C for 8 hrs to relax the stress from machining. After the initial heat treatment, the thread on bolt and body should be re-threaded with a tap and die. The load and torque was measured by using load cell and torque wrench, respectively. Figure 6-2 shows the calibration setup and the linear torque-load relation.

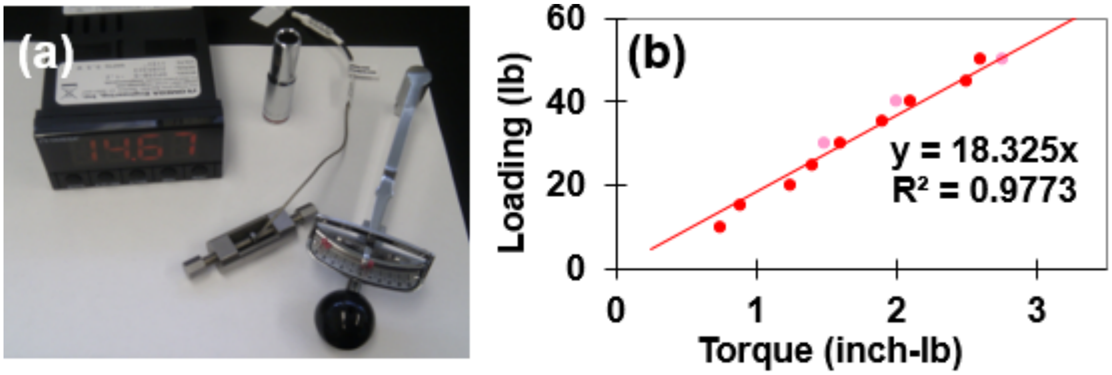

Figure 6-2. (a) Setup of calibration for the load and torque. (b) The torque-loading correlation.

Pure cerium sheet as a surrogate material was used for the diffusion couple experiments. Cerium is one of the major lanthanide fission products that diffuses from the fuel into the cladding when a steady state FCCI phenomena took place. The cerium sheet (0.8 mm in thickness) was procured from ESPI Metals (Ashland, OR 97520) with a material purity of 3N.

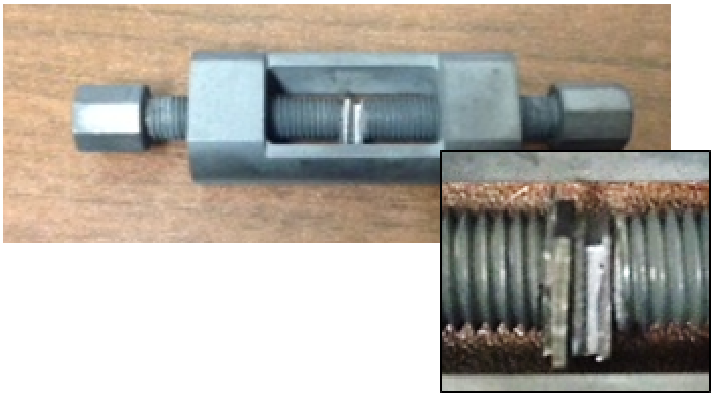

Figure 6-3. Diffusion couple fixture with sandwich-packed samples.

The coated/un-coated flat T91 coupons were mechanically clamped to the surrogate and fuel material (Figure 6-3). Tantalum foils was also placed between each side between T91 coupon and the jig to minimize inter-diffusion between the specimen and fixture. The normal stress of 7 in-lbs between the two bolts was applied using a torque wrench, which correspond to the typical contact pressure of 15 MPa between the metallic fuel and cladding in a SFR. The annealing tests were performed at various temperatures (550-690^{o}C) for 50 to 100 hrs. The low and high end of this temperature range is considered to be the normal operating temperature and the absolute maximum temperature at which the fuel/cladding interface could be exposed in even the most aggressive operating conditions, respectively [5, 21, 22]. After high temperature annealing, the diffusion couples were furnace cooled to room temperature. These fission products (e.g. cerium) are elevated in concentration at the fuel/cladding interface and play a big role in fuel cladding interaction.

7. Characterization Method

Following the coating experiments, the grain structure, chemical composition and phases of coatings were characterized using a scanning electron microscope (SEM) JEOL6400 equipped with energy-dispersive X-ray spectroscope (EDS) and X-ray diffractometer (Panalytical Xpert MRD). The cross-sectional analyses were performed to examine the morphologies and the thickness of the coating and the layer between the coating and the substrate. Depending on the thickness of region to be analyzed, several techniques can be used. The focused ion beam (FIB) is a technique which simultaneously employs the electron (i.e. SEM) and gallium ion beam on the sample surface. In the case of relatively thin film deposition (<10 μm), the FIB was used to assist the cross-section analysis procedure. By milling out a trench on the coated sample surface at 45^o, the thickness and grain structure of the coating can be directly observed suing SEM. The compositional profile was obtained by using EDS line-scan.

The microstructures of the diffusion couple specimens were examined using electron microscopy to evaluate their functionality as diffusion barrier by determining the new phases formed along the interaction interface, any fast diffusion paths from texture of the coating layer and determining the kinetics of the chemical inter-diffusion. The elemental composition of the interaction layers was also quantified using energy dispersive X-ray spectroscopy (EDS) and wavelength dispersion spectroscopy (WDS). Additionally, cross-sectional transmission electron microscopy (TEM) were selectively performed.

8. Results and Discussion

8.1 Low temperature CVD experiments

8.1.1. Coating Surface Morphology and Cross Section Characterization

The substrate temperature is by far the most important factor for controlling the coating grain structure and deposition rate due to its strong influence on the decomposition reaction rate of the vapor molecules and on the surface mobility of atoms [17, 19]. Figure 8-1 shows the surface morphology of the coating obtained with the Cp_2V precursor at a wide range of temperatures between 300 and 500 ^{o}C with the carrier gas flow rate of 50 sccm. The grain size was determined based on the ASTM standard for average grain size. At 300 ^{o}C (Figure 8-1a), the average grain size is approximately 200 nm and the substrate was not fully covered by the coating layer. The EDS spectrum also shows that Fe, Si, and Cr elements as well as V and C were observed, indicating elements other than V and C were detected from the T91 substrate surface. In contrast, well-developed coatings with an average grain size of approximately 500 nm and 2.5 μm were obtained at 400and 500 ^{o}C, respectively (Figure 8-1b and c). The EDS spectra in Figure 8-1b and c show that the coating contains both V and C, while no peaks for Fe, Si, and Cr were detected from the T91 steel. Therefore, it is thought that vanadium carbide coatings were effectively deposited onto the substrate at 400 and 500^{o}C. The SEM surface morphology taken at a lower mag (Figure 8-2, ×500 magnification) further shows that vanadium carbide coating was well developed at a large surface area of the specimen. One notable finding is that C content increased with increasing temperature, and the coatings are likely V_2C and VC at 400^{o}C and 500^{o}C, respectively. This is probably due to the fact that higher temperature promotes C diffusion [19].

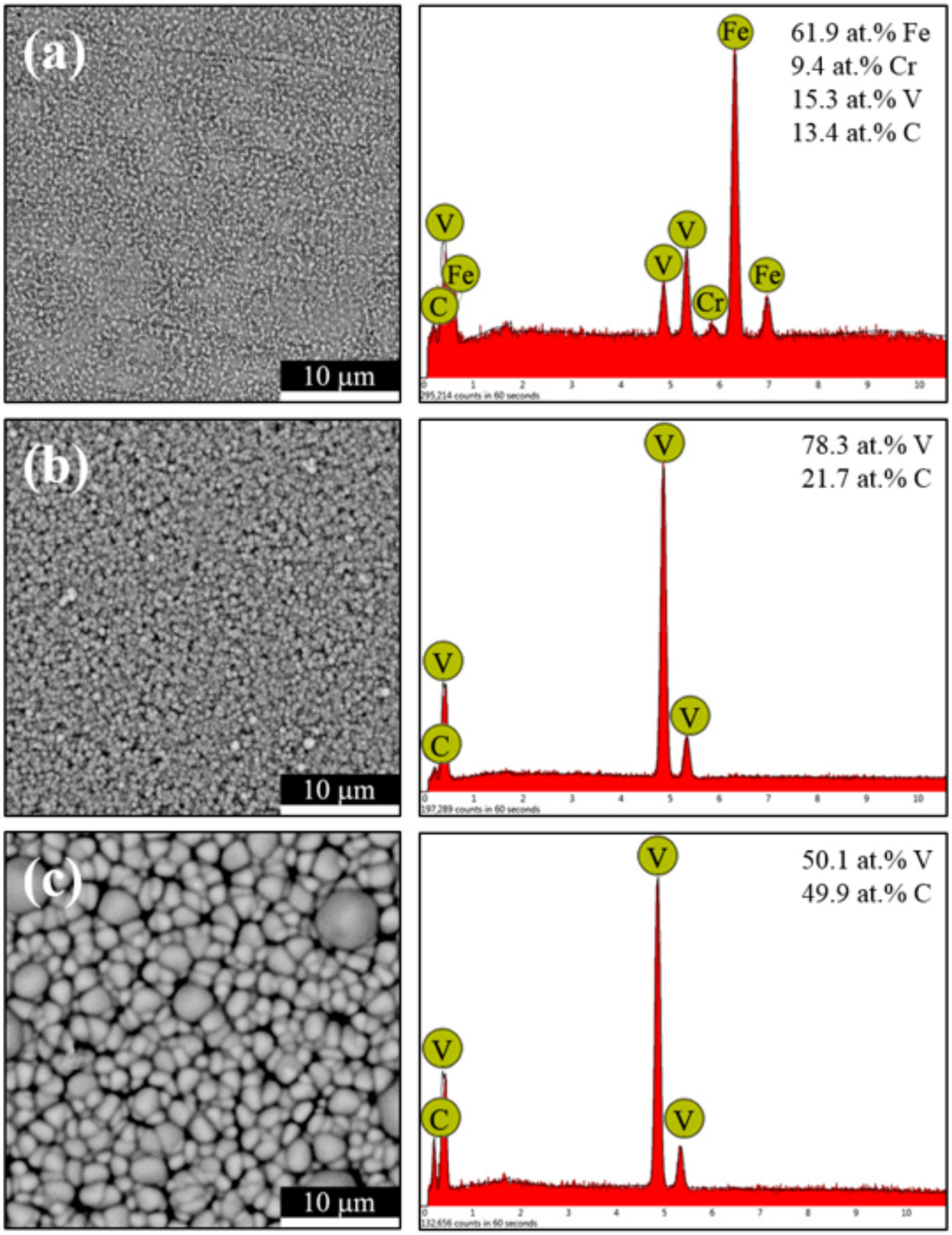

Figure 8-1. SEM surface morphology (left) and EDS spectra (right) of the specimens coated at (a) 300 °C, (b) 400 °C, and (c) 500 °C with the flow rate of 50 sccm.

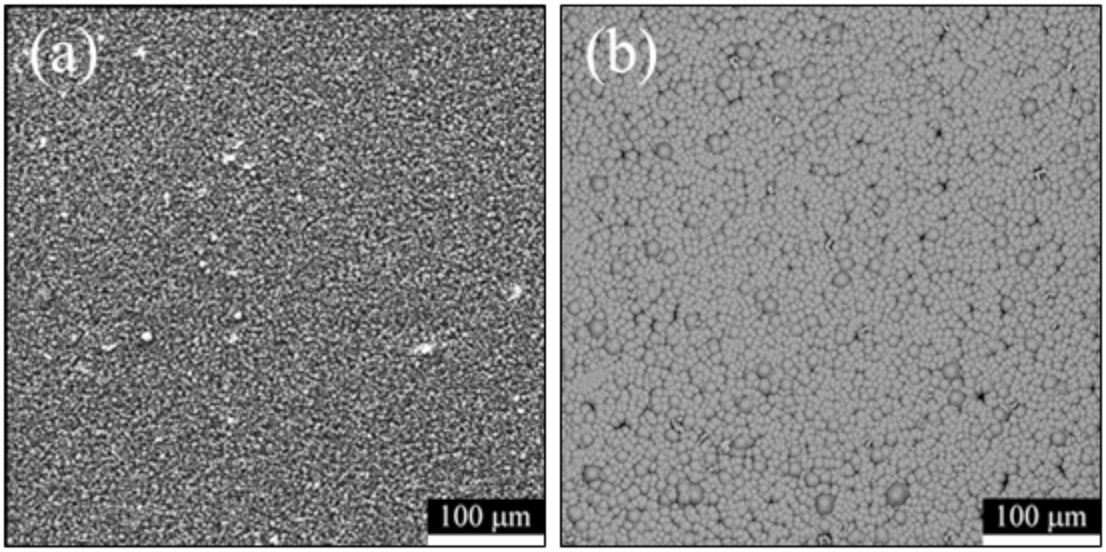

Figure 8-2. SEM surface morphology coated at (a) 400 °C and (b) 500 °C with the flow rate of 30 sccm taken at low magnification (× 500)

The cross-section SEM image in Figure 8-3 shows that there is no gap or de-adhesion between the coating and T91 substrate, and the coating thickness is approximately 1.5 μm and 5.5 μm for the 400 °C and 500 °C specimens, respectively. It is speculated that the increase in thickness is attributed to more adsorption and surface reactions taking place at a higher substrate temperature.

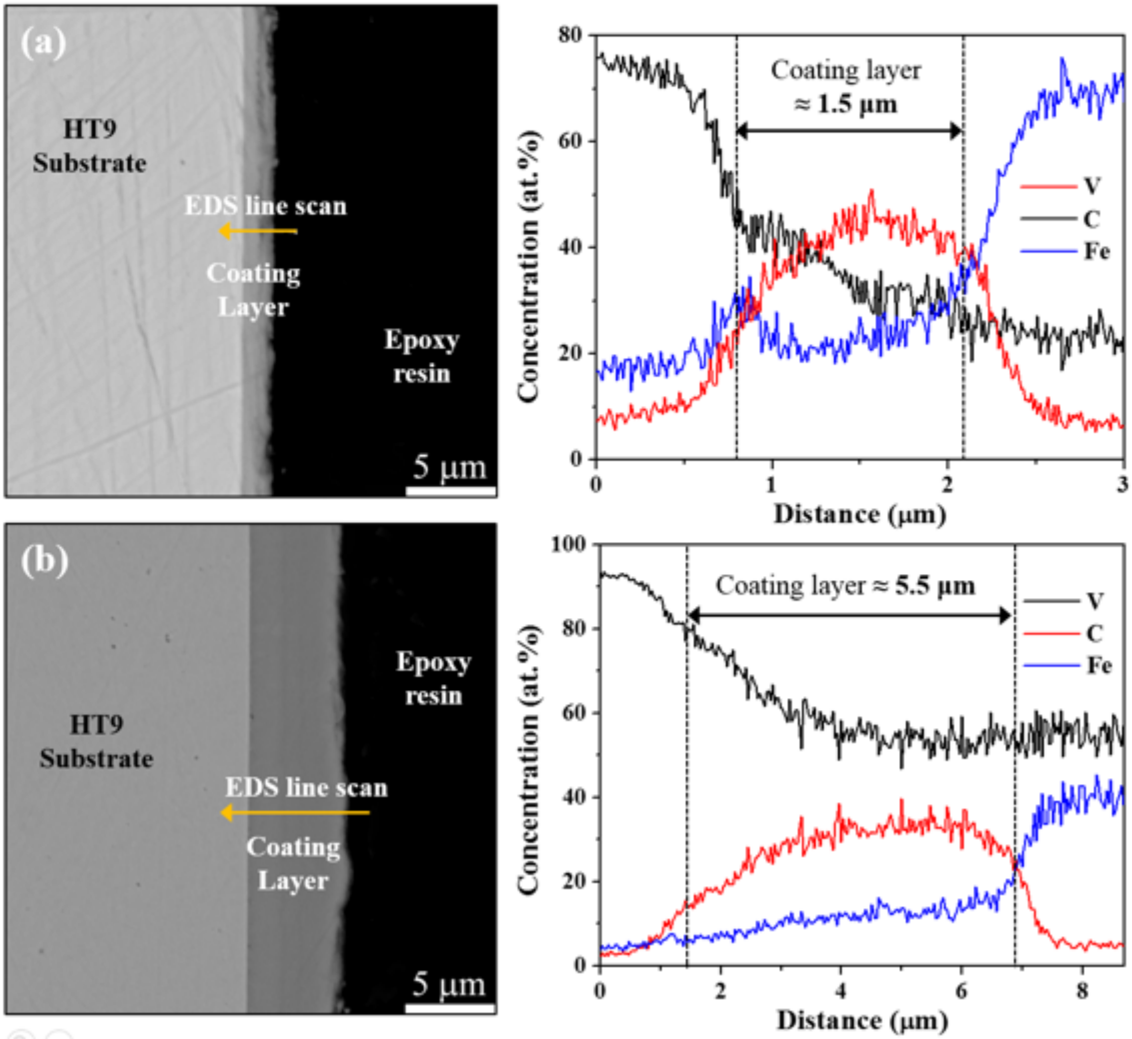

Figure 8-3. SEM cross sectional images (left) and concentration depth profiles (right) deposited at (a) 400 °C and (b) 500 °C.

For the deposition of a thick coating, low flow rate of the carrier gas (10 sccm) and longer deposition time (20 hrs) were used at both 400 °C and 500 °C. Figure 8-4 shows the surface morphology of the coating obtained with the Cp_2V as a precursor at two different temperatures of 400 °C and 500 °C. A well-developed coating with an average grain size of approximately 2.5 μm and 4.8 μm were obtained at 400 °C and 500 °C, respectively (Figure 8-4a and b). The grain size was determined based on the ASTM standard for average grain size. The EDS spectra in Figure 8-4c and d show that the coating contains both V and C. Therefore, it is thought that V and C were well-developed on the substrate at 400 °C and 500 °C using newly developed CVD system. However, the suspected low concentration of oxygen was not detected by EDS.

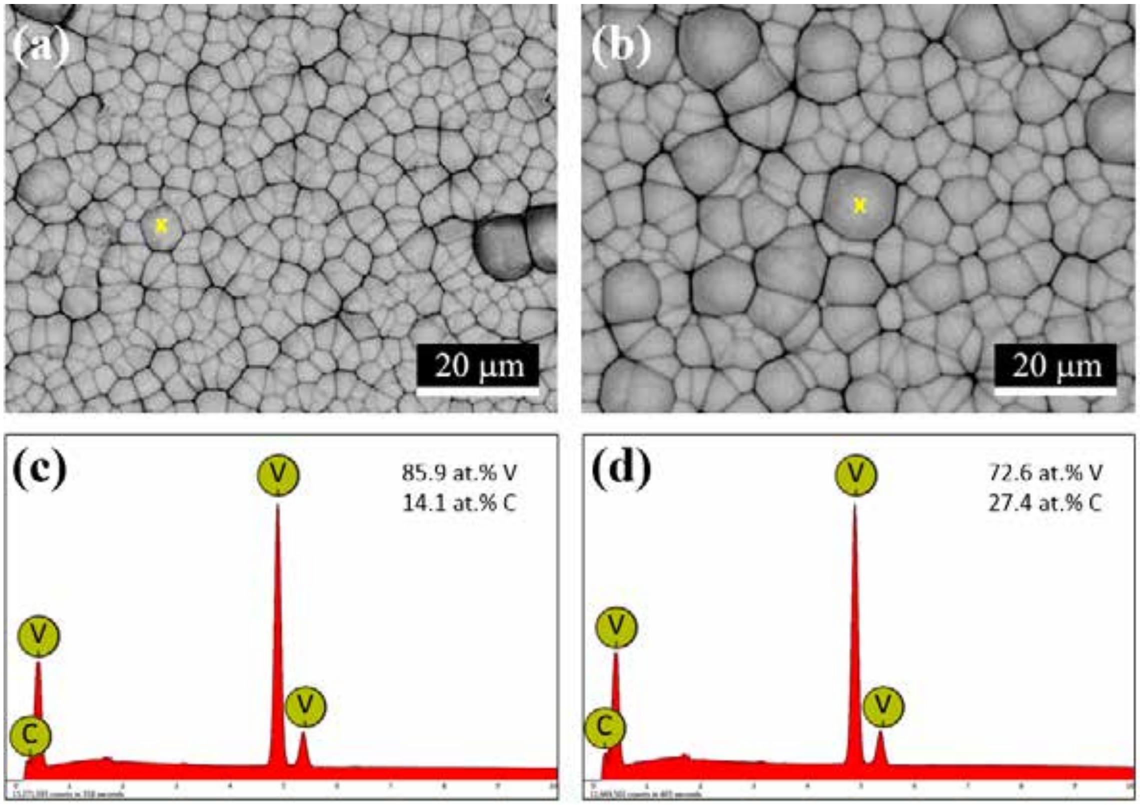

Figure 8-4. SEM surface morphology and EDS spectrum of the specimens coated at (a and c) 400 °C and (b and d) 500 °C.

The SEM cross-sectional images in Figure 8-5 show that there is no gap or de-adhesion between the coating and T91 substrate, and the coating thickness is approximately 6 µm and 8 µm for processing temperatures of 400 °C and 500 °C, respectively. EDS line profiles in Figure 8-5c and d also show that both V and C are the main species in the coating and both elements present complementarily in the coating, while a few percentage of iron was detected in the coating.

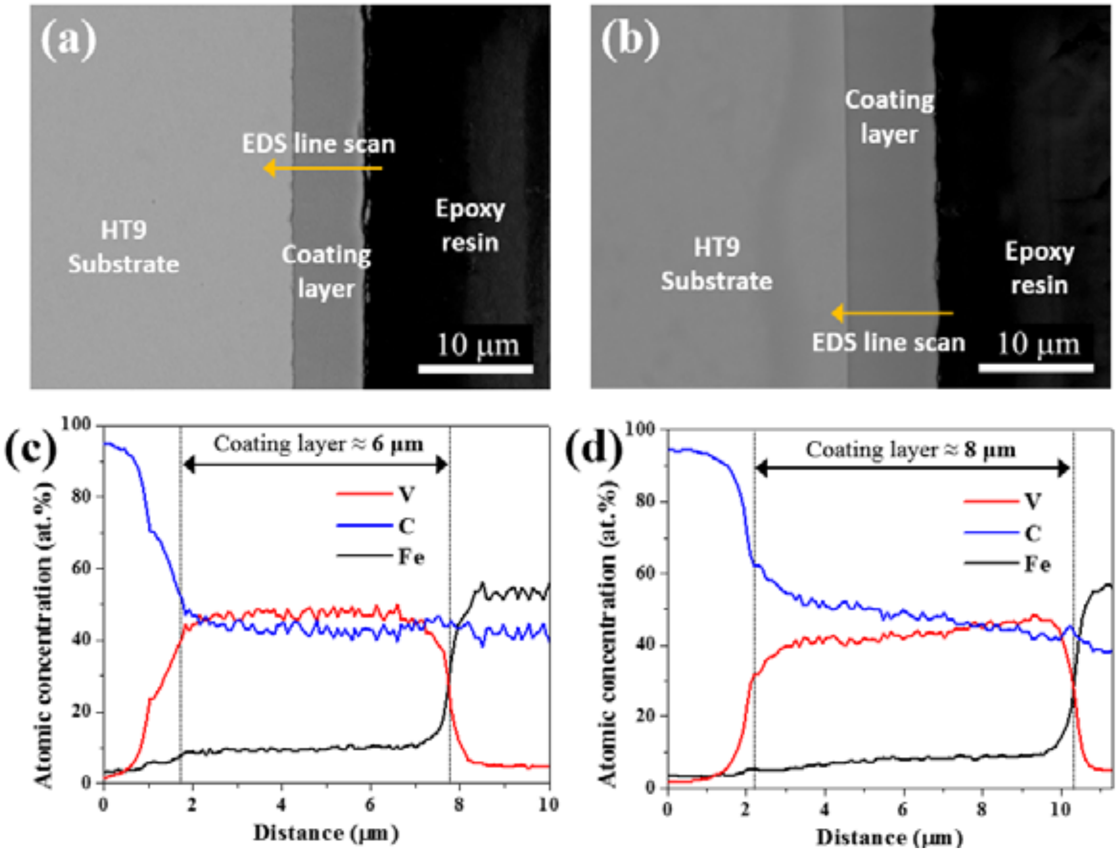

Figure 8-5. SEM cross sectional images and EDS line scan profiles of the specimens coated at (a and c) 400 °C and (b and d) 500 °C.

The coating results such as average grain size, content of V and C, and thickness of the coating are summarized in Figure 8-6 as a function of temperature. It is clearly seen that the grain growth occurred and the grain size increased dramatically at 500 °C.

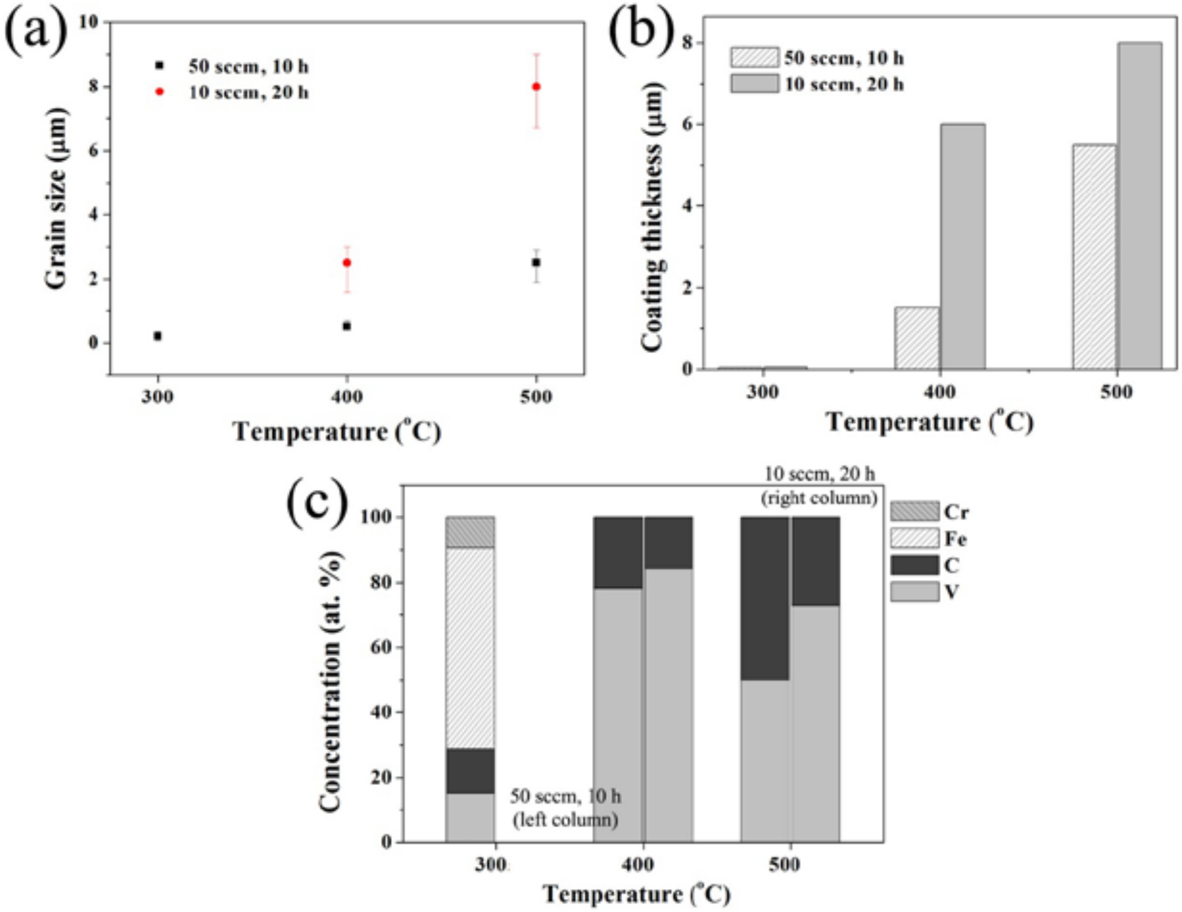

Figure 8-6. (a) Average grain, (b) thickness of the coating, and (c) content of V and C in the coatings deposited at 300, 400, and 500 °C, respectively.

Another coating experiments with relatively low carrier gas flow rate with lower evaporation rate of the precursor was also performed. Figure 8-7a shows SEM surface morphology of the specimen deposited at 500 °C with the flow rate of 10 sccm and the precursor temperature of 70 °C. It seems that all surface was fully covered with vanadium carbide. The average grain size of the coated particle was approximately 8 µm. EDS result in Fig 8-7b also confirms that the specimen was fully covered. The compositions at the spot marked with 'x' was 48 at.% V-52 at.% C. Lower magnification image in Figure 8-8 also shows that most area on the specimen was fully covered with vanadium carbide. The SEM cross sectional image in Figure 8-9 shows that the coating with approximately 8 µm was deposited on the surface of the T91 steel. There was no gap or de-adhesion between the substrate (T91) and the coating. However, the coating quality was not the best compared with previous results. The pores was observed in the middle of the coating, and the surface of the coating was not smooth.

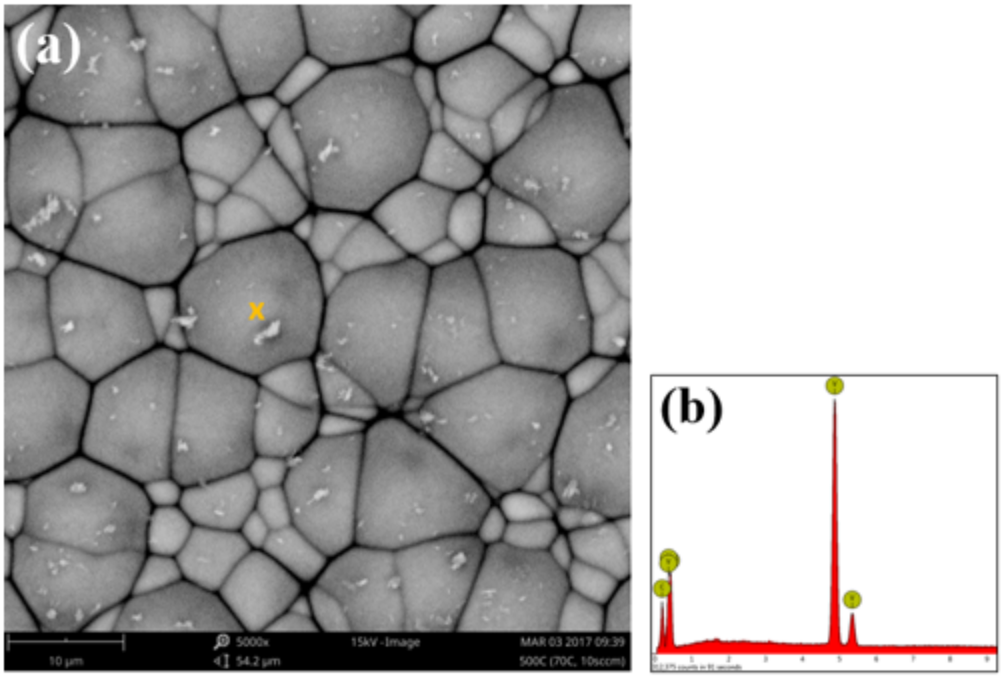

Figure 8-7. (a) SEM surface morphology of the specimen and (b) EDS spectra. The ‘x’ indicates the spot where the EDS spot analysis was performed. The sample was coated at 500 ^oC with the flow rate of 10 sccm and the precursor temperature of 70 ^oC.

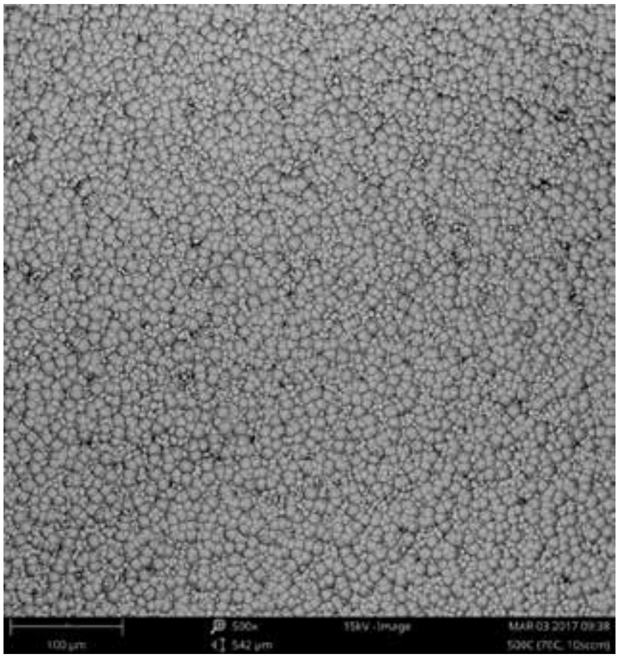

Figure 8-8. Lower maginification (×500) SEM surface morphology of the specimen deposited at 500 ^oC.

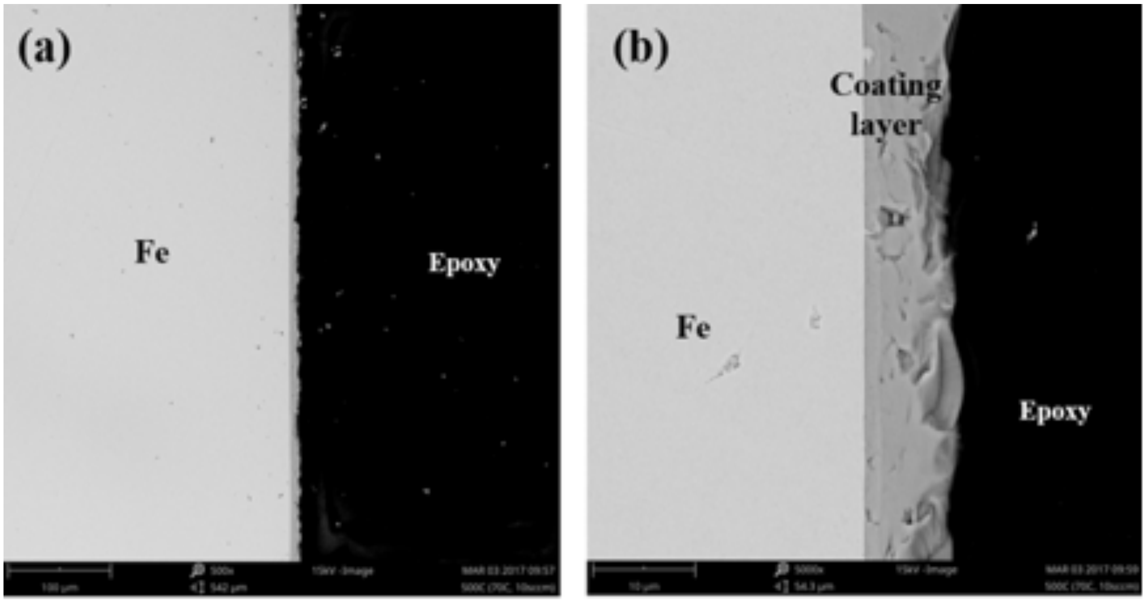

Figure 8-9. (a) Low (×500) and (b) high (×5000) magnifications SEM cross sectional images deposited at 500 ^oC with the flow rate of 10 sccm and the precursor temperature of 70 ^oC.

Higher flow rate of 20 sccm instead of 10 sccm was followed to deliver a vaporized precursor more efficiently. The gas purifier was also adopt in this experiment. The SEM surface morphology in Figure 8-10a shows well-developed coating on the specimen. The average grain size of the coated particle was approximately 10 μm and it mainly contains 56 at. % V and 44 at. % C, which shows a similar ratio with previous result. Lower magnification image in Figure 8-11 also shows that most area on the sample was fully-covered with vanadium carbide.

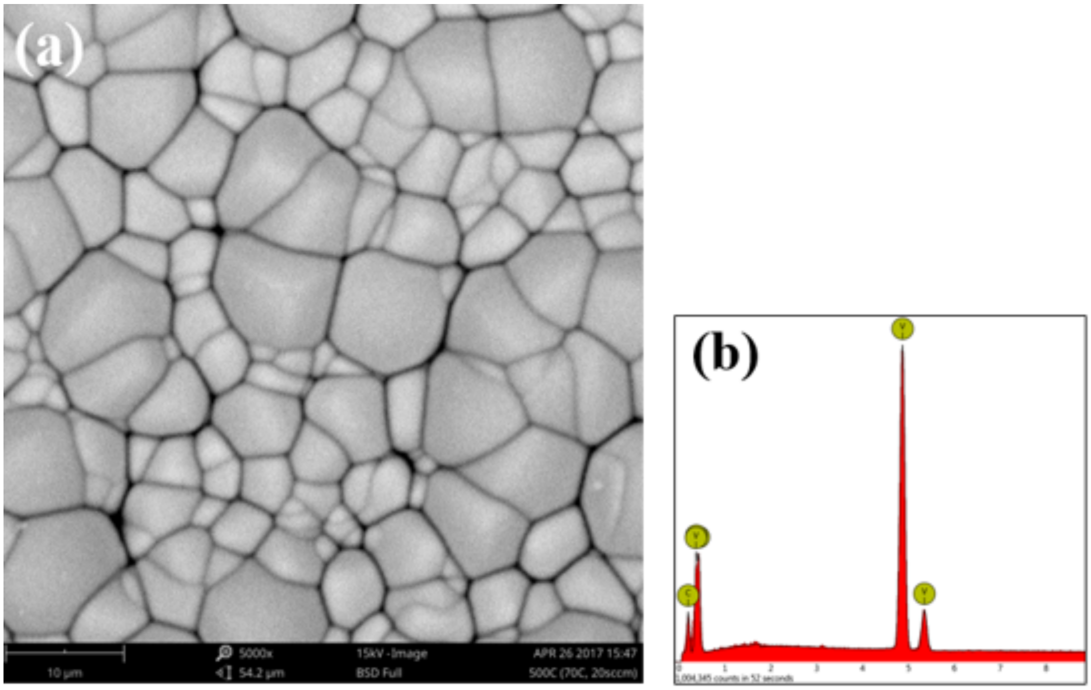

Figure 8-10. (a) SEM surface morphology and (b) EDS spectra of the sample coated at 500 ^{o}C with the flow rate of 20 sccm and the precursor temperature of 70 ^{o}C.

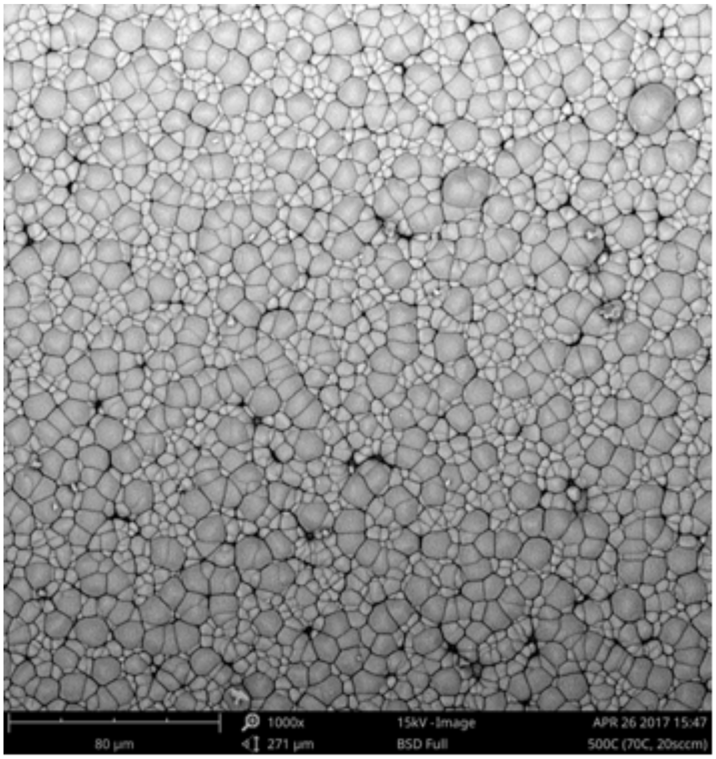

Figure 8-11. (a) Lower magnification (×1000) SEM surface morphology of the sample coated at 500 ^{o}C with the flow rate of 20 sccm and the precursor temperature of 70 ^{o}C.

However, the quality of the coating seems not good. The SEM cross sectional image in Figure 8-12 shows that the coating was well-deposited on the surface of the T91 steel, and there was no gap or de-adhesion between the substrate (T91) and the coating. The thickness of the coating was approximately 6.5 μm. Although there was no pore developed in the coating, the surface of the coating was not smooth, either. This is probably due to a fluctuated carrier gas flow with vaporized precursor, and the carrier gas flow as well as the sample position need to be optimized to obtain better quality coating sample (e.g. Figure 8-4 and 8-5).

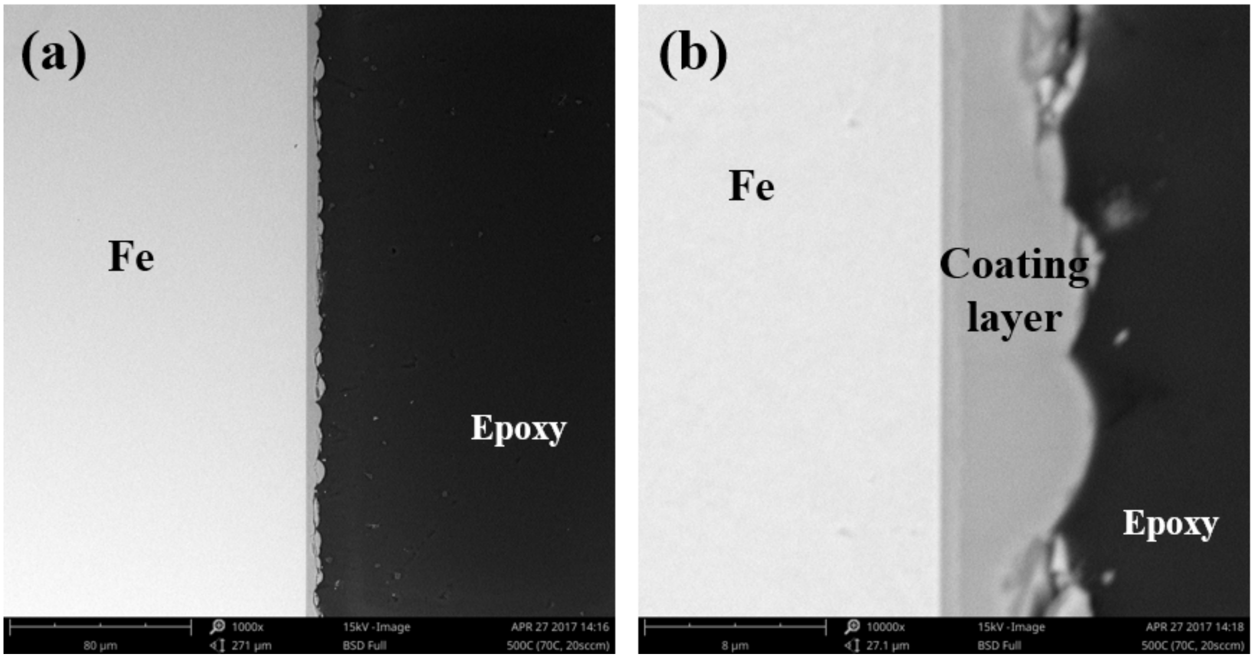

Figure 8-12. (a) Low (×1000) and (b) high (×10000) magnifications SEM cross sectional images of the specimen. The sample was deposited at 500 ^{o}C with the flow rate of 20 sccm and the precursor temperature of 70 ^{o}C.

8.1.2. Effect of Carrier Gas Diffusivity

Several carrier gases such as Ar, He, and H_2 were used in CVD experiments [19, 23, 24]. For example, He gas, which is known to have a high reduction characteristic, was adopted as a carrier gas in order to inhibit the reaction with an oxygen and moisture. Several experiments were performed with different conditions (e.g. sample position in the chamber, carrier gas flow rate between 5 and 20 sccm). However, the sample was not coated under various conditions. It is thought that vaporized precursor along with the He carrier gas was not deposited on the specimen efficiently, since a thermal diffusivity of the He is approximately 7 ~ 8 times higher than Ar, and the reactant gas diffusivity is also higher in He than that in Ar [23]. It was revealed that the stagnation of the carrier gas and the staying time around the specimen are key factor, and the He as a carrier gas, which has a faster atomic movement, was not suitable/favorable in our CVD set up. Momentum and thermal diffusivities derived from Lennard-Jones parameters were summarized in Table 8-1 [23].

Table 8-1. Momentum and thermal diffusivities of carrier gases at 0.3 mbar, 500 K [23].

	Momentum diffusivity [cm^2/s]	Thermal diffusivity [cm^2/s]
Ar	1200	1800
He	9800	13,100
H_2	8700	12,300

8.1.3. Combination beteen Evaporation and Carrier Gas Flow Rates

Figure 8-13 shows actual reaction chamber and the evaporator after the test. It seems carrier gas flow was well performed since there was no blockage or deposition at the entrance of the chamber (Figure 8-13a, marked with an arrow). The carrier gas flow rate and the heating temperature of the precursor were 15 sccm and 80 °C, respectively. However, after the test, some precursor was left around the evaporator (Figure 8-13b), indicating that the vaporized precursor was not fully delivered to the chamber. In terms of the evaporation rate of the precursor and the carrier gas flow rate, there are two possibilities that caused the blockage at the evaporator based on the literature [17]; one is high evaporation rate caused from high precursor temperature, and the other is that the carrier gas flow rate of 15 sccm was not sufficient to deliver the vaporized precursor to the chamber under these conditions. Therefore, two more experiments were carried out. The details of the test conditions were listed in Table 8-2.

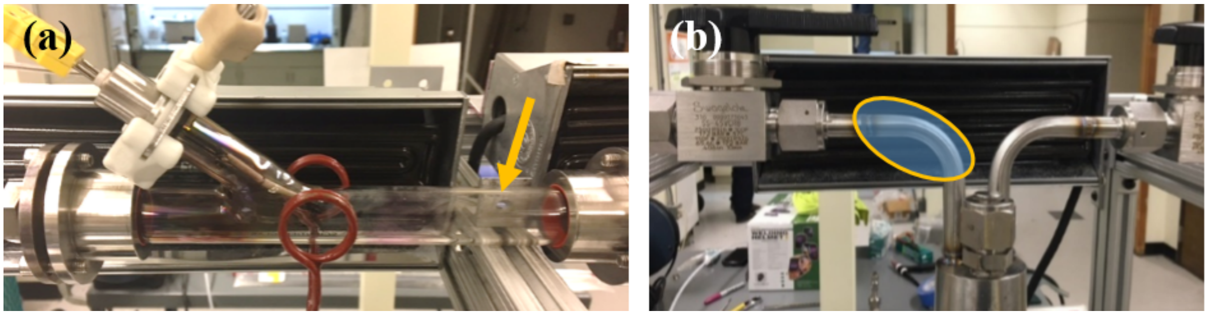

Figure 8-13. (a) Actual reaction chamber and (b) the evaporator after the test.

Table 8-2. The CVD test conditions and the anticipated results.

$T_{precursor}$ (°C)	Flow rate (sccm)	Results
80	15	Not fully delivered to the chamber.
80	30	Higher flow rate will deliver the precursor to the chamber.
75	15	Lower evaporation rate may inhibit the blockage at the evaporator.

Figure 8-14a shows SEM surface morphology of the specimen deposited at 500 °C with the flow rate of 15 sccm and the precursor temperature of 80 °C. It seems that all surface were not fully covered with vanadium carbide probably due to the limitation of the precursor supply caused from the blockage at the evaporator. EDS results in Fig 6b and c also confirm that the specimen was not fully covered. The compositions of the spot #1 and #3 are 70 at.% V-30 at.% C and 45 at.%- 23 at.% C-28 at.% Fe-4 at.%., Especially in spot #3, Fe and Cr elements as well as V and C were observed, indicating elements other than V and C were detected from the T91 initial surface. Lower magnification image in Figure 8-15 also shows that the delivery of the vaporized precursor was not sufficient to deposit all surface.

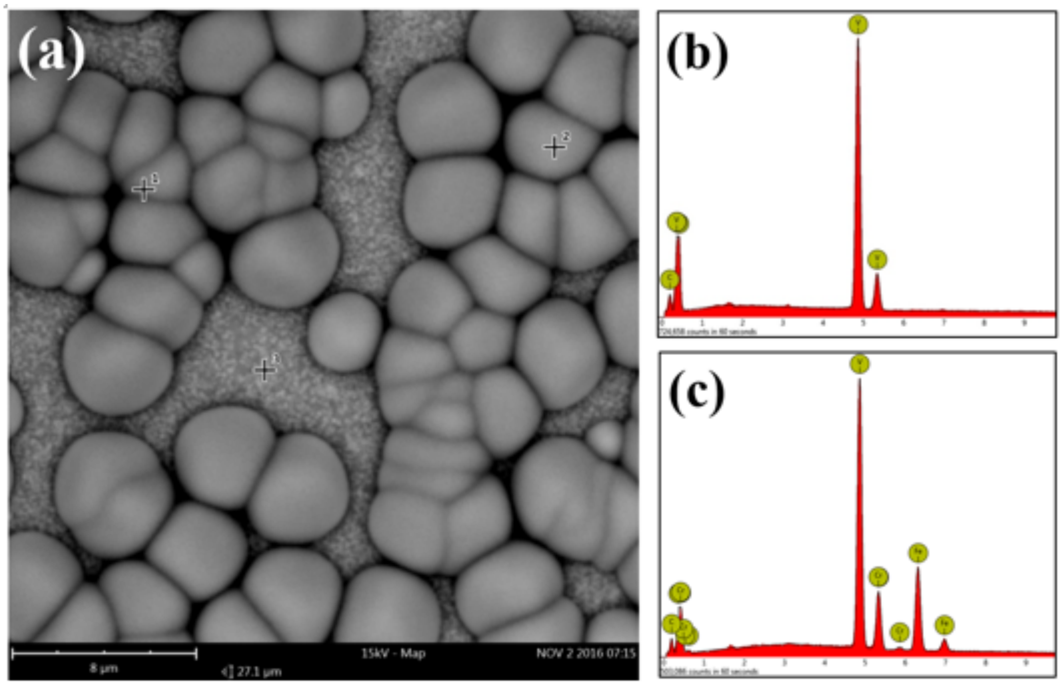

Figure 8-14. (a) SEM surface morphology of the specimen and EDS spectra of the (b) spot #1 and (c) spot #3. The sample was coated at 500 °C with the flow rate of 15 sccm and the precursor temperature of 80 °C.

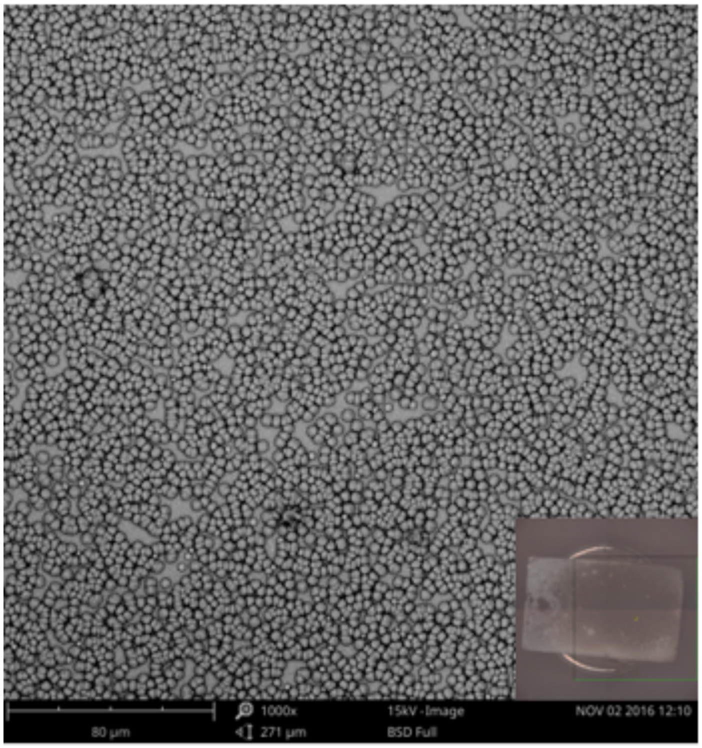

Figure 8-15. Lower maginification (×1000) SEM surface morphology of the sample coated at 500 °C with the flow rate of 15 sccm and the precursor temperature of 80 °C.

Higher flow rate of 30 sccm instead of 15 sccm was followed to deliver a vaporized precursor more efficiently. Although there was a small amount of blockage at the end of the system probably because of the high carrier gas flow rate, the sample surface was well-deposited with vanadium carbide (Figure 8-16). However, it seems there is a gradient in concentration between the center (Figure 8-16b) and the edge (Figure 8-16c) of the specimen. The average grain size of the coating was approximately 3.5 µm and mainly composed with 44 at.% V-56 at.% C (Figure 8-17). The SEM cross sectional image in Figure 8-18 further confirms that the coating was well-deposited on the surface of the T91 steel. There was no gap or de-adhesion between the substrate (T91) and the coating. The thickness of the coating was approximately 7 µm.

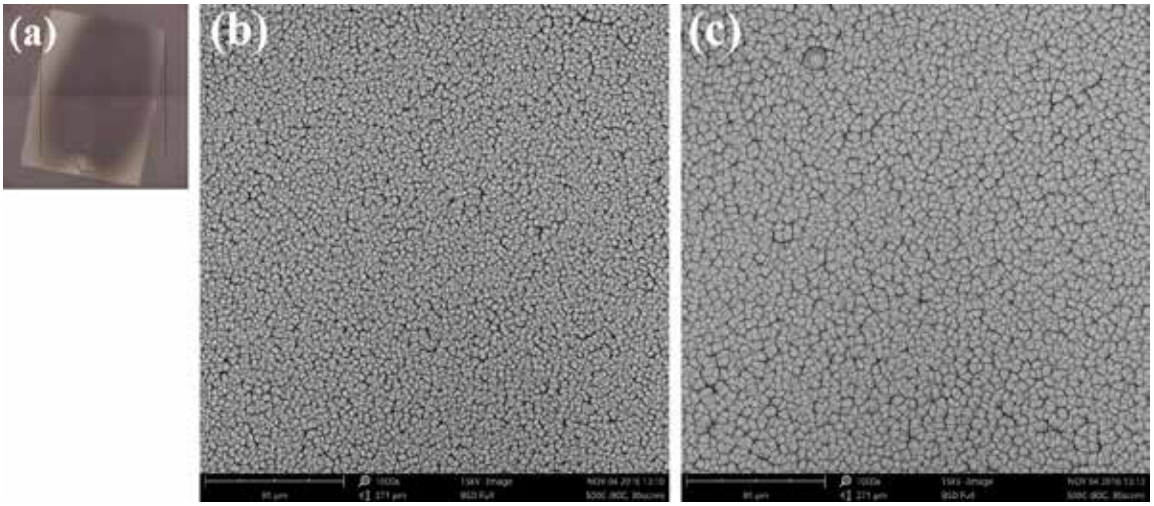

Figure 8-16. (a) Specimen after the test. There is a gradient in concentration between the center and edge of the specimen. SEM surface morphology of (b) center and (c) edge regions.

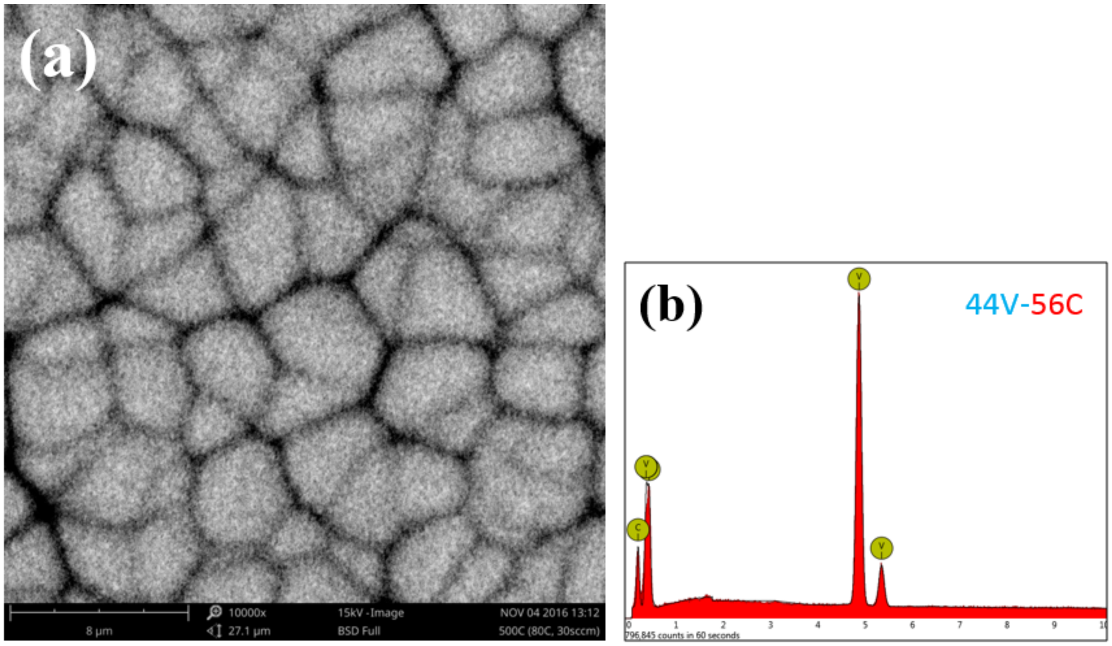

Figure 8-17. (a) Higher magnification (×10000) SEM surface morphology and (b) EDS spectrum of the sample coated at 500 ^{o}C with the flow rate of 30 sccm and the precursor temperature of 80 ^{o}C.

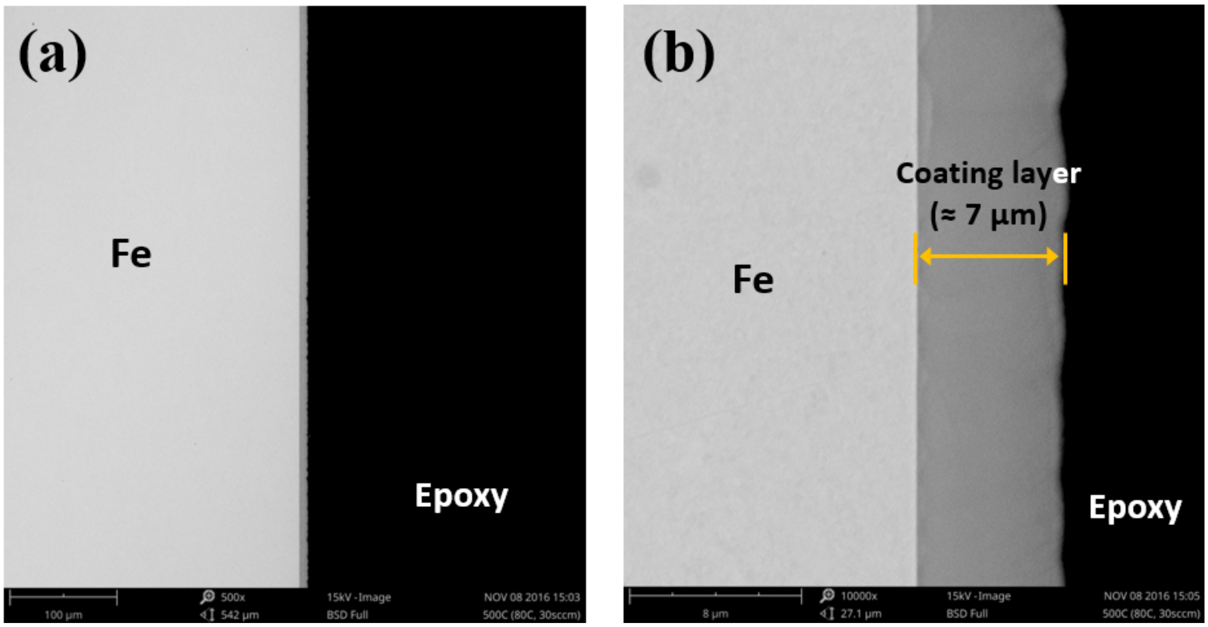

Figure 8-18. (a) Low (×500) and (b) high (×10000) magnifications SEM cross sectional images deposited at 500 °C with the flow rate of 30 sccm and the precursor temperature of 80 °C.

Based on the CVD test schedule, lower precursor temperature (75 °C) by keeping the carrier gas flow rate the same (15 sccm) was performed in order to control the evaporation rate of the precursor and inhibit the blockage around the evaporator. The experiment was performed at 500 °C substrate temperature with the flow rate of 30 sccm and the precursor temperature of 80 °C, and there was no blockage after the test. The sample, however, has quite similar morphology that there was a gradient in concentration between the center and the edge of the specimen (Figure 8-19). The SEM surface morphologies of the center (Figure 8-20a) and the edge (Figure 8-20b) were similar with each other, and all surface were covered with the coating. The coating thickness was approximately 2.5 µm in Figure 8-21a, and the composition of the coating was 57 at.% V-43 at.% C (Figure 8-21b). The SEM cross sectional image in Figure 8-22 shows that the coating was well-deposited on the surface of the T91 steel, and there was no gap or de-adhesion between the substrate (T91) and the coating. The thickness of the coating was approximately 5.5 µm.

Figure 8-19. The sample after the CVD test.

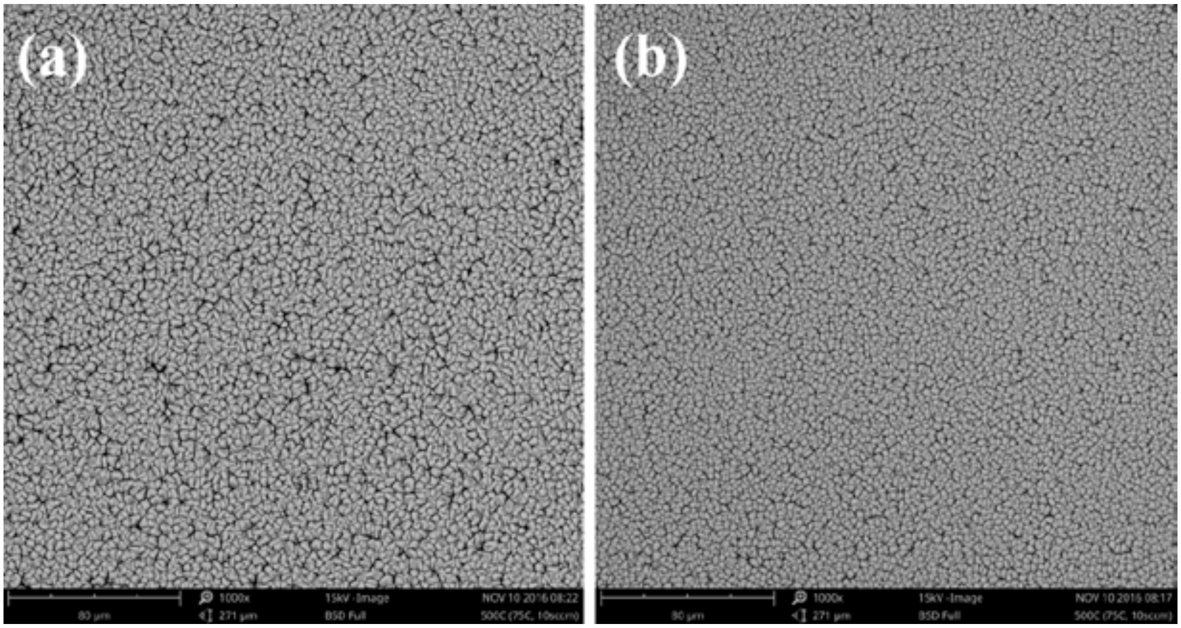

Figure 8-20. SEM surface morphology of (a) Center and (b) edge of the specimen deposited at 500 ^{o}C with the flow rate of 15 sccm and the precursor temperature of 75 ^{o}C.

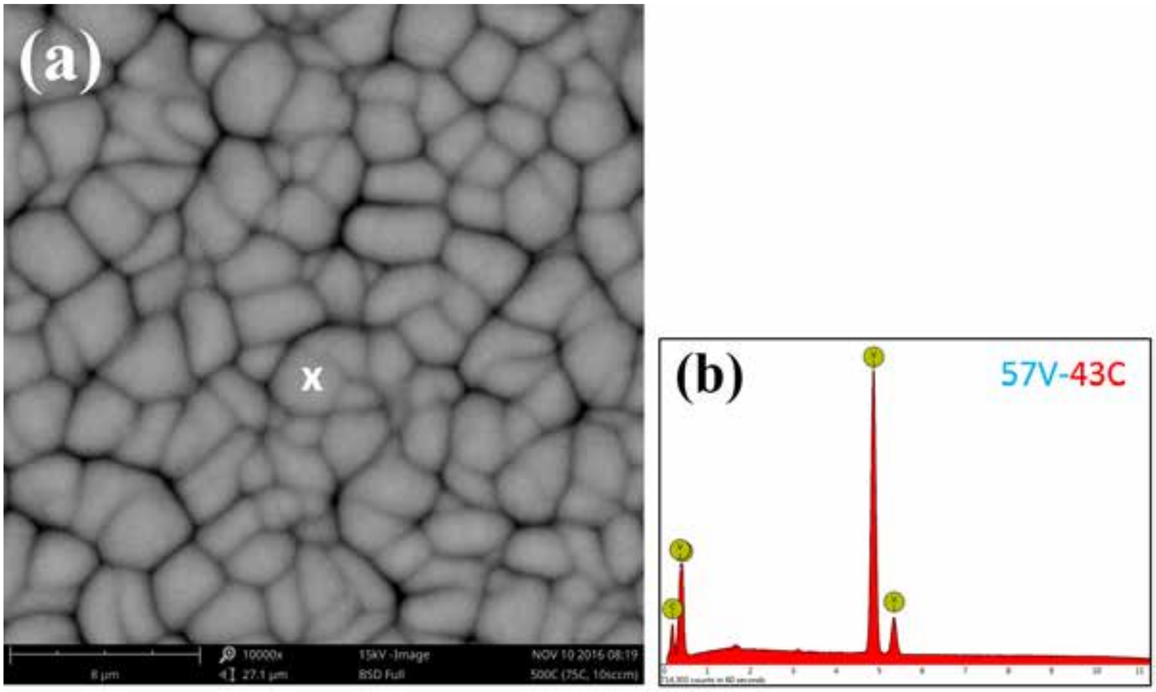

Figure 8-21. (a) Higher magnification (×10000) SEM surface morphology and (b) EDS spectrum of the sample coated at 500 ^{o}C with the flow rate of 15 sccm and the precursor temperature of 75 ^{o}C.

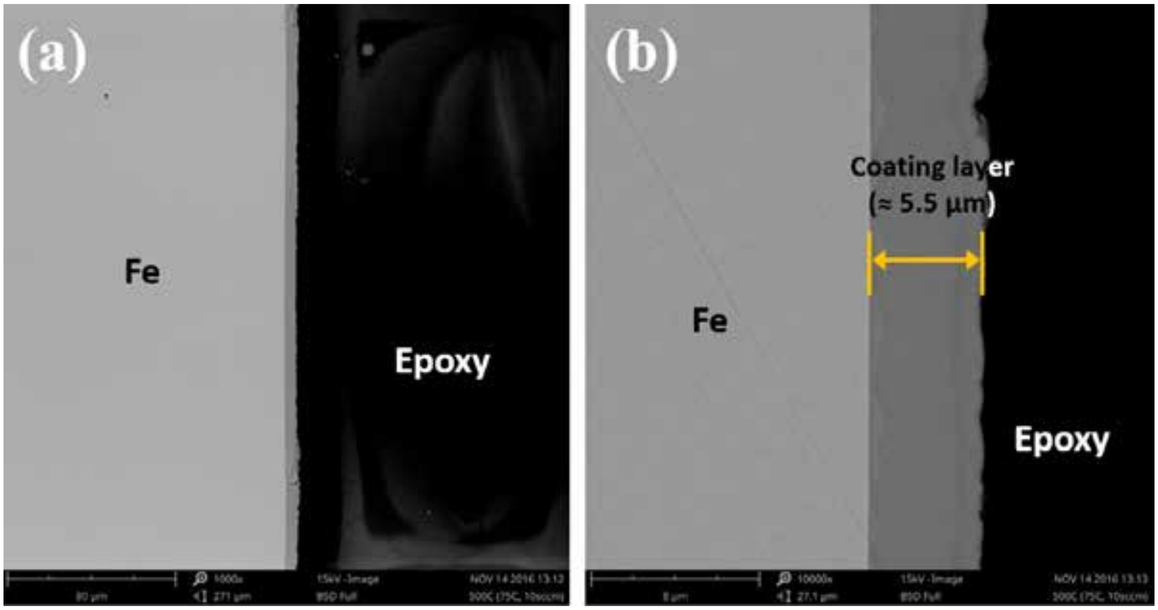

Figure 8-22. (a) Low (×1000) and (b) high (×10000) magnifications SEM cross sectional images taken at the center of the specimen. The sample was deposited at 500 ^{o}C with the flow rate of 15 sccm and the precursor temperature of 75 ^{o}C.

8.1.4. Sample Position in the Chamber

Sample position in the chamber is also important factor since mass transfer (e.g. the injection of the vaporized precursor) by diffusion and convection determine the access of reactants to the deposition surface. However, effects of standard CVD operating conditions (e.g. flow rate, pressure of the system, and types of carrier gas) on flow characteristics are hard to consider. Therefore, in this project, the position of the sample was determined empirically. Figure 8-23a shows top and side views of the chamber after the test under the flow rate of 15 sccm. Precursors were also deposited on the wall of the chamber, and it is clearly seen that most deposition occurred in the middle of the chamber where the specimen placed. However, not all over the specimen, but only the middle of the sample was covered with soot after the test, indicating that carrier gas was directly injected on the specimen (Figure 8-23b). This is probably due to the fact that the specimen was too close to the nozzle, therefore, it directly hit the specimen, and has not enough time for the surface of the specimen to be deposited.

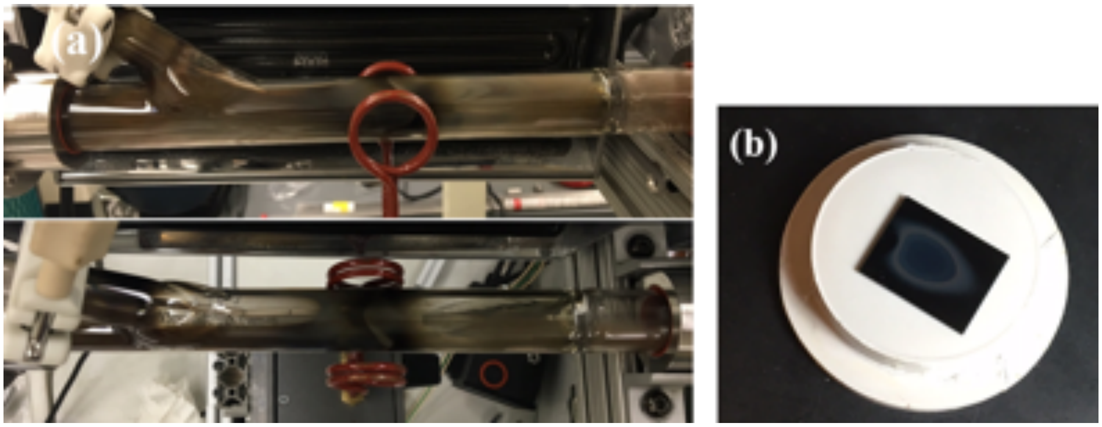

Figure 8-23. (a) Top and side views of the chamber after the test under the carrier gas flow rate of 15 sccm. (b) The specimen after the test. The middle of the sample was covered with soot.

Figure 8-24a shows top and side views of the chamber after the test under the higher flow rate of 20 sccm. The precursor deposition characteristics on the wall shows different pattern that the vaporized precursors mainly deposited at the end of the chamber where an additional arm located, while the sample position in the chamber was the same (middle of the chamber). In this case, most surface area of the specimen was covered with the coatings. However, SEM images in Figure 8-25 show that not only the front of the sample (Figure 8-25b), but also the back side of the sample (Figure 8-25c) were deposited, implying that higher flow rate of the carrier gas promoted a turbulence near the specimen. Therefore, it will be considered to place the specimen at the end of the chamber for our future work.

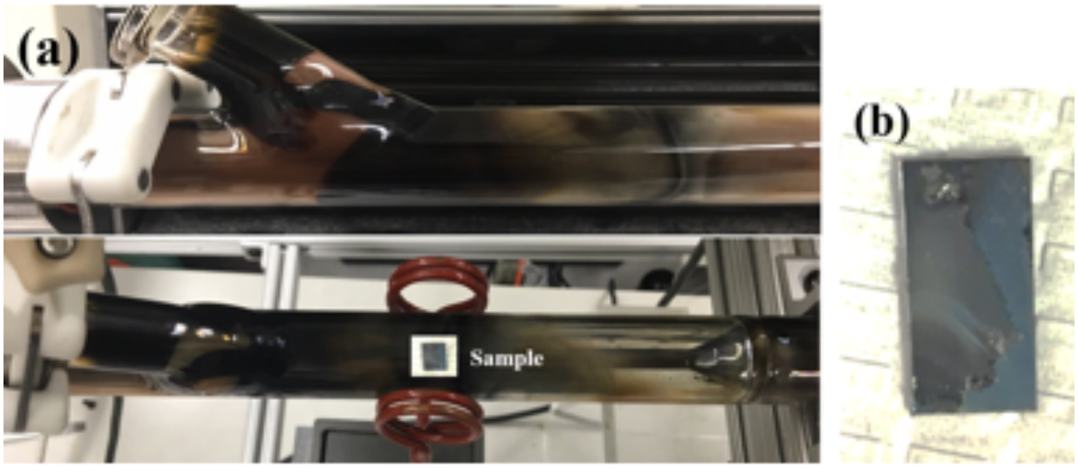

Figure 8-24. (a) Top and side views of the chamber after the test under the carrier gas flow rate of 20 sccm. (b) The specimen after the test.

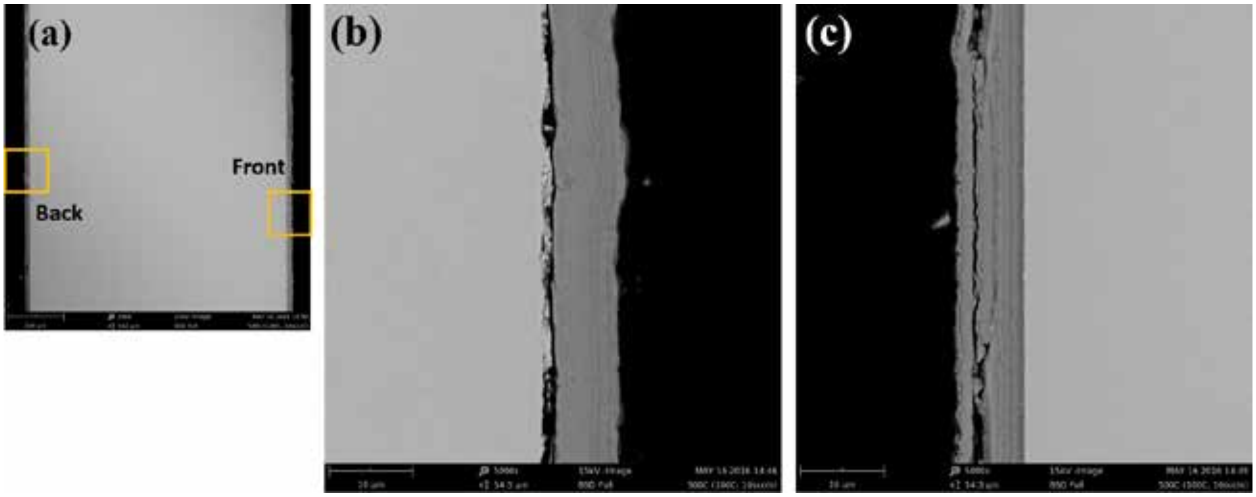

Figure 8-25. (a) Low magnification of SEM image of the sample, showing both front and back sides. Higher magnification (×5000) SEM images of (b) front, and (c) back of the specimen. Both sides show de-adhesion between T91 substrate and the coating.

8.1.5. Coating Time of OMCVD

So far, the coating experiment usually took place for 20 hrs in order to minimize the effect of time on coating performance. However, we found the difference in color and stoichiometry on surface of the flat coupon after finishing the test. After using up the precursor, we kept the evaporator valves open and left it for 20 hours, and it became sooty on the sample after 8 hrs (Figure 8-26). The SEM results show that the image and the EDS spectra were quite different between two different regions. Figure 8-27a shows SEM surface morphology of the specimen at the bottom of the sample, which represented a gray color (bottom of the sample in Figure 8-26). The sample was deposited at 500 ^{o}C with the flow rate of 20 sccm and the precursor temperature of 70 ^{o}C. It seems that all surface was fully covered with vanadium carbide. The average grain size of the coated particle was approximately 9 µm. EDS result in Figure 8-27b also confirms that the specimen was fully covered. The compositions was 51 at.% V-49 at.% C. Lower magnification image in Figure 8-28 also shows that most area on the specimen was fully covered with vanadium carbide. The SEM cross sectional image in Figure 8-29 shows that the coating with approximately 6 µm was deposited on the surface of the T91 steel. There was no gap or de-adhesion between the substrate (T91) and the coating.

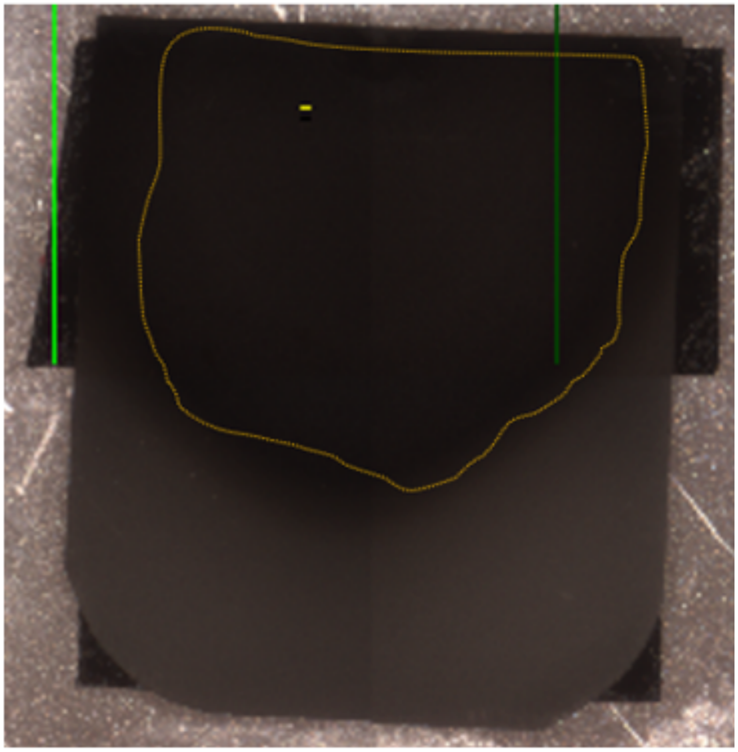

Figure 8-26. Optical image for the sample after the test. The area within the dashed line represents sooty spot after the test.

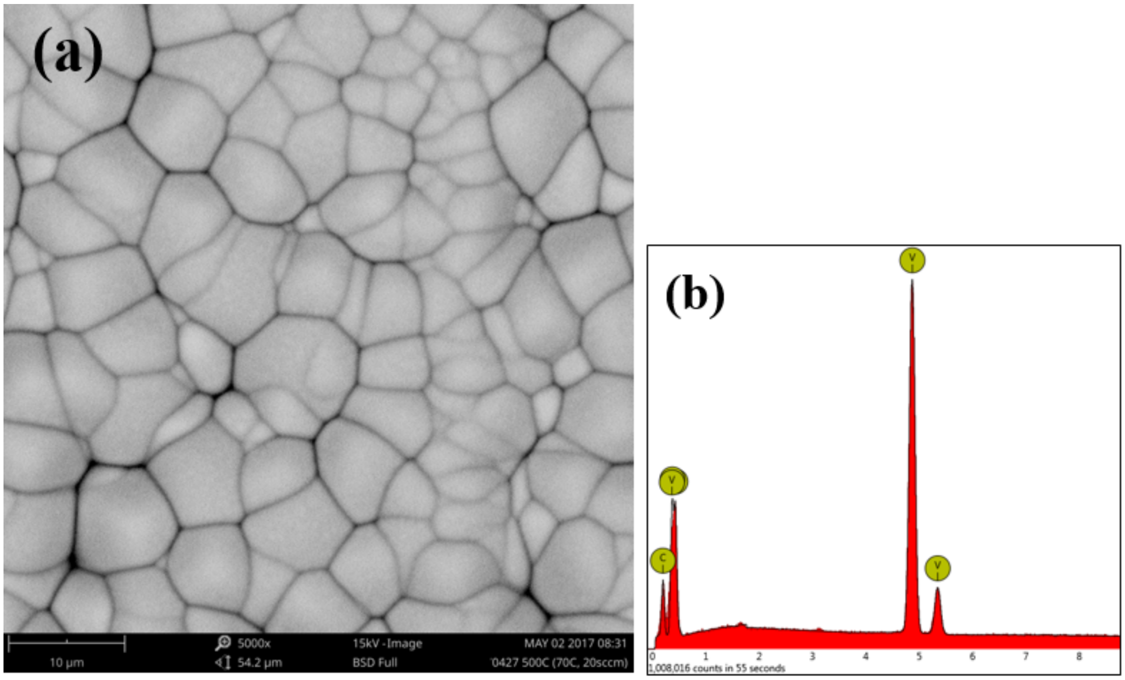

Figure 8-27. (a) SEM surface morphology of the specimen and (b) EDS spectra. The sample was coated at 500 °C with the flow rate of 20 sccm and the precursor temperature of 70 °C. The sample was coated for 20 hrs.

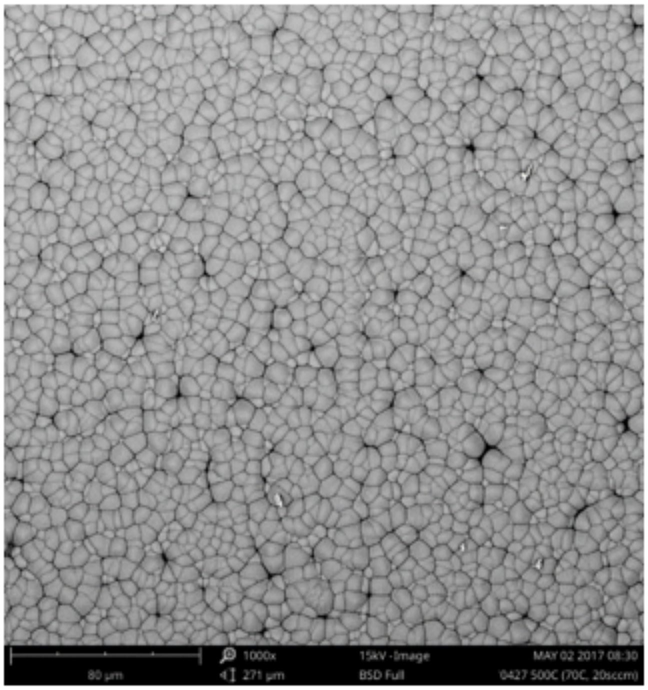

Figure 8-28. Lower maginification (×1000) SEM surface morphology of the specimen deposited at 500 °C with the flow rate of 20 sccm and the precursor temperature of 70 °C.

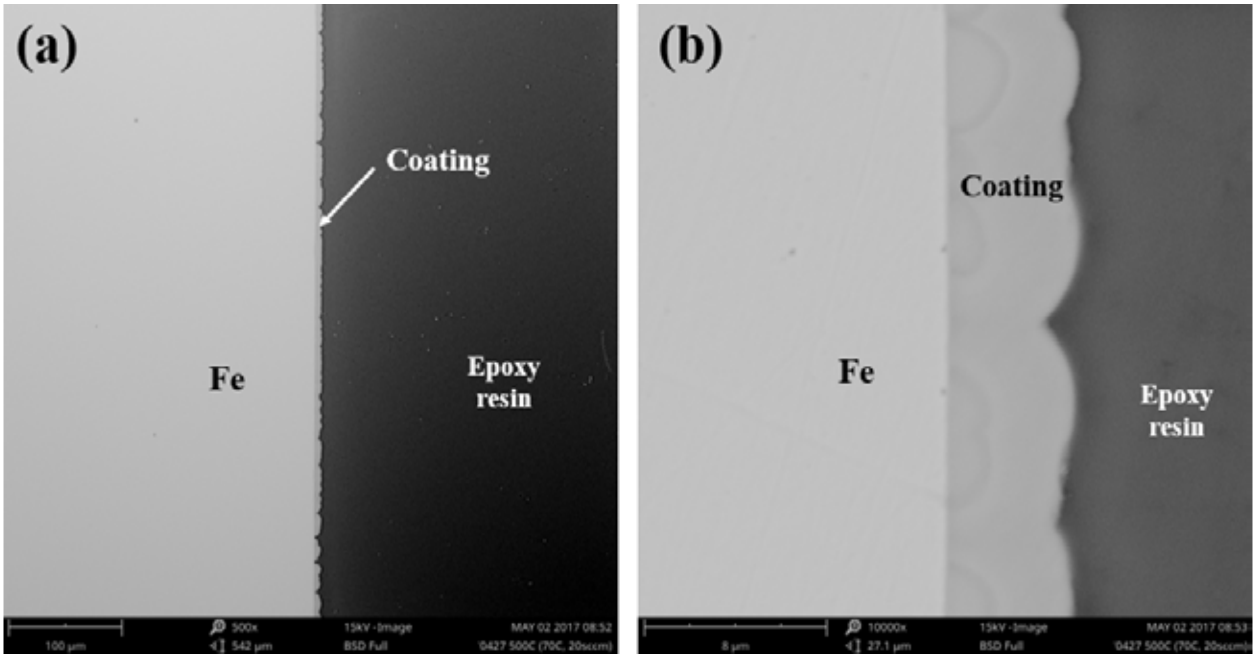

Figure 8-29. (a) Low (×500) and (b) high (×5000) magnifications SEM cross sectional images deposited at 500 ^{o}C with the flow rate of 20 sccm and the precursor temperature of 70 ^{o}C.

However, SEM result in Figure 8-30 shows that the surface was not fully covered with vanadium carbide. The image was taken from the top of the sample, which is the marked area within the dashed line. Figure 8-30a shows some area was barely revealed. The EDS spectrum further confirms that the spot in the particle has a composition of 47 at.% V-52 at.% C-1 at.% Fe (Figure 8-30b). However, the EDS result taken from the spot marked as ‘x’ was 27 at.% V-38 at.% C-27 at.% Fe-8 at.% Cr, indicating that bare Fe was detected in the EDS result (Figure 8-30c).

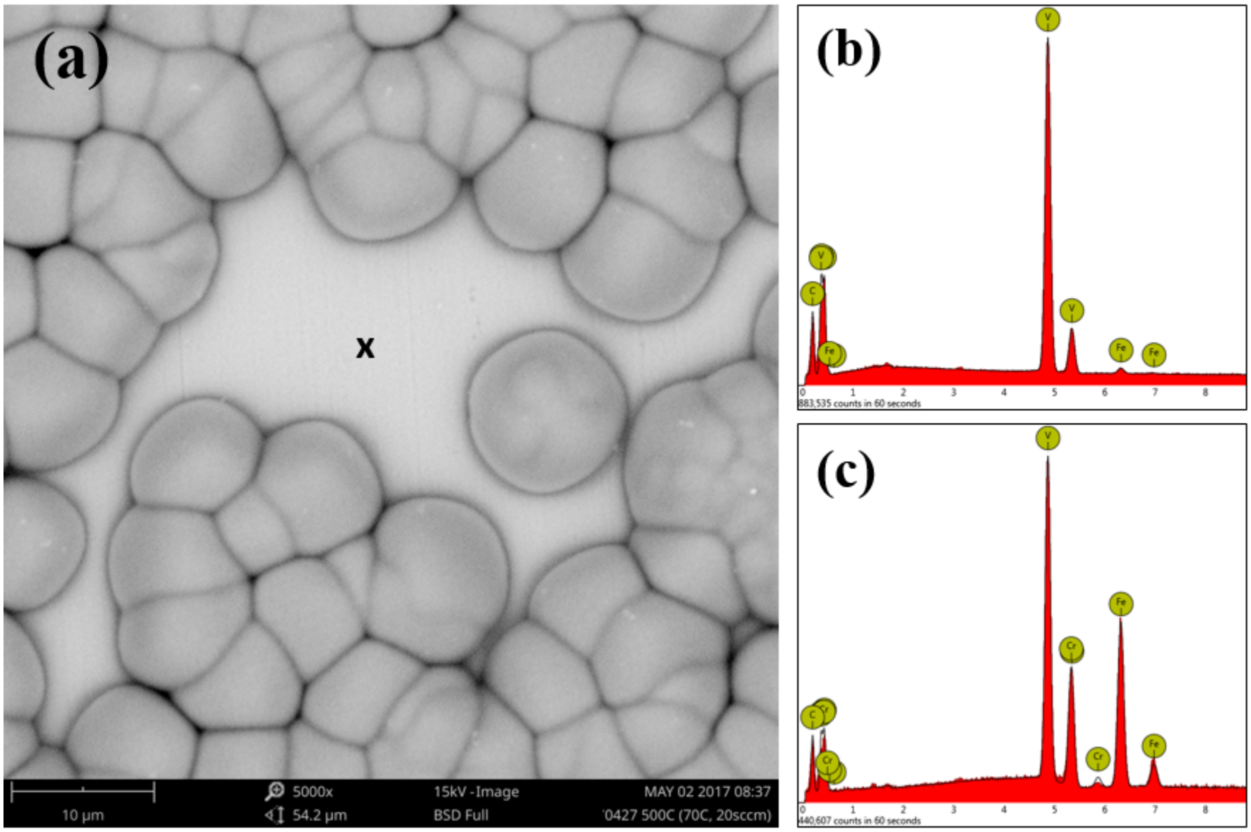

Figure 8-30. (a) SEM surface morphology and (b) EDS spectra of the sample coated at 500 °C with the flow rate of 20 sccm and the precursor temperature of 70 °C.

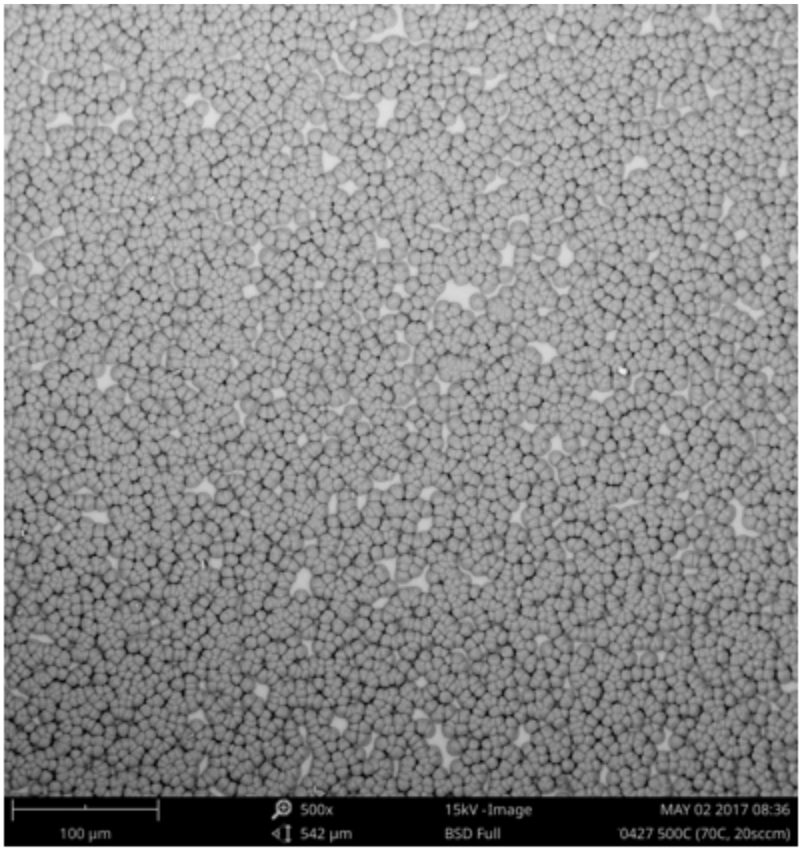

Figure 8-31. (a) Lower magnification (×1000) SEM surface morphology of the sample coated at 500 ^{o}C with the flow rate of 20 sccm and the precursor temperature of 70 ^{o}C.

Lower magnification SEM surface image (Figure 8-31) and SEM cross section images (Figure 8-32) also show that the surface was not fully covered. As we monitored the surface of the sample and the parameter in the system during the test, it is thought that all precursor was used up after approximately 3 hrs, since there is little change in total pressure. Then, after approximately 8 hrs, the sample became sooty from the top of the sample, which is probably the spot where the carrier gas hit. Therefore, it is thought that 20 hrs test time was not necessary, and it is expected that the experiment with shorter time might show a better coating performance.

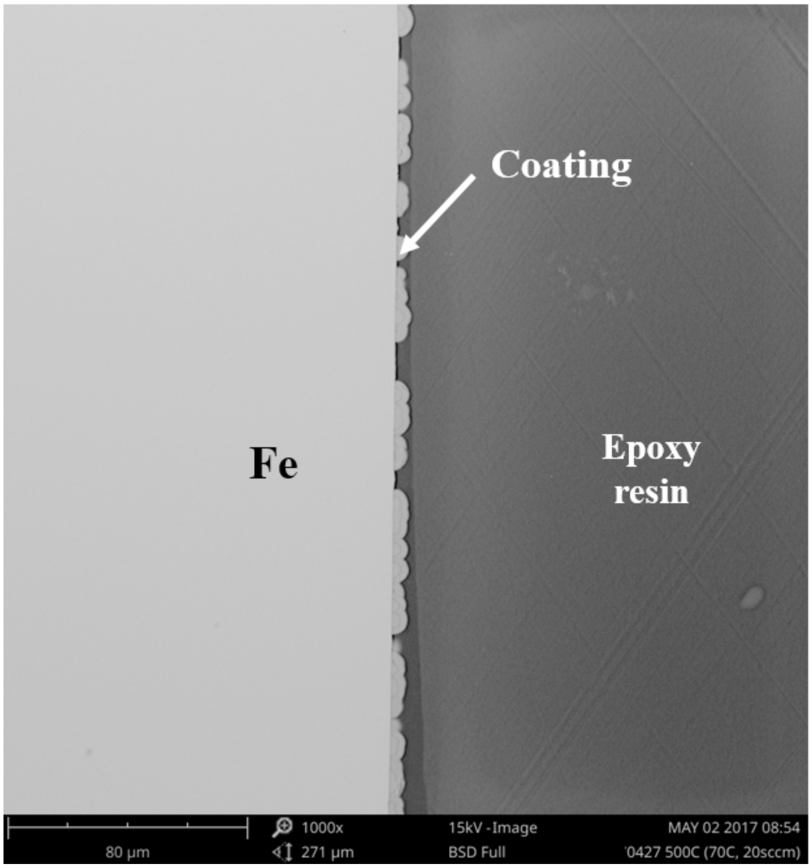

Figure 8-32. SEM cross sectional images of the specimen. The sample was deposited at 500 ^{o}C with the flow rate of 20 sccm and the precursor temperature of 70 ^{o}C.

Figure 8-33 shows the SEM surface morphologies of the sample coated at 500 ^{o}C with the flow rate of 20 sccm and the precursor temperature of 70 ^{o}C. The sample was coated for 10 hrs. After the experiment, the sample has a single gray color surface, and there is no sooty area over the specimen. The gain size of the coating was approximately 8.5 µm, which is quite comparable to the grain size of the sample coated for 20 hrs. The quality of the coating was good. There was no bare region on the surface of the sample, which was not covered with a coating. Therefore, it is thought that a coating with shorter time of 10 hrs was enough with using 1 g of vanadocene in our system, and it is thought that there is no impact of grain size and coating quality by reducing a coating time.

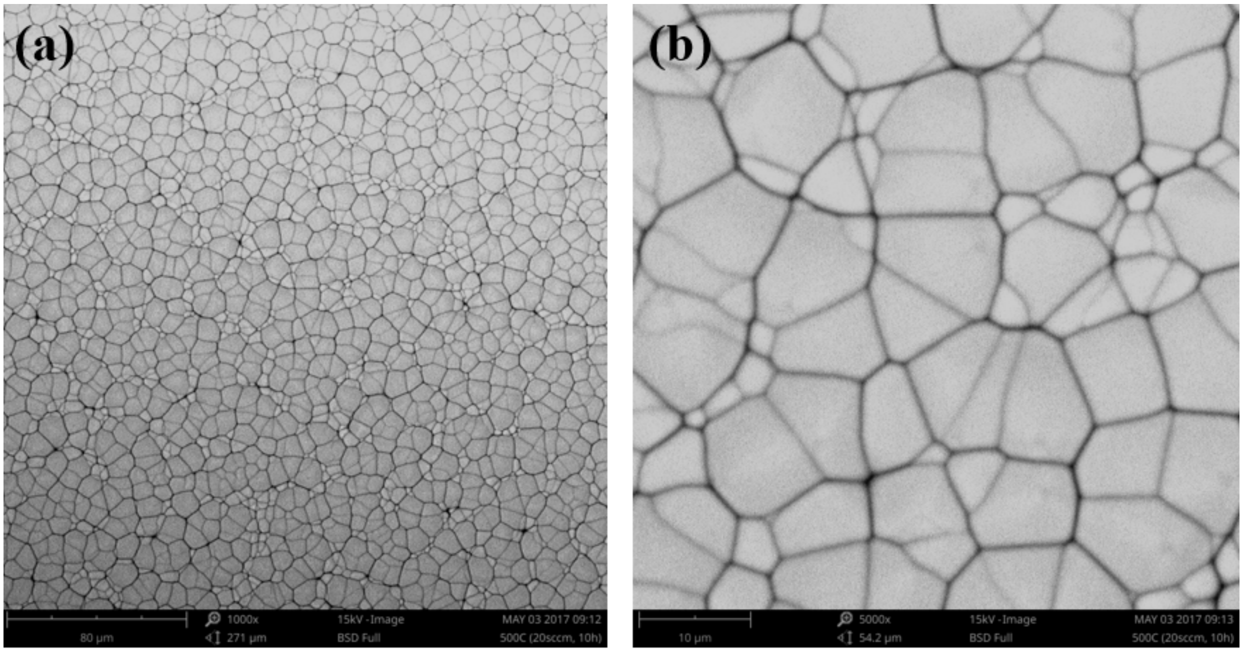

Figure 8-33. (a) Low (x1000) and (b) high (x5000) magnifications SEM surface morphologies of the sample coated at 500 ^{o}C with the flow rate of 20 sccm and the precursor temperature of 70 ^{o}C. The sample was coated for 10 hrs.

8.1.6. Cooling Rate of the Sample after Experiments

In general, grade T91 exhibits excellent elevated-temperature strength and creep behavior up to approximately 600 °C [25]. In addition, T91 steel has higher heat transfer and lower coefficients of thermal expansion (CTE) compared with austenitic steels [26]. However, when the vanadium carbide, which has relatively lower CTE value than T91 steel, deposits on the surface of the cladding materials, thermal cracks would occur as a result of the discrepancy of the CTE values between the coating and the cladding material. Figure 8-34 shows a specimen after the coating experiment, showing that a coating initially took place on the flat coupon sample, but it was peeled off afterward probably because of a rapid cooling rate of approximately 100 ^{o}C/sec. As a result, shiny gray surface revealed, while a small amount of dark gray area, which is a coated region, was remained.

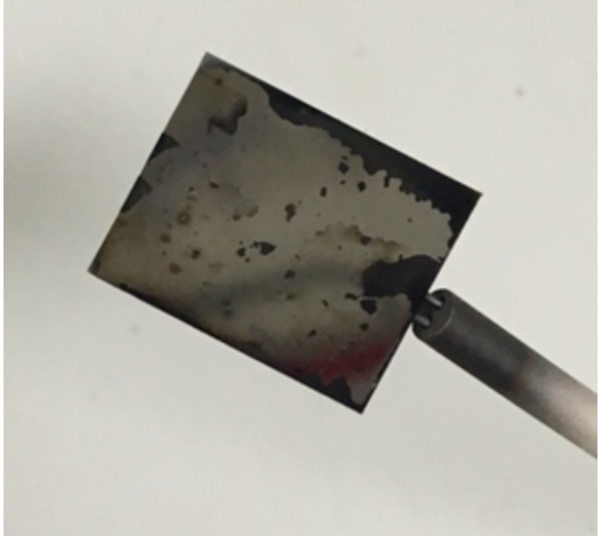

Figure 8-34. The sample after the coating experiment. Most of the coating was peeled off.

The coating experiment with slower cooling rate (20 ^{o}C/min) was followed to inhibit the gap or de-adhesion probably due to the difference in CTE. Figure 8-35a shows that the cooling rate of 20 ^{o}C/min seems still not enough to prohibit the cracking. After the deposition, the cracking occurred at the surface of the specimen. In addition, C content at the surface of the coating was relatively higher (Figure 8-35b, 78 at.%) than other coating experiments, indicating that high content of C might expedite the cracking at the surface. The cross-section images in Figure 8-36 shows that the approximately 10 μm thick coating layer was deposited on the specimen. However, the coating layer was also not uniform (Figure 8-36b). During the test, there was a fluctuation in total pressure, which occurred from the blockage of the precursor at the system. It is thought that the blockage might occur when the gas flow injection was not enough to bring the vaporized precursor into the chamber, so that there was a stagnant vaporized species at the evaporator. Therefore, another experiment with higher flow rate was performed.

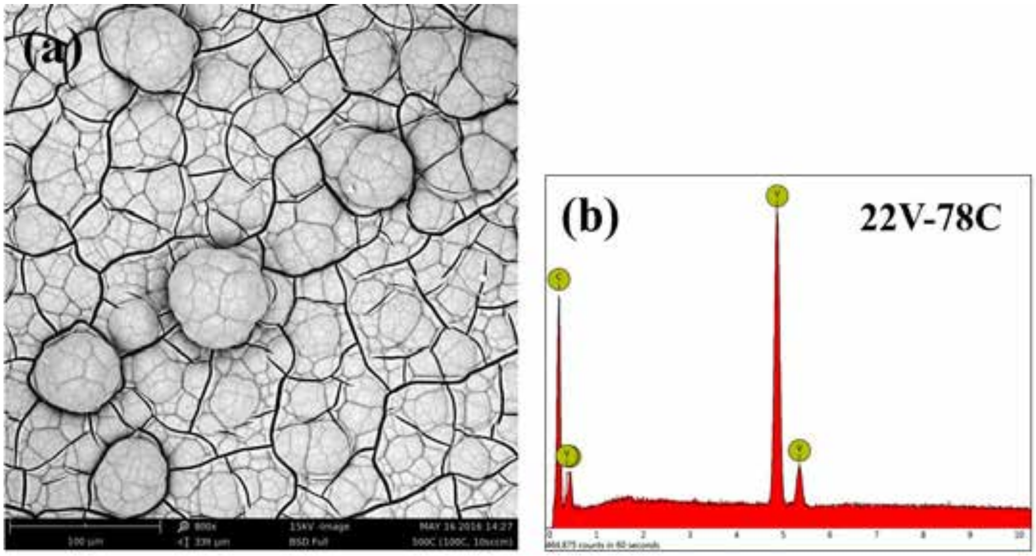

Figure 8-35. (a) SEM surface morphology and (b) EDS profile deposited at 500 ^{o}C with the flow rate of 10 sccm.

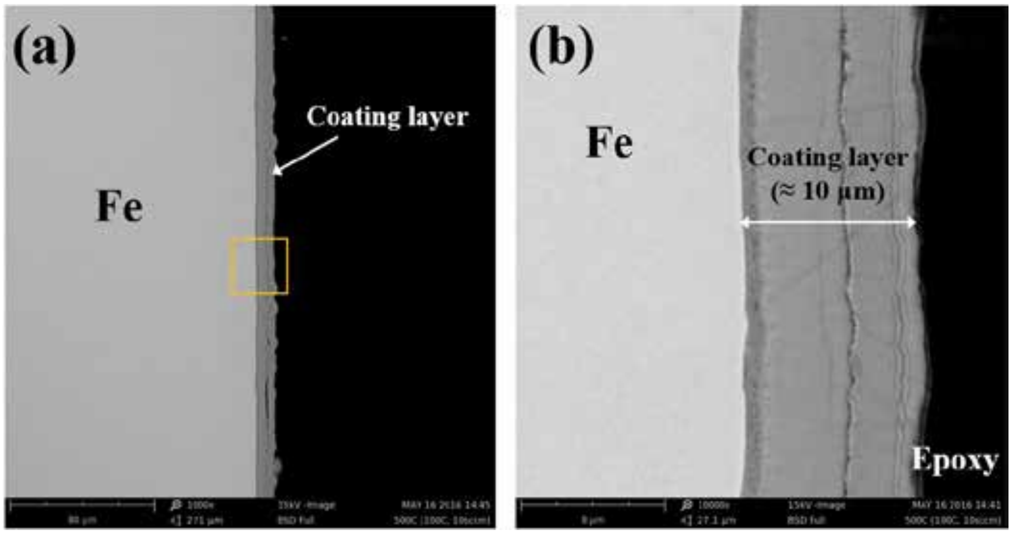

Figure 8-36. SEM cross sectional images at (a) low and (b) high magnifications deposited at 500 ^{o}C.

Figure 8-37a shows the SEM surface morphology. Well-developed grain structure with micron scale grain size was obtained under the substrate temperature of 400 ^{o}C for 20 h with the flow rate of 10 sccm. The EDS spectra in Figure 8-37b further confirms that the surface of the T91 steel was well-covered, and the coating contains both V (67.6 at.%) and C (33.4 at.%), no peaks for Fe, Si, and Cr was detected. Low magnification SEM surface morphology image in Figure 8-38 also shows most area of the specimen was well-deposited with V and C atoms. The SEM cross section image in Figure 8-39 shows that approximately 6 μm thick solid coating layer was developed. There are no distinct gap or de-adhesion between T91 substrate and the coating, since the specimen was cooled down at lower rate of 10 °C/min. In summary, it is thought that adequate gas flow and pump rates as well as slow cooling rate is necessary in order to obtain a good quality coated specimen.

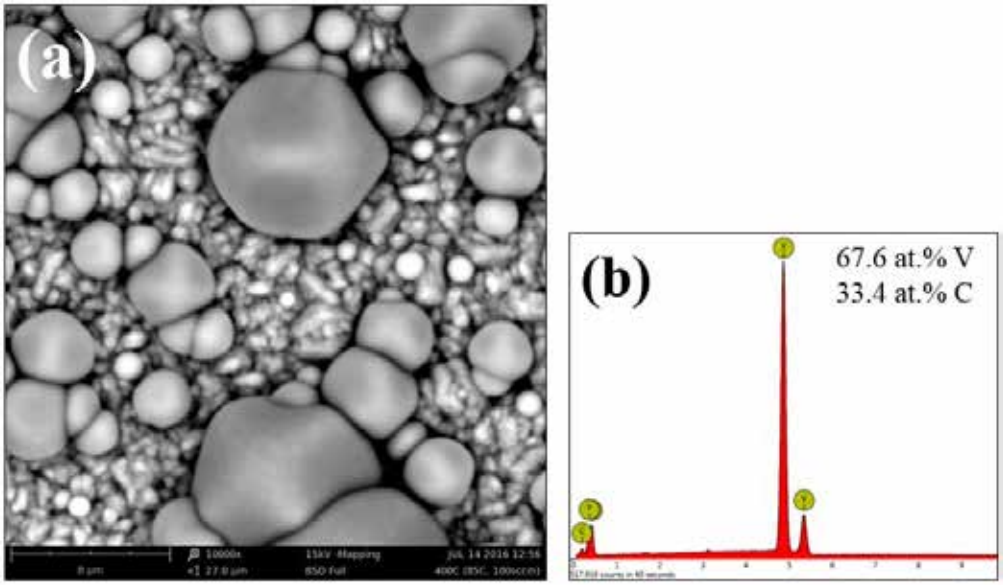

Figure 8-37. (a) SEM surface morphology and (b) EDS profile deposited at 400 °C with the flow rate of 10 sccm.

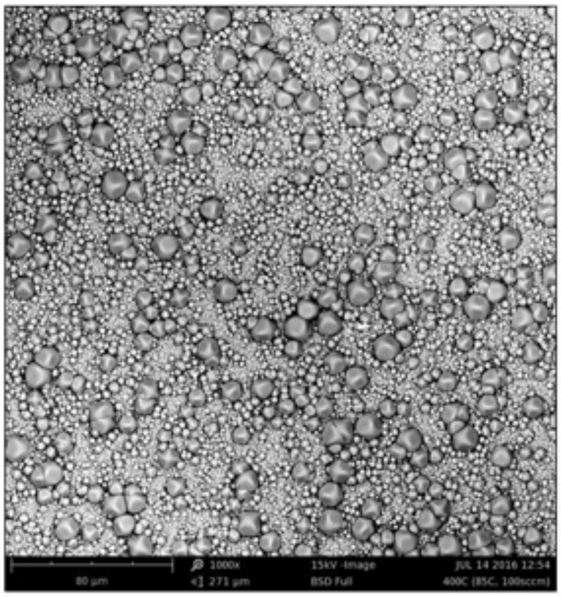

Figure 8-38. SEM surface morphology taken at lower magnification (×1000). The specimen was fully covered with particles.

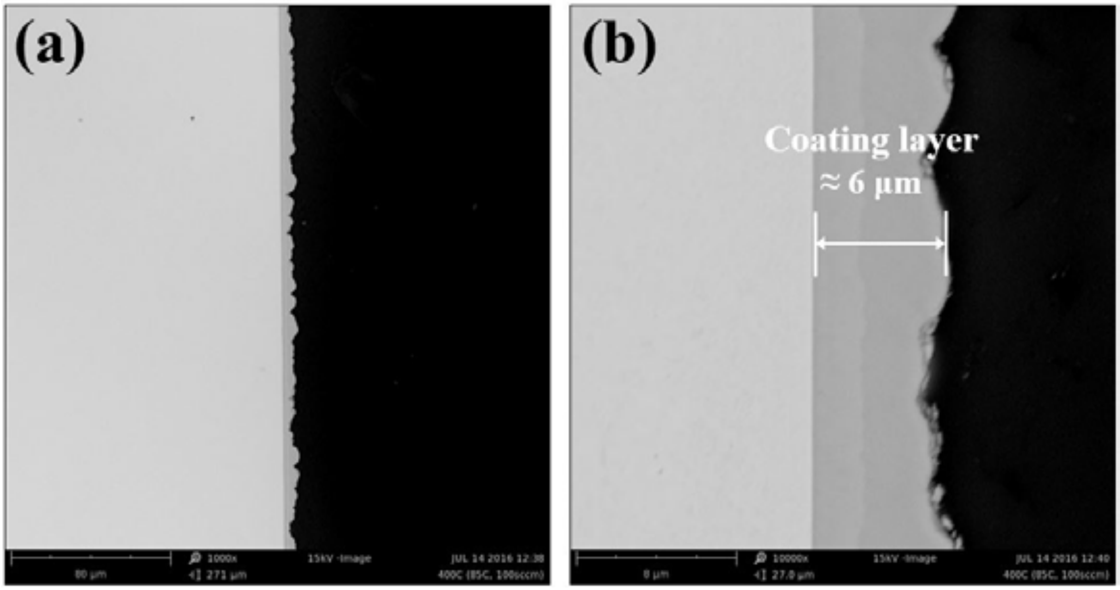

Figure 8-39. SEM cross sectional images at (a) low and (b) high magnifications deposited at 400 °C.

Another experiment with slow carrier gas flow rate (10 sccm) and cooling rate (10 °C/min) was also performed. Figure 8-40a shows the surface morphology of the coating obtained with the Cp_2V precursor at 400 °C with the carrier gas flow rate of 10 sccm. A well-developed coating was obtained, and the EDS spectra in Figure 8-40b shows that the coating contains both V (48.2 at.%) and C (51.8 at.%), no peaks for Fe, Si, and Cr was detected, indicating that the surface of the T91 steel was well-covered with V and C atoms.

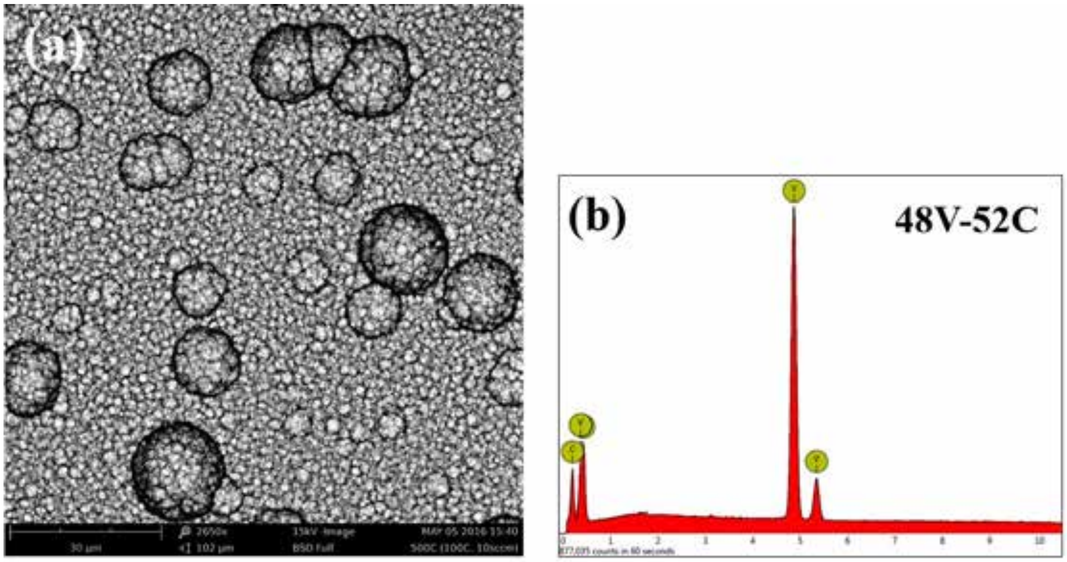

Figure 8-40. (a) SEM surface morphology and (b) EDS profile deposited at 400 °C with the flow rate of 10 sccm.

The low magnification cross-sectional SEM image in Figure 8-41a shows that the coating with uniform thickness was developed at the surface of the T91. The thickness of the coating was approximately 20 µm, which is the thickest result so far (Figure 8-41b). However, the higher magnification image in Figure 8-41b shows that there is a gap and de-adhesion between the coating and T91 substrate. This is probably due to the high deposition rate or a discrepancy in CTE between T91 steel and the vanadium carbide coating during cool-down after the test [27]. In addition, multiple layers in the coating was observed, which proved to be a C-rich layer in EDS line scan profile (Figure 8-42).

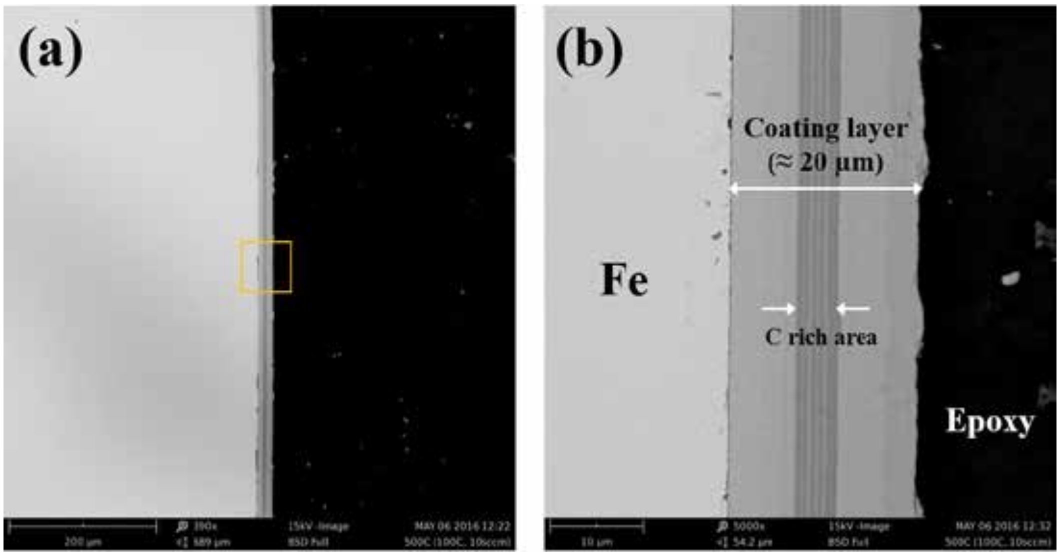

Figure 8-41. SEM cross sectional images at (a) low and (b) high magnifications deposited at 400 °C.

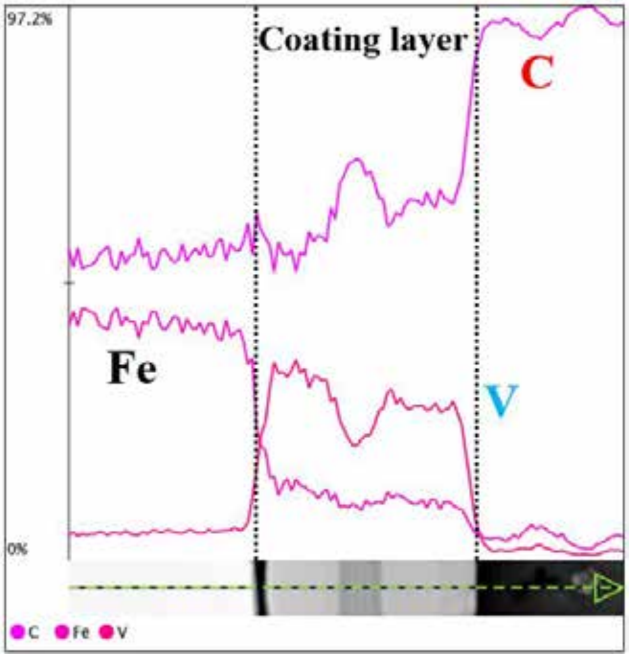

Figure 8-42. EDS line scan profile of the specimen coated at 400 °C. C-rich region presented in the coating.

8.1.7. Phase Constituent

Figure 8-43 shows the X-ray diffraction from the vanadium carbide coating deposited at 400 °C (Figure 8-4a) and 500 °C (Figure 8-4b). In addition to the EDS result in Figure 8-4, the X-ray result in Figure 8-43 further confirms that the coating is consisted of a mixture of V_2C, VC and a small amount of V_2O_3.

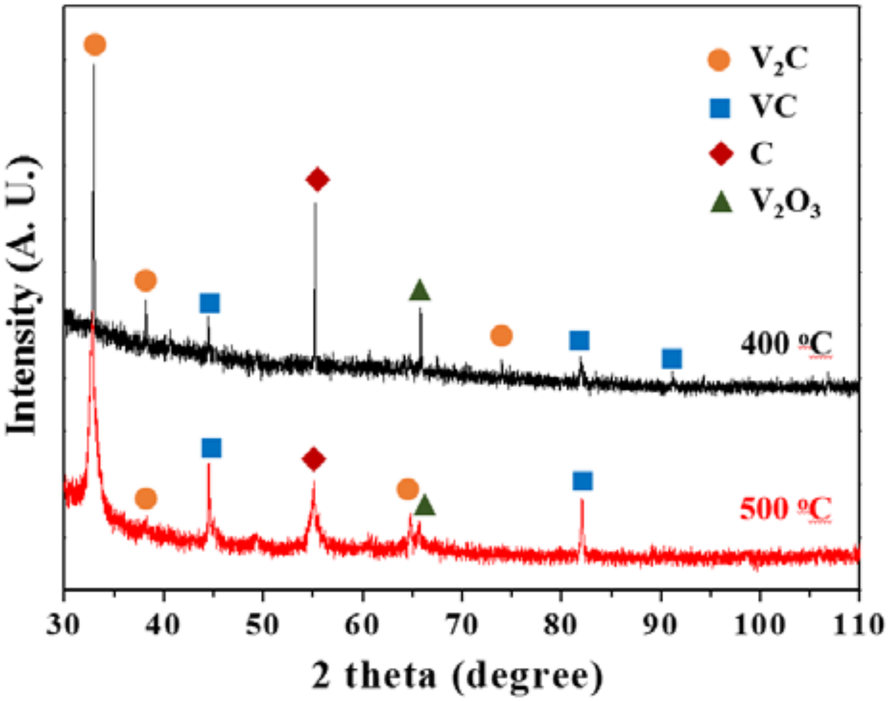

Figure 8-43. X-ray diffraction from the vanadium carbide coating deposited at 400 ^{o}C and 500 ^{o}C.

8.1.8. Composition Analyses by Using TEM

The cross-sectional TEM was also prepared by using FIB, which is shown in Figure 8-44. The cross-sectional TEM image shows that the microstructures such as the grain and carbide in T91 substrate remain intact.

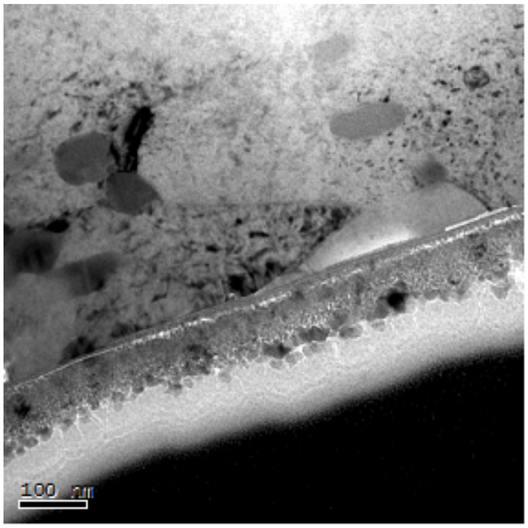

Figure 8-44. Cross sectional TEM image of the coated T91 substrate.

Figure 8-45 shows a TEM Cross-sectional image of the sample coated at 450°C. The sample was deliberately lifted out from an area with a thin coating layer, which contains a small grain size. The coating shows a uniform thickness of ~2.5 µm, and it is further confirmed that there is no gap or de-adhesion between HT9 and the coating.

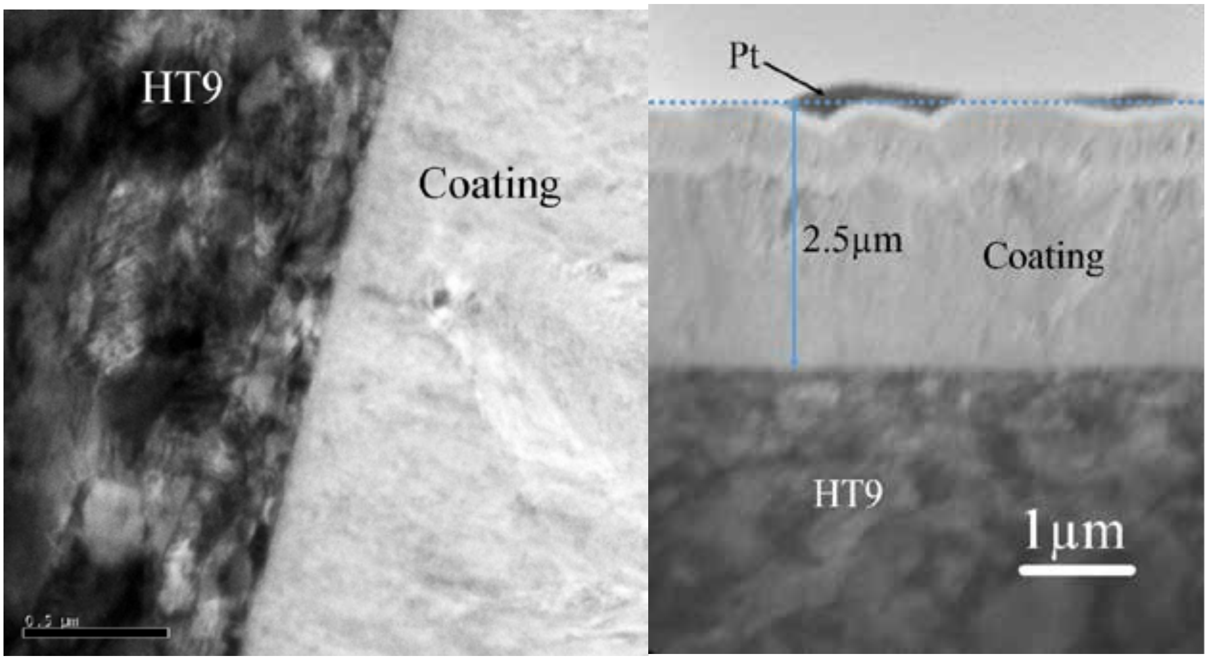

Figure 8-45. TEM Cross-sectional image of the sample coated at 450°C after FIB lift out.

8.1.9. Application to the Tubular T91 Sample

Figure 8-46 shows a preliminary design for the tubular coating apparatus. A preliminary coating result at the inner surface morphology of the cladding material is shown in Figure 8-46b. It is shown that the surface of the inner cladding was not fully covered with the coating. The possible reason for the irregular coating is because that the inner surface is just as extruded, and/or a much thicker coating would be needed to fully cover the inner surface. Therefore, further design and development was performed to improve the coating uniformity as well as application to a longer cladding tube in Figure 8-47. In order to measure the exact temperature, and keep the temperature of the tubular sample consistent, the actual cladding tube was directly attached with the thermos couple by using a spot welder. Then, the sample was loaded and placed at front of the nozzle in the reaction chamber.

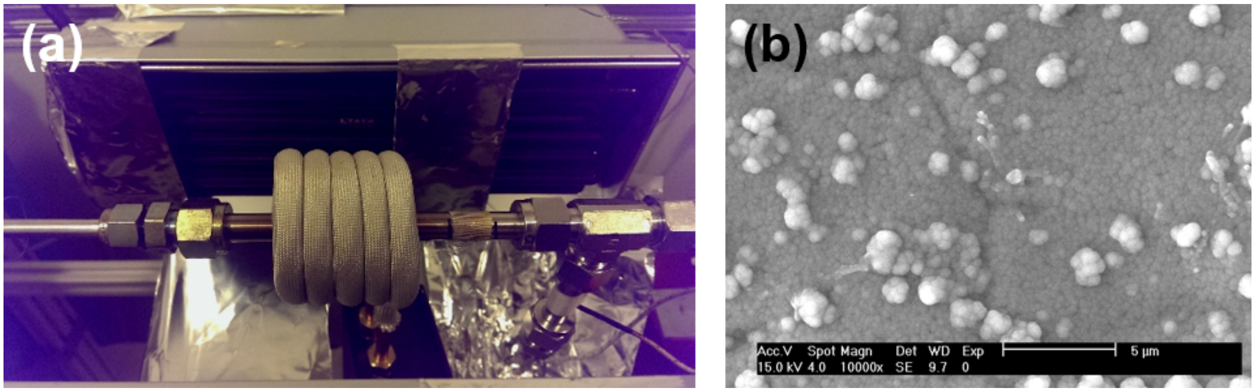

Figure 8-46. (a) Preliminary setup for tubular coating experiments, and (b) surface morphology of the tube inner coating.

Figure 8-47. (a) The actual cladding tube directly attached with the thermos couple by using a spot welder. (b) The sample loaded at front of the nozzle in the reaction chamber.

The coating experiment for the tubular T91 cladding sample was performed under the substrate temperature of 450 ^{o}C and the carrier gas flow rate of 10 sccm. After the test, the precursor was not fully passed through the tip probably because of the limited flow rate of the precursor due to the change in the reaction chamber (especially, the nozzle tip might cause a limitation of the carrier gas flow along with the precursor. The cross section images of the inner surface was also shown in Figure 8-48, which are three different regions in the tubular sample. Unlike the front (Figure 8-48b) and the rear (Figure 8-48d) side of the sample, a thicker coating with some gap between the coating the inner surface was observed in the middle of the tubular cladding specimen (Figure 8-48c). This is probably due to the fact that there was less turbulence generated in the middle of the cladding, resulting in favorable condition for the precursor to be deposited.

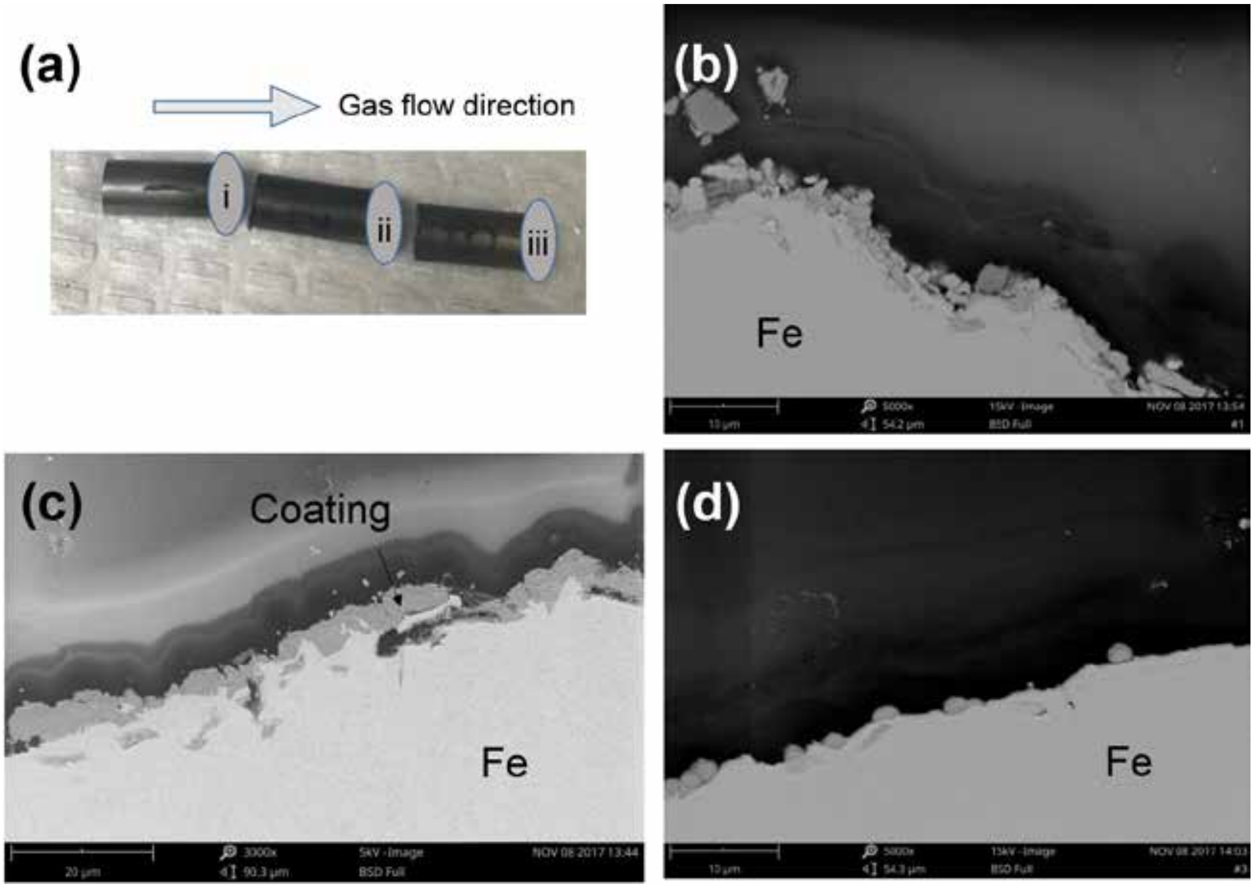

Figure 8-48. (a) Sectioned cladding tube. The gas flows from left to right direction. Cross section images of the inner cladding surface at each area of (b) i, (c) ii, and (d) iii under the substrate temperature of 450 °C and the carrier gas flow rate of 10 sccm.

8.2 Effects of Vanadium Carbide Coating Layer to Inhibit the FCCI

8.2.1. Diffusion Couple Studies at Normal Operating Temperature of SFR

Figure 8-49 shows the back scattered electron (BSE) micrograph of cross-sectional image of samples after a diffusion couple experiment at 550°C for 100 h. An annealing temperature of 550 °C was adopted based on the normal operating temperature at which the fuel/cladding interface could be exposed. The average lengths of the inter-diffusion zone between T91 and Ce before and after the coating process were 125 μm and 25 μm, respectively. This indicates there is 80 % reduction in the inter-diffusion zone between the cladding and the fuel. However, it is not enough to mitigate FCCI since it is clearly seen that cerium atoms diffused toward iron substrate. This is probably attributed to the fact that a small coating thickness of 1.5 microns did not effectively inhibit inter-diffusion of both iron migration and lanthanide penetration [3]. Therefore, it is thought that another diffusion couple test needs to be performed using the specimen with thicker vanadium carbide deposition.

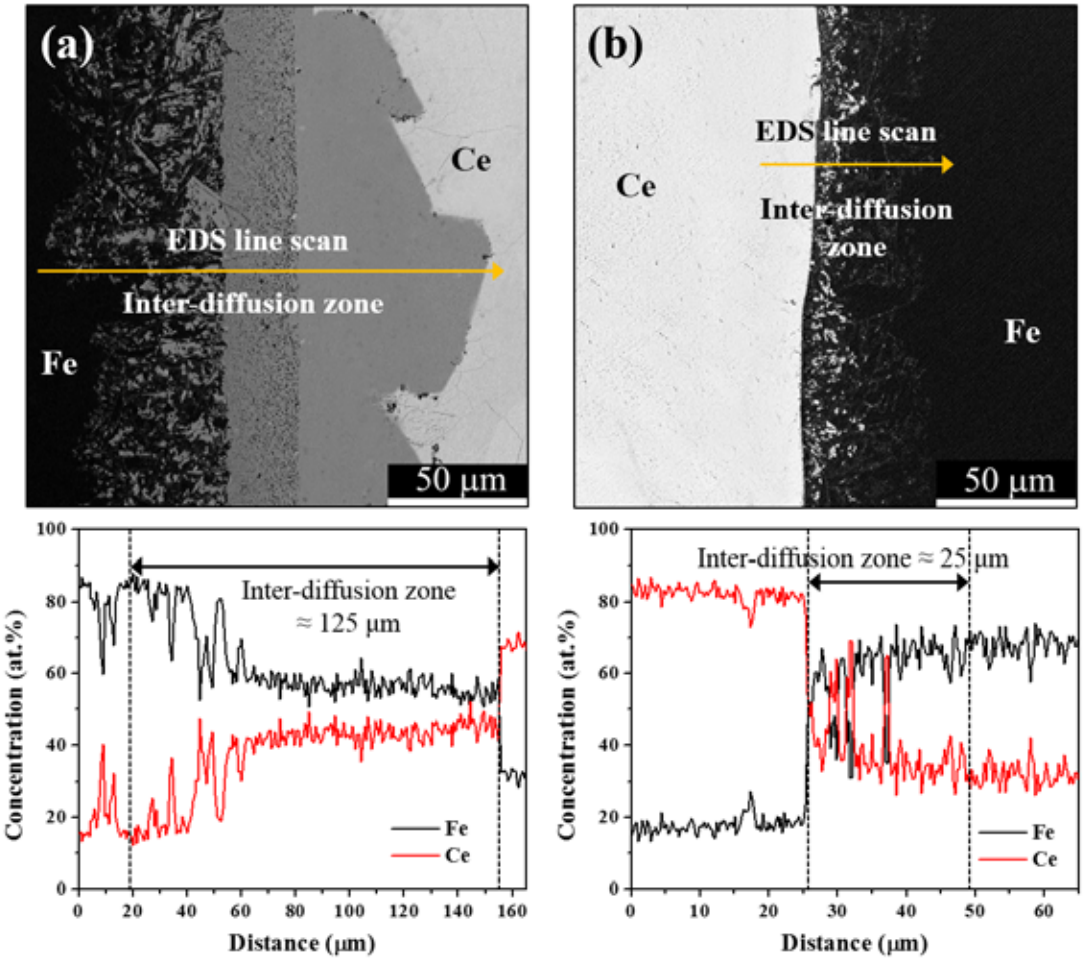

Figure 8-49. BSE micrograph of cross-sectional images (top) and concentration depth profiles (bottom) of samples after diffusion couple experiment at 550°C for 100 h. (a) T91/Ce and (b) T91/VC/Ce. The coating was deposited at 400 °C.

Thereafter, diffusion couple test was conducted at same temperature of 550 °C with the specimen having 5.5 µm thick coating (Figure 8-50). It was expected to get better results in terms of the reduction in inter-diffusion zone, since the specimen coated at 500 °C (5.5 µm) has thicker coating than that coated at 400 °C (1.5 µm). However, the result in Figure 8-50 shows that there is a little reduction in inter-diffusion zone (17% reduction). It is probably due to the fact that higher concentration of C atoms in the coating (approximately 50 at.%) acts as easier diffusion path for both Ce and Fe diffusion through the coating. Therefore, at this moment, it is thought that small concentration of C atoms with thicker coating is required to reduce inter-diffusion zone between Fe and Ce atoms effectively.

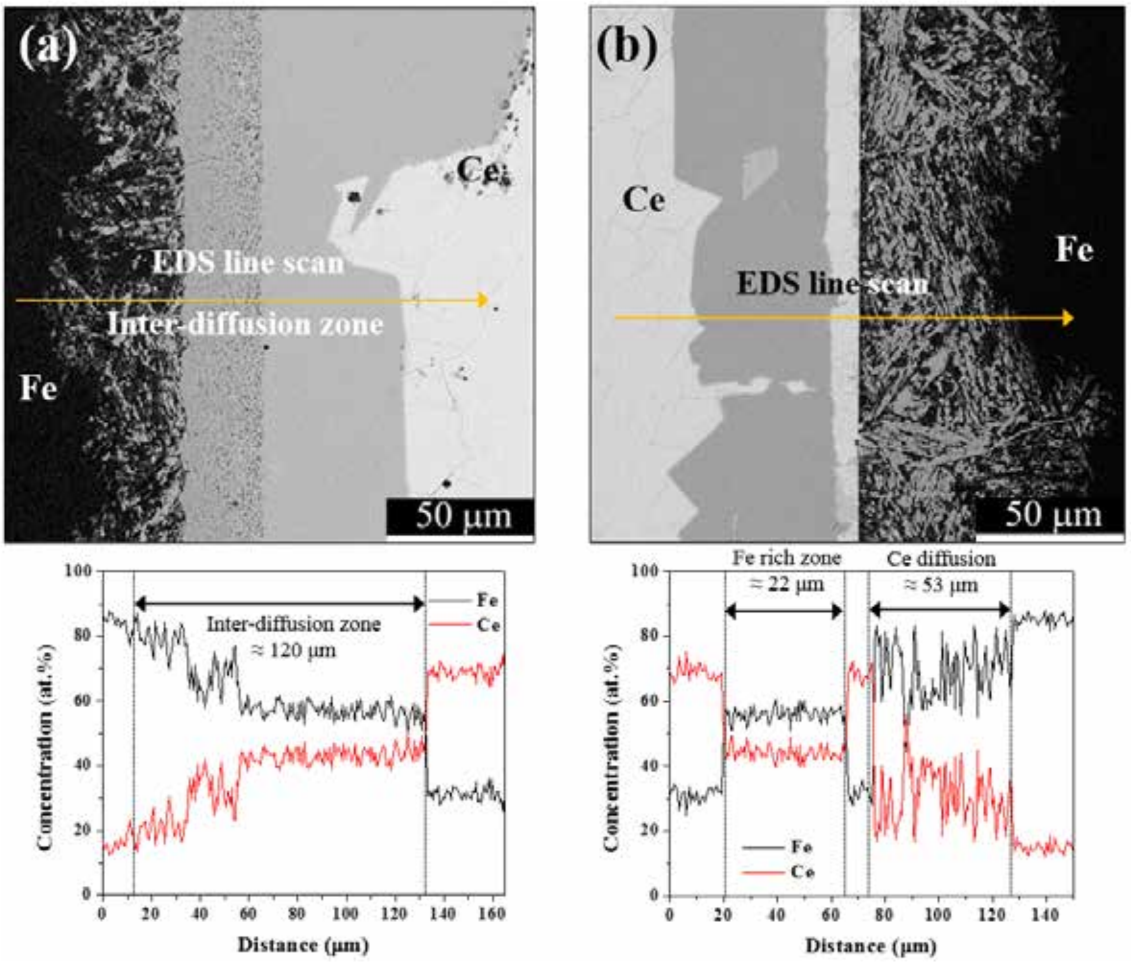

Figure 8-50. BSE micrograph of cross-sectional images (top) and concentration depth profiles (bottom) of samples after diffusion couple experiment at 550°C for 100 h. (a) T91/Ce and (b) T91/VC/Ce. The coating was deposited at 500 °C.

Figure 8-51 shows another BSE micrograph of cross-sectional image of samples after a diffusion couple experiment at 550 °C for 50 h. The average lengths of the inter-diffusion zone between T91 and Ce before and after the coating process were 65 µm and 25 µm, respectively. This indicates 62 % reduction in the inter-diffusion zone between the cladding and the fuel.

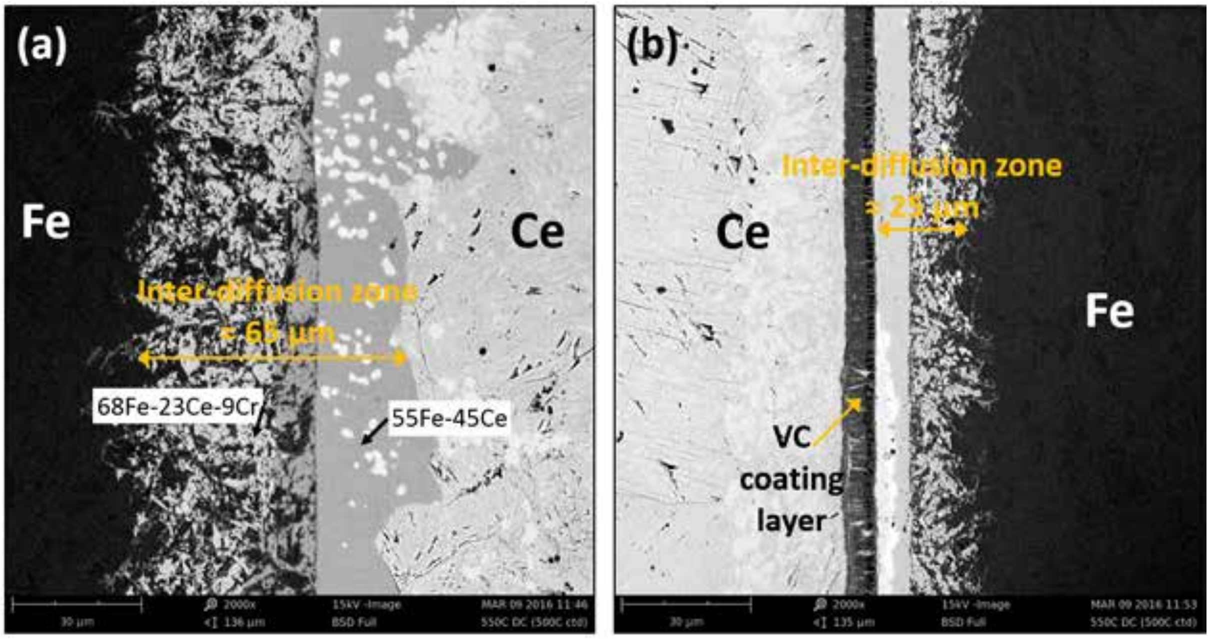

Figure 8-51. BSE micrograph of cross-sectional images after diffusion couple experiment at 550°C for 50 h. (a) T91/Ce and (b) Ce/VC/T91. The coating was deposited at 500 °C.

Figure 8-52 shows enlarged BSE cross-sectional images (x7000) of Ce/VC/T91 specimen with spot analyses on each spot. First, the composition at Ce substrate near the vanadium carbide coating layer was 100 wt.% Ce, which indicates that no Fe atoms diffuse toward Ce sheet. Therefore, it is thought that vanadium carbide coating layer mitigates the Fe diffusion efficiently, and act as a diffusion barrier. Ce diffusion, however, took place in the specimen through the vanadium carbide coating layer and T91. The length of Ce diffusion zone is approximately 25 µm.

In addition, the Fe/Ce inter-diffusion zone can be divided into two different regions in terms of its apparent shapes: one is solid gray region on the left near the vanadium carbide coating, and the other is debris-like particles on the right. It is uncertain that the particles was fabricated from the sample preparation process or not, since relatively soft Ce sheet could smear on the Fe substrate during mechanical polishing. Thus, surface mill trench process by using a FIB was performed in order to determine when the debris-like particles were fabricated.

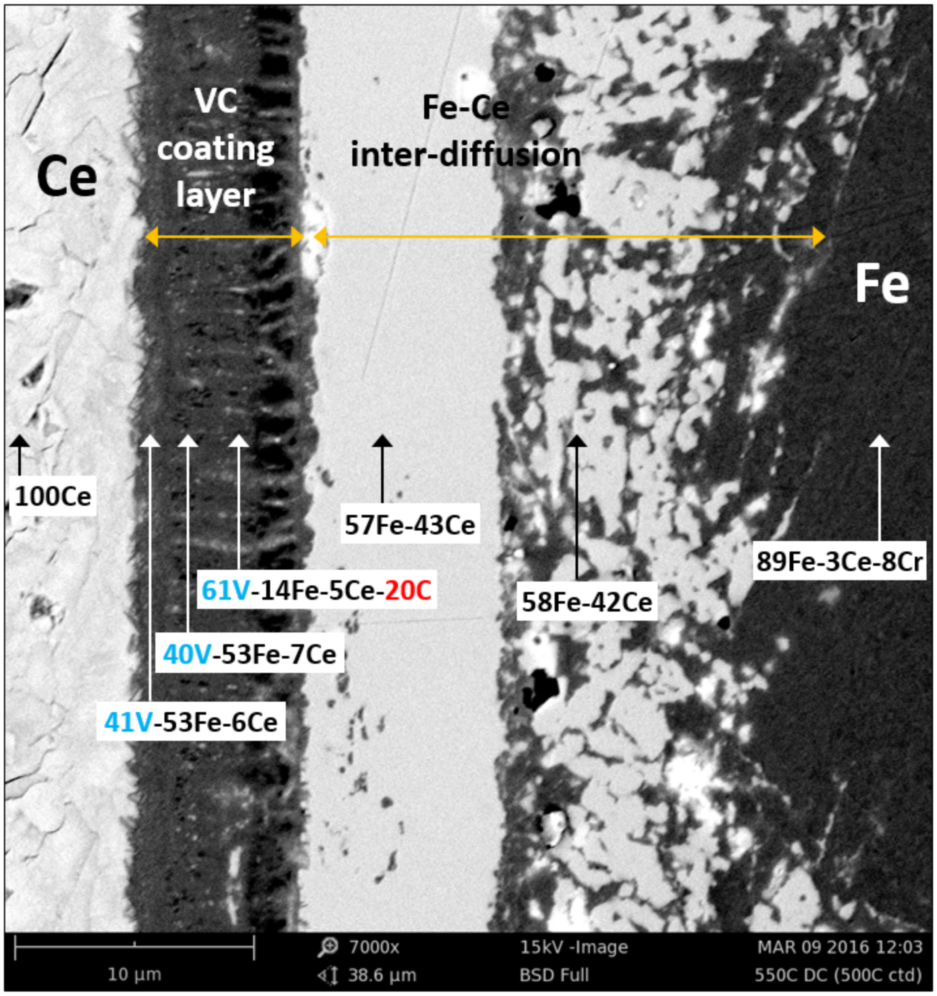

Figure 8-52. Enlarged BSE cross-sectional images of Ce/VC/T91 diffusion couple specimen. Each arrow indicates the compositional spot analysis at different spots.

Figure 8-53 shows the BSE top view image after ion-milling treatment. The depth of the ion-milled region was 4 μm from the surface, indicating that there was probably little effect of mechanical polishing on the sample surface. The result shows that a debris-like particles were still observable underneath the surface of the T91 substrate. In addition, it was quite comparable in composition with Figure 8-52 that debris-like particles also contain Ce as well as Fe. Therefore, it is confirmed that the debris-like particles were fabricated as a result of the Ce diffusion toward T91 substrate.

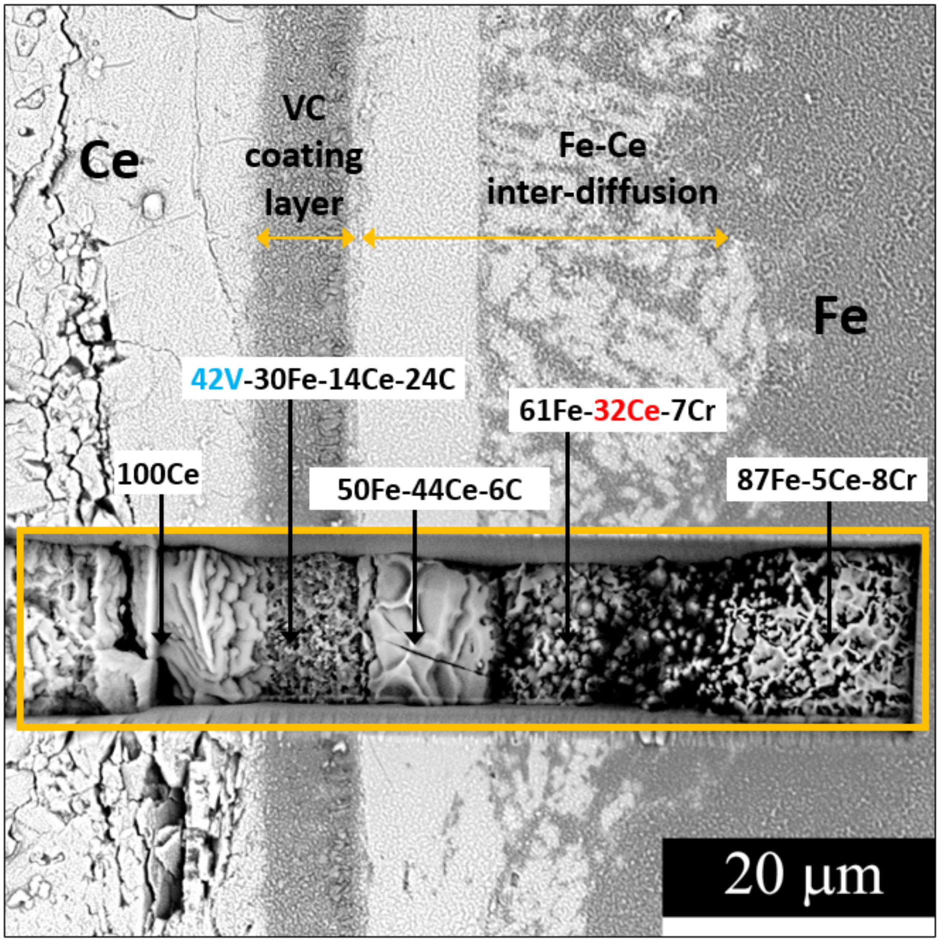

Figure 8-53. SEM micrograph after surface mill trench treatment by using a FIB. Yellow box indicates ion-milled region, which is approximately 4 µm below the surface.

From the previous diffusion couple experiments, it is thought that the thickness of the coating as well as the ration between V and C are important factor to minimize the inter-diffusion. Therefore, a coating sample with approximately 8 µm thick and the 1:1 ratio between V and C was used for the diffusion couple test. Figure 8-54 shows BSE micrograph of cross-sectional image of samples after a diffusion couple experiment at 550°C for 50 h. The average lengths of the inter-diffusion zone between T91 and Ce before and after the coating process were 45 µm and 5 µm, respectively. This indicates 89 % reduction in the inter-diffusion zone between the Fe and Ce sheets.

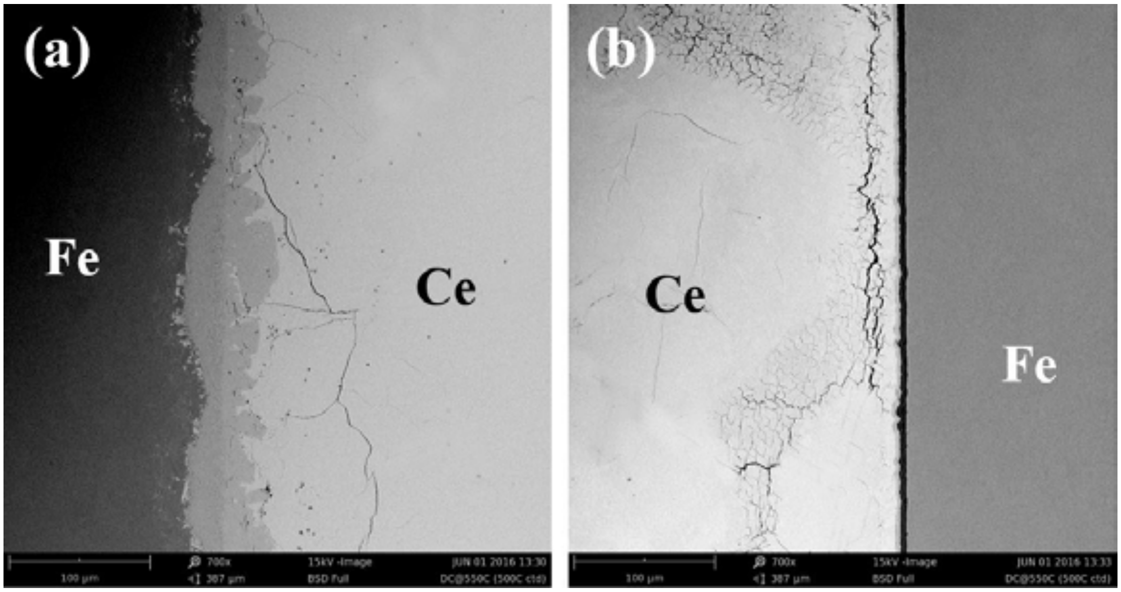

Figure 8-54. BSE micrograph of cross-sectional images after diffusion couple experiment at 550 ^{o}C for 50 h. (a) T91/Ce and (b) Ce/VC/T91. The coating was deposited at 500 ^{o}C.

Figure 8-55 shows enlarged BSE cross-sectional images (×10000) of Ce/VC/T91 specimen with spot analyses on each spot. First, Ce diffusion occurred through the vanadium carbide coating and T91 substrate. First, VC coating which consists of 3-layer prohibited the inter-diffusion between Ce and Fe. However, inter-diffusion occurred obviously at the layer near Ce, while second and third layers were intact relatively. In addition, the SEM cross-section images in Figure 8-56 show that there are various inter-diffusion behavior at different regions. While the coating layer was intact in Figure 8-56a, the coating was detached from the T91 steel probably due to the weak bonding between the coating and the T91 substrate. In addition, the coating at another region was split up after the diffusion couple test. Therefore, it is thought that none-uniform coating layer (e.g. multiple layers) has bad impact on inter-diffusion between the fuel and the cladding, since the interface at the boundary may act as cracking initiation and/or thermal concentration sites.

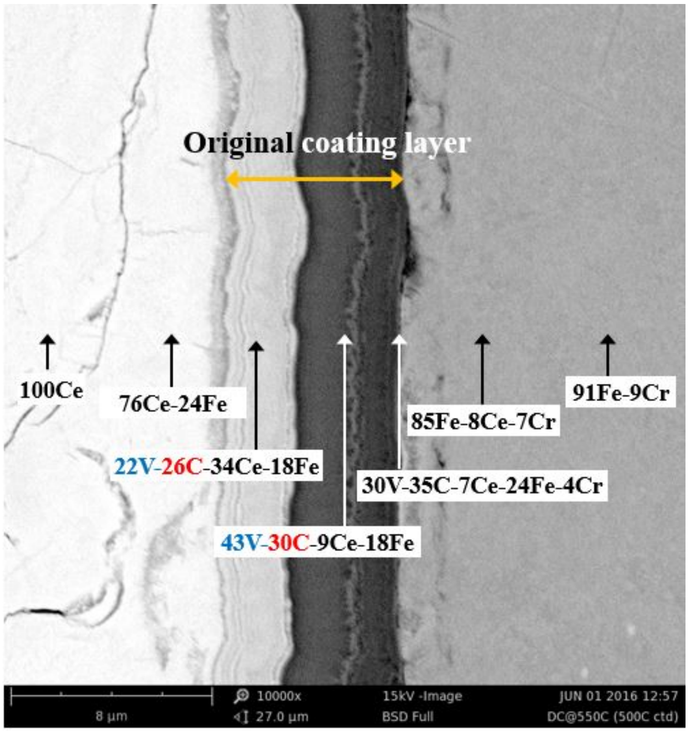

Figure 8-55. Enlarged BSE cross-sectional images of Ce/VC/T91 diffusion couple specimen. Each arrow indicates the compositional spot analysis at different spots.

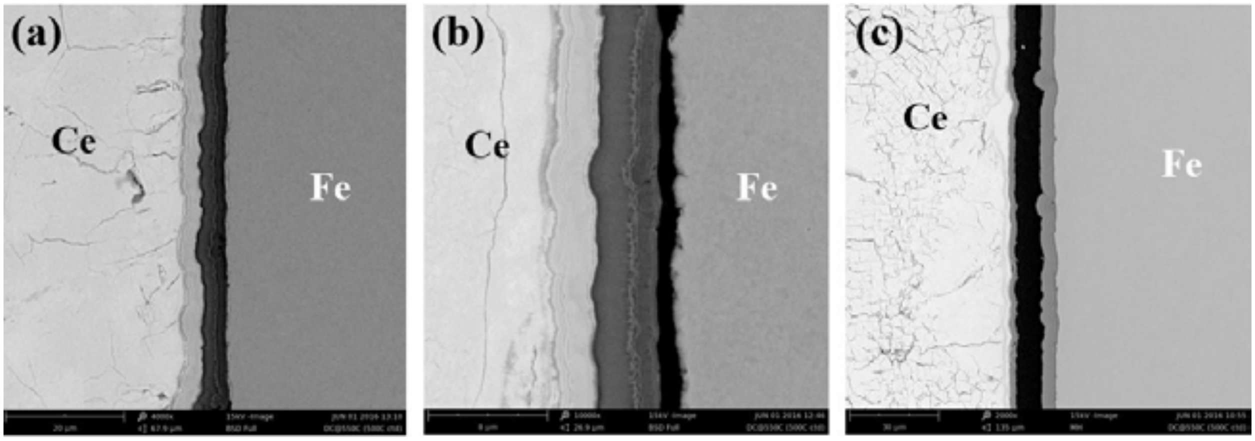

Figure 8-56. Diffusion couple results of Ce/VC/Fe coatings taken at different regions. (a) The coating layer was intact. (b) The coating was detached from the T91 substrate. (c) The coating was split up after the test.

Another diffusion couple test with the specimen which has approximately 6 µm thick uniform coating was performed (Figure 8-57). The average lengths of the inter-diffusion zone between T91 and Ce were 85 µm and 3 µm, respectively. This indicates 96 % reduction in the inter-diffusion zone between the T91 steel and Ce. In addition, the coating layer was intact after the test and there was no detachment between the coating and the T91 substrate (Figure 8-58). Furthermore, no Ce and Fe atoms diffused toward each side, since the coating layer blocked the diffusion of Ce as well as Fe atoms effectively.

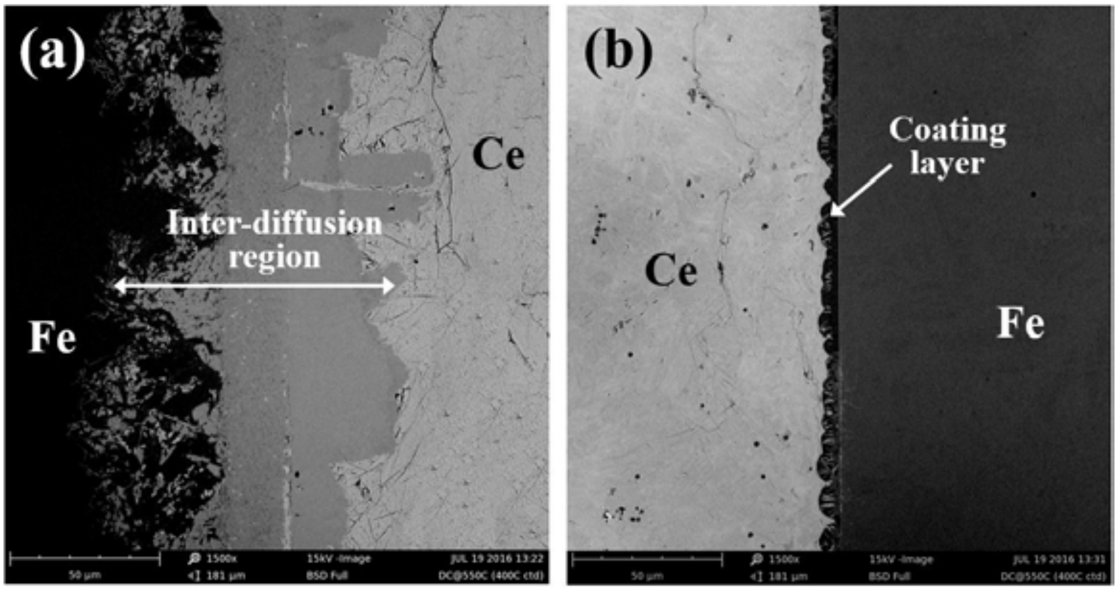

Figure 8-57. BSE micrograph of cross-section images after diffusion couple experiment at 550 ^{o}C for 50 h. (a) T91/Ce and (b) Ce/VC/T91. The coating was deposited at 400 ^{o}C.

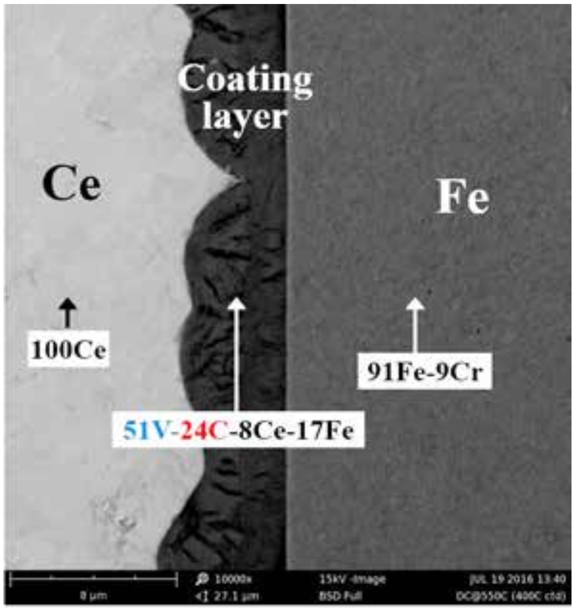

Figure 8-58. Enlarged BSE cross-section image of Ce/VC/T91 diffusion couple specimen. Each arrow indicates the compositional spot analysis at different spots.

Figure 8-59 shows enlarged BSE cross-section images of Ce/VC/T91 diffusion couple specimen taken at different area of the specimen. The coating prohibited the inter-diffusion between Ce and T91 substrate effectively at most area (Figure 8-59a and b), while small amount of Ce atoms diffused toward the coating and T91. At one spot, Ce atoms diffused through the coating which has thinner coating depth, and racking occurred afterward.

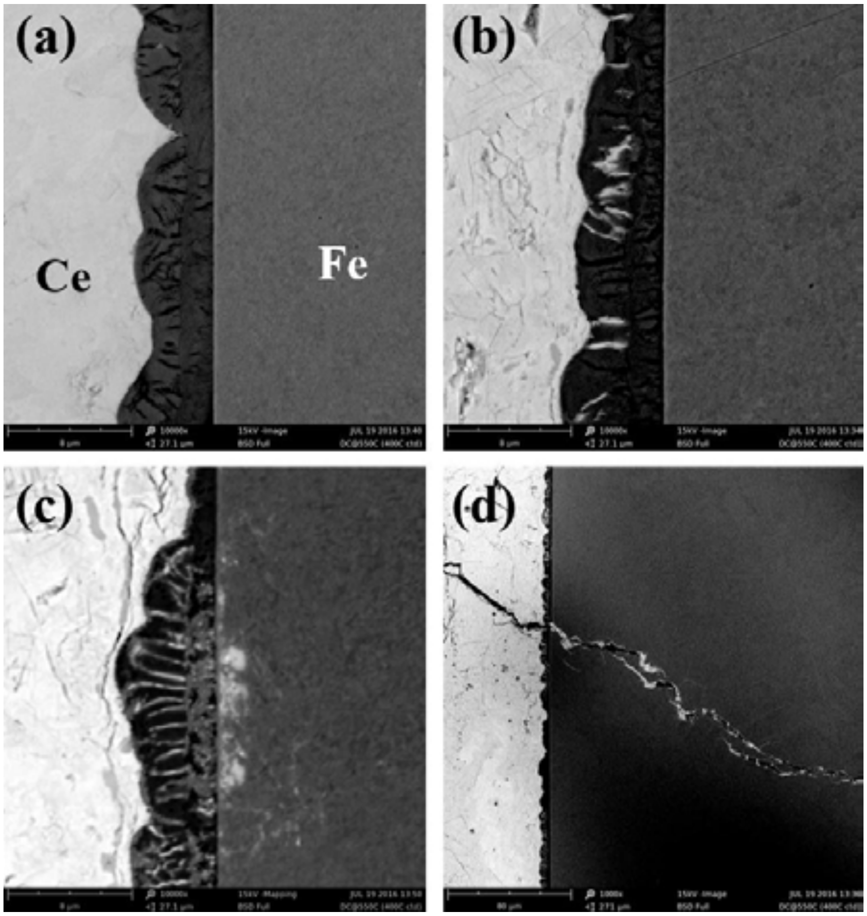

Figure 8-59. Enlarged BSE cross-section images of Ce/VC/T91 diffusion couple specimen. (a and b) The coating inhibited the inter-diffusion between Ce and T91 steel. (c) Small amount of Ce diffused toward the coating and T91. (d) Ce atoms diffused through the coating which has thinner coating depth. Cracking occurred afterward.

Figure 8-60 shows the BSE micrograph of cross-sectional image of samples after a diffusion couple experiment at 550 °C for 50 h. An annealing temperature of 550 ^{o}C was adopted based on the normal operating temperature at which the fuel/cladding interface could be exposed. The average lengths of the inter-diffusion zone between T91 and Ce before the coating process were approximately 40 μm (Figure 8-60a). However, after the deposition of the coating on the cladding material, there was a decrease in inter-diffusion (figure 8-60b). However, it is not enough to mitigate FCCI since it is clearly seen that Fe atoms diffused toward Ce sheet, while Ce atoms was not detected in the Fe substrate. This indicates that 5 μm thick coating was effective to inhibit Ce diffusion toward Fe, but still need further improvement to inhibit Fe diffusion toward Ce.

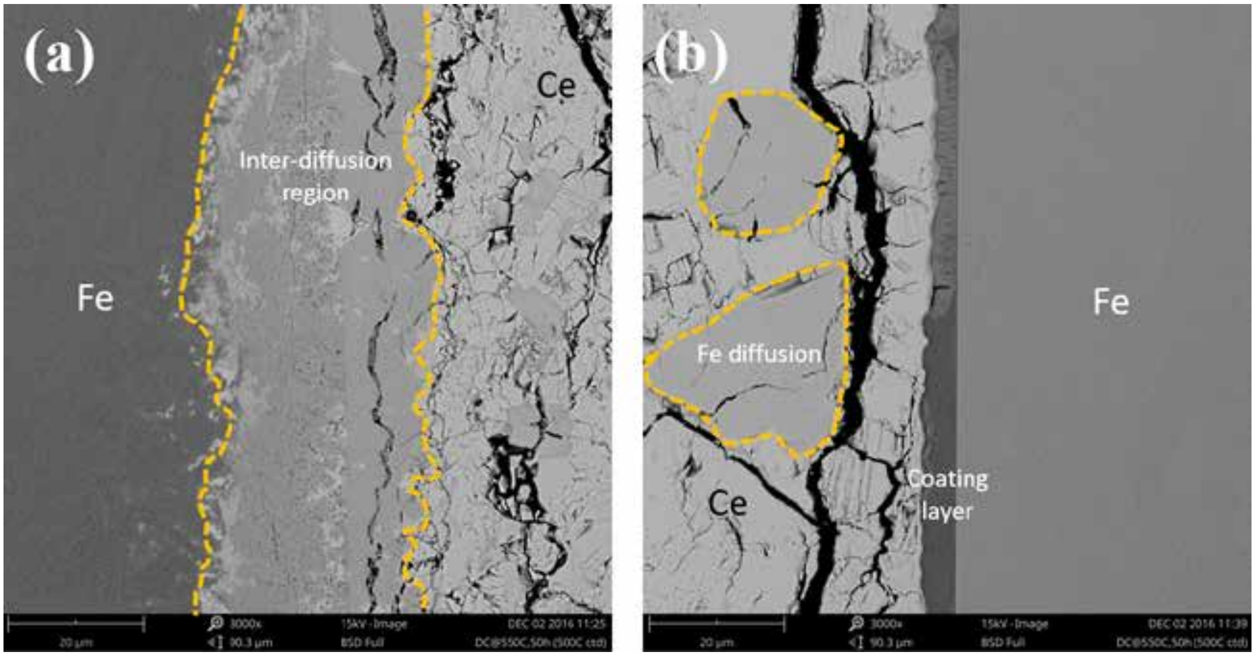

Figure 8-60. BSE micrograph of cross-sectional images of samples after diffusion couple experiment at 550 °C for 50 h. (a) T91/Ce and (b) T91/VC/Ce. The coating was deposited at 500 °C.

Figure 8-61 shows the BSE micrograph of cross-sectional image of samples after a diffusion couple experiment at 550 °C for 50 h. An annealing temperature of 550 °C was adopted based on the normal operating temperature at which the fuel/cladding interface could be exposed. The average lengths of the inter-diffusion zone between T91 and Ce before the coating process were approximately 50 μm (Figure 8-61a). Especially, Extensive Fe atoms were diffused toward Ce area. However, after the deposition of the coating on the cladding material, there was a decrease in inter-diffusion (figure 8-61b). However, it is not enough to mitigate FCCI since it is clearly seen that Fe atoms diffused toward Ce sheet, while Ce atoms was not detected in the Fe substrate (yellow dashed line in Figure 8-62). This indicates that 8 μm thick coating was effective to inhibit Ce diffusion toward Fe, but still need further improvement to inhibit Fe diffusion toward Ce.

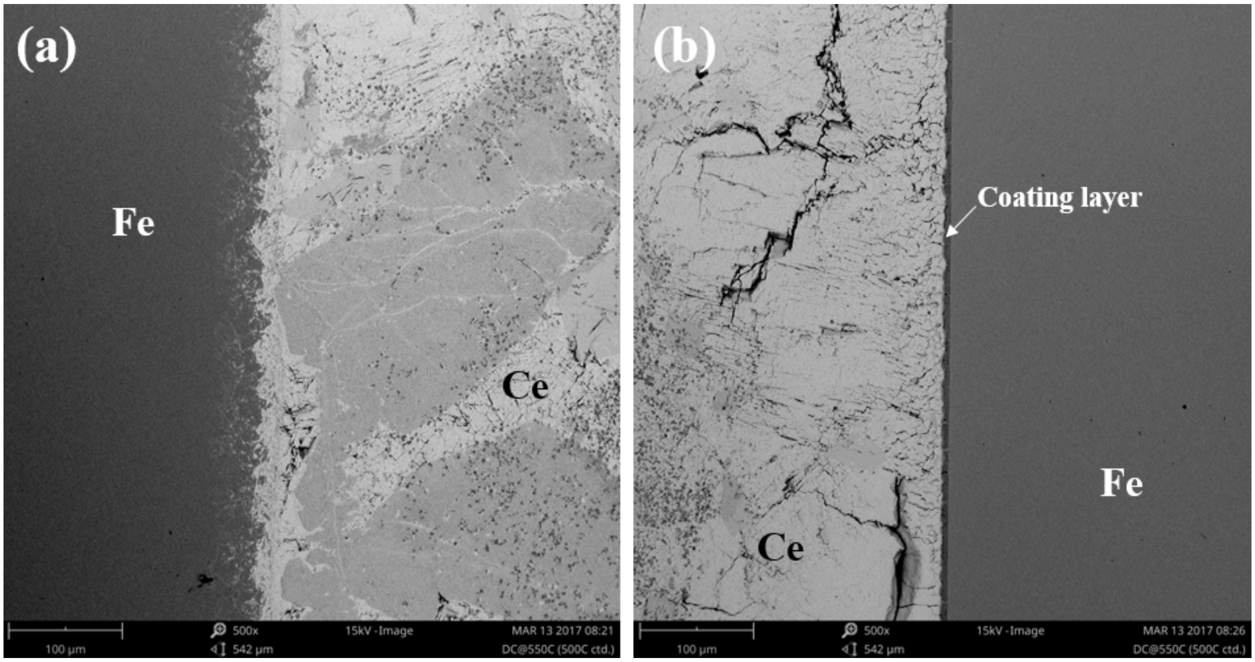

Figure 8-61. BSE micrograph of cross-sectional images of samples after diffusion couple experiment at 550 °C for 50 h. (a) T91/Ce and (b) T91/VC/Ce. The coating was deposited at 500 °C.

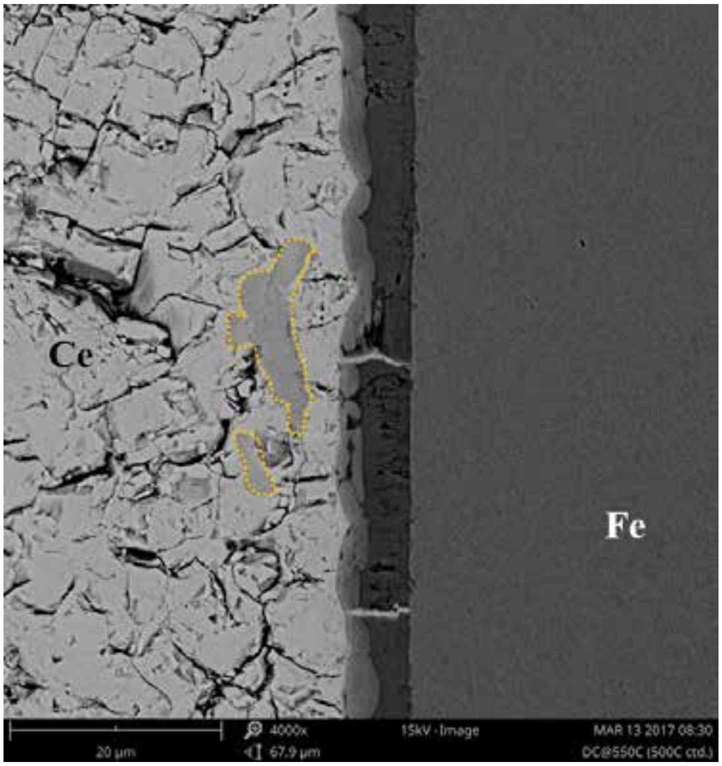

Figure 8-62. Enlarged BSE micrograph of cross-sectional images of T91/VC/Ce pack.

8.2.2. Diffusion Couple Studies at Aggresive Operating Temperature of SFR

Figure 8-63 shows diffusion couple test result of coated (Ce/coating/HT9) and uncoated (Ce/HT9) specimens annealed at 690 °C for 100 h. The width of inter-diffusion zone in the sample coated at 500 °C was approximately 35 μm (Figure 8-63a) and it mainly consists of Ce and Fe, while uncoated specimen has the inter-diffusion width of 160 μm (Figure 8-63b). It can be clearly identified that Ce actively diffuses into HT9 steel in uncoated specimen and the eutectic-melted structure on the Ce side was also observed due to higher annealing temperature. However, the diffusion couple result with the sample coated at 500 °C shows that the interaction zone decreased significantly. In the future, diffusion couple test annealed at temperature lower than eutectic temperature of Ce, which is 592 °C, will be also performed in order to validate the functionality of the coating as a FCCI barrier under normal operating condition of the SFR.

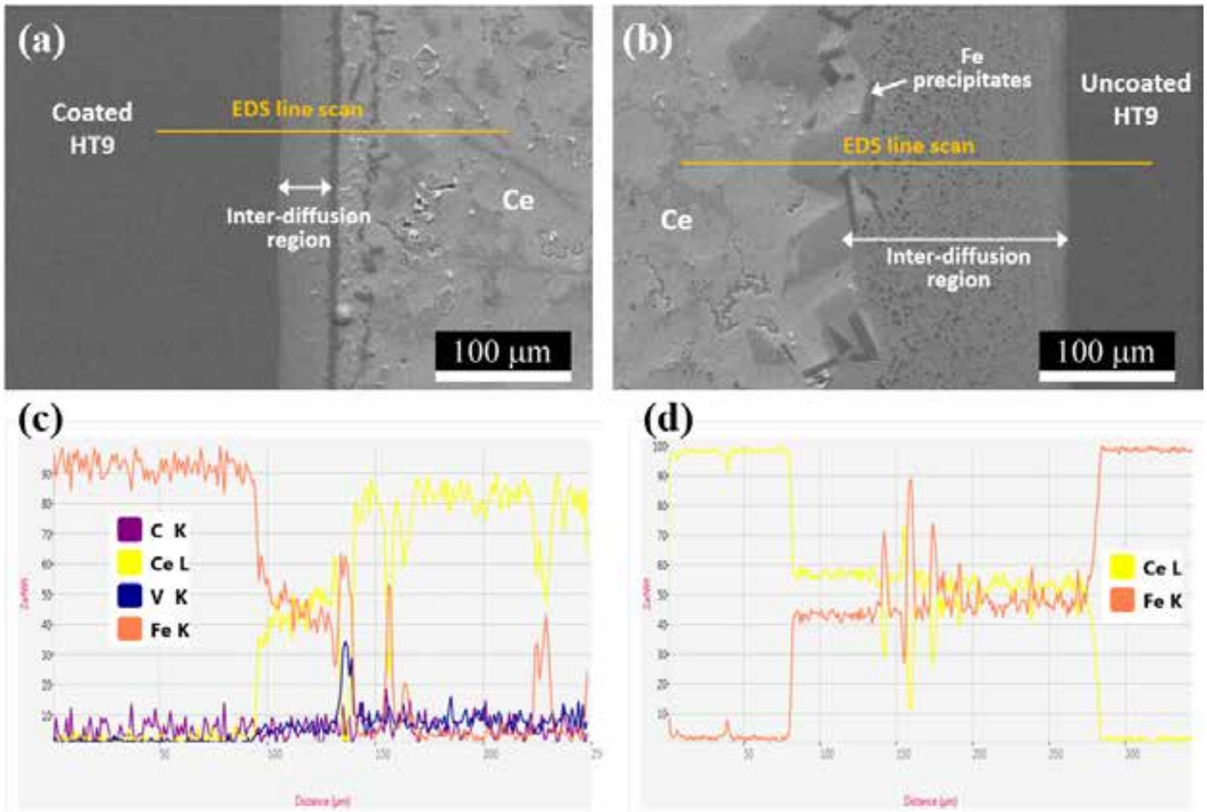

Figure 8-63. SEM cross sectional images and EDS line scan profiles of diffusion couple experiments with (a and c) coated and (b and d) uncoated specimens annealed at 690 °C for 100 h.

9. Atomistic modeling

A. *Energetics and ground state properties of ordered V_2C structures*

As a first step in determining the general diffusion behavior of extrinsic defects in V_2C, we studied self-diffusion within the material's ordered phases. According to X-ray diffraction studies of nearly stoichiometric V_2C at low temperatures [28-30], there are two distinct ordered phases, known as α and β'. The β' phase (space group $P\bar{3}1m$) has vanadium atoms arranged on a hexagonal lattice with the carbon atoms preferentially occupying half of the octahedral interstitial sites. This is in contrast to the high-temperature disordered β phase of V_2C in which the site occupation is random. At around 800°C, V_2C undergoes a hexagonal-orthorhombic transformation to the α phase (space group *Pbcn*). The transformation is characterized by a small distortion ~1.1% of the vanadium sublattice and a reordering of the occupied octahedral sites [28]. Ignoring the small distortion of the vanadium sublattice, the α and β' phases differ only in the arrangement of carbon atoms within the carbon sublattice.

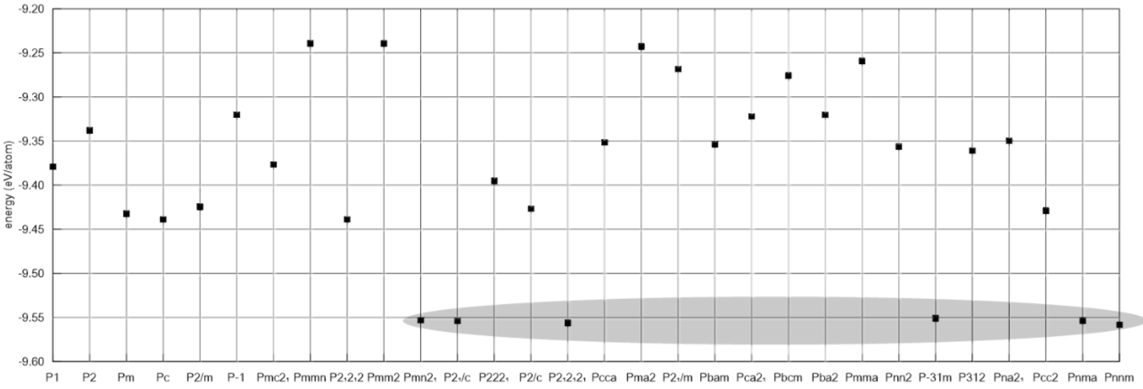

Figure 9-1. Cohesive energies of all symmetry inequivalent configurations of carbon atoms in V_2C for a 36-atom cell calculated using density functional theory.

To see how the specific carbon ordering influences the energy of a given V_2C structure, we looked at all possible configurations of occupied octahedral interstitial sites within a 36-atom cell. Once symmetry equivalent structures were eliminated, we then relaxed the remaining structures to their ground state using density functional theory (DFT). The ground state energies of these structures along with their space group designation are shown in Fig. 9-1. Out of the tens of different structures, six stood out as having significantly lower energy (~0.1 eV/atom) than the remaining structures. The relative energies of these six structures along with the structure corresponding to the α phase, whose symmetry is incommensurate with the specific 36-atom cell, are plotted in Fig. 9-2. The figure shows that the energy difference between these seven structures is small ~7.3 meV. Interestingly, the figure also shows that the experimentally determined ground state structure of V_2C, namely the α phase, does not correspond to the lowest energy structure in our DFT calculations. Instead, the lowest energy structure belongs to the space group *Pnnm*. This conclusion is independent of the DFT functional, LDA vs. GGA-PBE, used in the calculation.

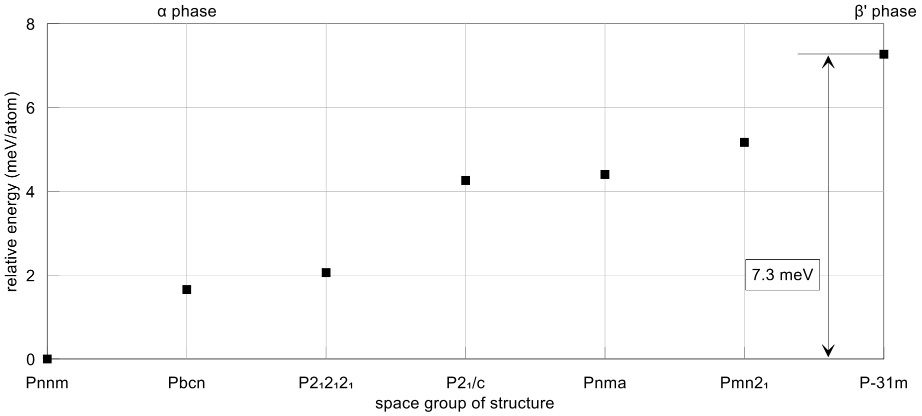

Figure 9-2. Relative energies of the six lowest-energy structures from Fig. 1 along with the structure belonging to the α phase (space group *Pbcn*) which is not commensurate with lattice used to generate the other structures.

The relaxed lattice parameters and cohesive energies for the lowest energy structure, shown in Fig. 9-2, and the α and β*'* phases of V_2C are given in Table 9-1. Cohesive energies calculated using both GGA-PBE and LDA functionals are provided to show that the energy ranking of the structures is independent of the specific functional used in the calculation. However, the lattice constants calculated using the GGA-PBE functional are in better agreement with experiment and therefore all calculations for the remainder of this work use this functional. To determine if the specific ordering of carbon atoms influences the self-diffusion behavior of V_2C, we have included the lowest-energy structure (space group *Pnnm*) in addition to the α and β*'* phases in our calculations. Schematic drawings of the unit cells for each of the three structures are shown in Fig. 9-3. Note that the β*'* phase is the only one of the three structures for which the density of carbon atoms is not the same between neighboring close-packed planes.

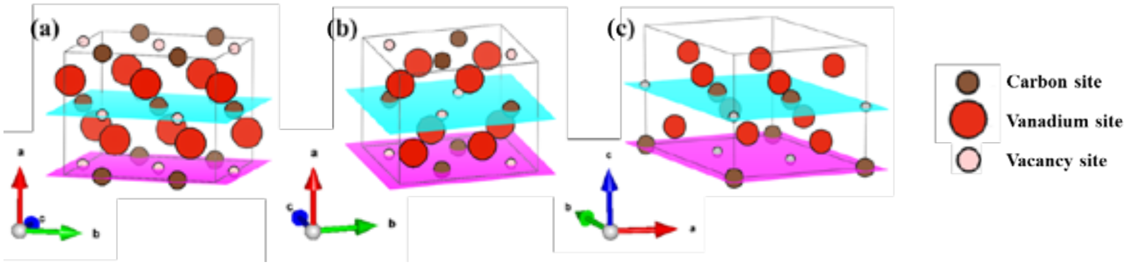

Figure 9-3. Unit cells of three ordered V_2C structures including (a) the low-energy orthorhombic structure belonging to space group *Pnnm*, (b) the α phase and (c) the β*'* phase. Lattice planes within the carbon sublattice are highlighted to show the different site occupations.

The calculated electronic band structure and density of states (DOS) for the α phase of V_2C is shown in Fig. 9-4. There is considerable band overlap at the Fermi energy which is in agreement with the experimental fact that early transition metal carbides are all good electrical conductors

[31]. The electronic band structure and DOS for the β′ phase and the other low-energy orthorhombic structure exhibit similar behavior.

Table 9-1. Lattice constants and cohesive energies for the α and β′ phases of V_2C and the low-energy structure belonging to space group *Pnnm* (see Fig.9-2). Theoretical results are obtained at zero temperature.

Space group (phase)	$Pnnm$	$Pbcn$ (α)							$P\bar{3}1m$ (β′)	
Lattice type	orthorhombic	orthorhombic							hexagonal	
Prototype	*anti* $CaCl_2$	ζ-Fe_2N							ε-Fe_2N	
a (Å)	4.534[*]	4.551[*]	4.55[a]	4.577[b]	4.57[c]	4.54[d]	4.495[e]	4.551[f]	5.008[*]	5.005[g]
b (Å)	5.733[*]	5.731[*]	5.745[a]	5.742[b]	5.742[c]	5.726[d]	5.628[e]	4.735[f]	-	-
c (Å)	5.037[*]	5.035[*]	5.03[a]	5.037[b]	5.026[c]	5.031[d]	4.929[e]	5.032[f]	4.535[*]	4.551[g]
E_0^{LDA} (eV/atom)	-9.5566	-9.5554							-9.5496	
E_0^{PBE} (eV/atom)	-10.5428	-10.5404							-10.5348	
E_{ZP} (meV/atom)	72.4	71.3							73.3	

[*] This work (VASP-PBE) [a] Expt. from Ref. [32] [b] Expt. from Ref. [28] [c] Expt. from Ref. [6] [d] VASP-PBE from Ref. [34] [e] CASTEP-PBE from Ref. [35] [f] CASTEP-PBE from Ref.[36] [g] Expt. from Ref.[37]

The zero-temperature elastic constants for the three different V_2C structures are given in Table 9-2. Values from previous theoretical works are given for the α phase. No other theoretical results could be found for the β′ phase. To the best of our knowledge, no experimental values exist for the single crystal elastic constants of either of the ordered V_2C phases. The bulk modulus K and shear modulus G for the aggregate V_2C crystal are estimated using the Voigt-Reuss-Hill approximation [32]. The Young′s modulus E and Poisson ratio ν can then be calculated from the well-known relations $\frac{1}{E}=\frac{1}{3G}+\frac{1}{9K}$ and $\nu=\frac{1}{2}\left(1-\frac{3G}{3K+G}\right)$. These moduli from our DFT calculations for all three V_2C structures as well as from other theoretical works for the α phase are given in Table 9-2.

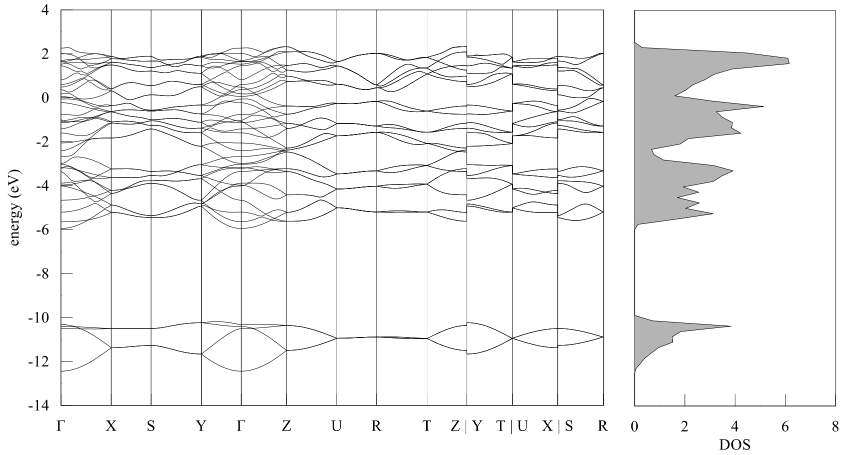

Figure 9-4. Electronic band structure and density of states (DOS) for the α phase of V_2C calculated using density functional theory. The Fermi energy is set to zero.

Figure 9-5 shows the theoretical phonon DOS for all three of the ordered V_2C structures calculated based on the relaxed lattice parameters in Table I. Each of the DOS decays to zero as the phonon frequency approaches zero indicating no unstable modes. Thus, the three ordered V_2C structures are mechanically stable. Zero point vibrational energy corrections to the total energy are calculated from [39]

$$E_{ZP} = \int_0^\infty g(\omega) \frac{\hbar\omega}{2} d\omega \qquad (1)$$

where $g(\omega)$ is the normalized phonon DOS. The zero point corrections to the cohesive energies for each of the three V_2C structures are given in Table I. Inclusion of the zero point energy reduces the energy difference between the two orthorhombic to ~1 meV, while the β*'* phase, which has the highest value of E_{ZP}, becomes even further removed energetically from the two orthorhombic structures.

TABLE 9-2. Zero-temperature elastic constants and elastic moduli for the three different ordered V_2C structures. Elastic moduli are estimated using the Voigt-Reuss-Hill approximation [32].

Space group (phase)	$Pnnm$	$Pbcn$ (α)				$P\bar{3}1m$ (β')
c_{11} (GPa)	434	414	393	452	400	419
c_{22} (GPa)	402	356	381	450	383	419
c_{33} (GPa)	437	392	410	493	414	426
c_{12} (GPa)	155	190	181	207	182	174
c_{13} (GPa)	143	118	122	146	120	149
c_{23} (GPa)	122	211	189	205	189	149
c_{44} (GPa)	157	112	107	122	110	123

c_{55} (GPa)	90	112	125	143	130	142
c_{66} (GPa)	80	78	131	161	135	142
$K\ (GPa)$	235	244	250	279	242	245
$G\ (GPa)$	118	100	118	140	121	133
$E\ (GPa)$	302	264	303	359	311	338
ν	0.285	0.320	0.290	0.290	0.286	0.270
Reference	This work VASP-PBE	This work VASP-PBE	Ref. [7] VASP-PBE	Ref. [8] CASTEP-PBE	Ref. [9] CASTEP-PBE	This work VASP-PBE

To see whether the carbon ordering affects the intrinsic defect and self-diffusion behavior in V_2C, we have included the low-energy orthorhombic structure predicted by DFT in addition to the α and β*'* phases in our calculations. The unit cells for these structures are shown in Fig. 9-3. Note that the β*'* phase is unique as the density of carbon atoms differs between neighboring planes along the close-packed direction.

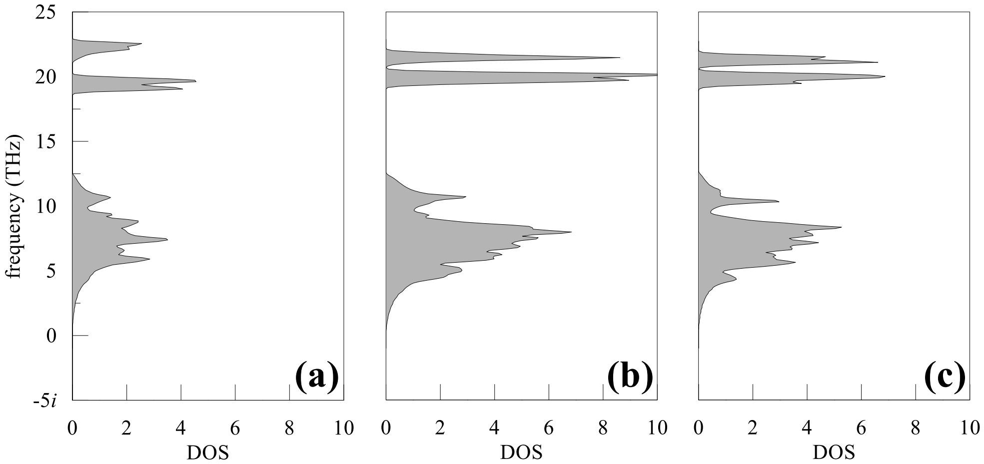

Figure 9-5. Theoretical phonon and density of states (DOS) for the (a) low-energy structure belonging to space group *Pnnm*, (b) the α phase of V_2C and (c) the β' phase of V_2C.

B. Vacancies in ordered structures of V_2C

As a first step towards investigating the self-diffusion behavior of V_2C, we calculated the formation energies of intrinsic defects most likely to aid in diffusion. Since the self-diffusion of each chemical species is thought to occur within their own respective sublattices, the only relevant defects to consider are vacancies. The formation energy at zero-temperature for a neutral defect X is given by [40-43]

$$\Delta E_f[X] = E[X] - E[\text{bulk}] + \sum_j n_j \mu_j \tag{2}$$

where $E[X]$ is the total energy of the cell with the defect, $E[\text{bulk}]$ is the total energy of the perfect cell, n_j is the number of atoms of chemical species j that are removed ($n_j > 0$) or added ($n_j < 0$) to the cell and μ_j is the energy of the atomic reservoir to which the atom is removed or added. In this work, μ_j is taken to be the cohesive energy per atom of either *bcc* vanadium or carbon graphite. Strictly speaking, the quantity measured in experiments is the formation enthalpy ΔH_f, but all calculations have been performed at zero pressure in which case $\Delta H_f = \Delta E_f$.

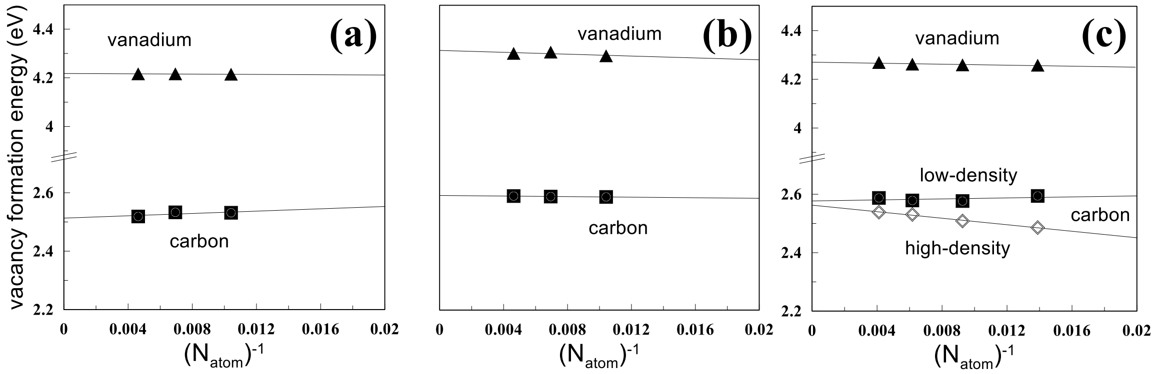

Figure 9-6. Calculated vacancy formation energies as a function of the number of atoms in the supercell for the (a) low-energy structure belonging to space group *Pnnm*, (b) the α phase of V_2C and (c) the β*'* phase of V_2C.

Figure 9-5 shows the convergence of the carbon and vanadium vacancy formation energies with respect to supercell size for the each of the three V_2C structures. The values listed in Table III were found by extrapolating linear fits of the calculated formation energies as $N^{-1} \to 0$. The similarity of the formation energies among the three structures indicates that the carbon arrangement has only a small effect on the overall interatomic bond strength. As the β*'* phase has two unique carbon sites, we denote the carbon atom lying in the high-density plane as C*'* and the carbon in the low-density plane as C. The vacancy formation energies for the two different carbon atoms, $\Delta E_f[v_C]$ and $\Delta E_f[v_{C'}]$, approach a common value as the supercell size increases, thus indicating a single unique carbon vacancy formation energy for large systems.

Table 9-3. Vacancy formation energies for the three different ordered V_2C structures calculated using density functional theory.

Space group (phase)	$Pnnm$	$Pbcn$ (α)	$P\bar{3}1m$ (β')
$\Delta E_f[v_C]$ (eV)	2.51	2.59	2.56
$\Delta E_f[v_{C'}]$ (eV)	-	-	2.56
$\Delta E_f[v_V]$ (eV)	4.22	4.31	4.27

C. Vacancy-assisted self-diffusion of vanadium in V_2C

Ignoring the small distortions in the two orthorhombic structures, the vanadium atoms in V_2C form an almost perfect *hcp* sublattice. It is assumed that vanadium self-diffusion occurs exclusively on the vanadium sublattice by a standard vacancy-assisted mechanism. As mentioned in the introduction, the former assumption is based on experimental evidence that the metal atom diffusivity in transition metal carbides in independent of carbon concentration. Following from this point, we further assume no net displacement of carbon atoms occurs as a result of vanadium atom migration. That is to say the carbon arrangements before and after vanadium migration are identical. Considering only the first nearest-neighbor shell, a vanadium may either migrate within its own basal plane (jump A) or into one of the two adjacent planes (jump B) as shown in Fig. 9-7(a). The in-plane $D_{\perp}$ and out-of-plane $D_{\parallel}$ self-diffusion coefficients for vanadium are given by

$$\begin{aligned} D_{\perp} &= \frac{1}{4} C_v \left(f_{Ax} \sum_i v_i^* \exp\left(-\frac{\Delta E_{A,i}^m}{kT}\right) d_{\perp,i}^2 + f_{Bx} \sum_j v_j^* \exp\left(-\frac{\Delta E_{B,j}^m}{kT}\right) d_{\perp,j}^2 \right) \\ D_{\parallel} &= \frac{1}{2} C_v f_{Bz} \sum_i v_i^* \exp\left(-\frac{\Delta E_{B,i}^m}{kT}\right) d_{\parallel,i}^2 \end{aligned} \tag{3}$$

where C_v is the concentration of thermal vacancies on the vanadium sublattice, v_i^* are the effective frequencies, $\Delta E_{A,i}^m$ and $\Delta E_{B,i}^m$ are the vacancy migration energies for jumps of type A and B, respectively, $d_{\perp,i}^2$ and $d_{\parallel,i}^2$ are the in-plane and out-of-plane squared displacements and the f's are the correlation factors. The subscripts i and j denote the index of the migrating atom. In the expression for $D_{\perp}$, the first sum is taken over the six nearest-neighbor vanadium atoms within the basal plane of the vacancy and the second sum is taken over the six nearest-neighbor vanadium atoms in the two adjacent planes. In the expression for $D_{\parallel}$, the sum is taken over only the six nearest-neighbor vanadium atoms in the two adjacent planes; jumps within the same basal plane do not contribute to $D_{\parallel}$.

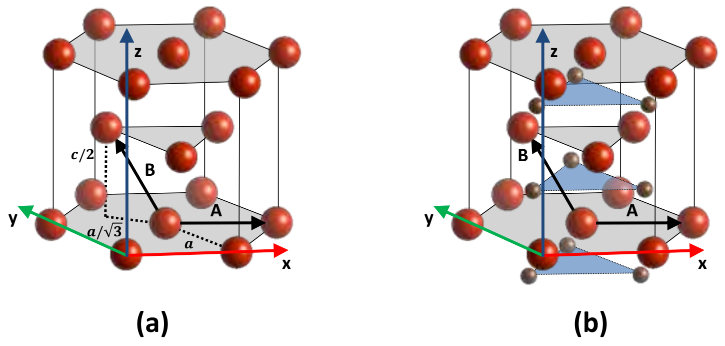

(a) **(b)**

Figure 9-7. In-plane (A) and out-of-plane (B) jumps for vanadium to a nearest-neighbor site within the vanadium sublattice (a) without octahedral sites shown and (b) with octahedral sites shown. Vanadium atoms are shown as large (red) spheres, while octahedral sites are shown as small (brown) spheres. In V_2C, only half of the octahedral sites are occupied by carbon.

The concentration of vacancies on the vanadium sublattice follows an Arrhenius dependence $C_v = \exp\left(\Delta S_f^{vib}/k\right)\exp\left(-\Delta E_f/kT\right)$, where ΔS_f^{vib} and ΔE_f are the vibrational entropy and energies of vacancy formation. The calculated ΔE_f values for a single vanadium vacancy have been given in Table III. The vibrational entropy of a harmonic solid composed of N atoms is given by [34]

$$S^{vib} = k\int_0^{\infty} g(\omega)\left\{\frac{\hbar\omega}{kT}\left[\exp\left(\frac{\hbar\omega}{kT}\right)-1\right]^{-1} - \ln\left[1-\exp\left(-\frac{\hbar\omega}{kT}\right)\right]\right\} \qquad (4)$$

where $g(\omega)$ is the phonon density of states, which is obtained by diagonalization of the dynamical matrix on a 15×15×15 mesh of phonon wave vectors. The expression for ΔS_f^{vib} is analogous to Eq. 2 for ΔE_f and requires calculating S^{vib} for three systems: a perfect V_2C supercell, the same supercell containing a single vanadium vacancy and a supercell of *bcc* vanadium. For the perfect and defect systems, the supercell sizes used in the dynamical matrix calculations are 2×2×4 (96 atoms) for the *Pnnm* structure, 2×2×2 (96 atoms) for the α phase and 2×2×2 (72 atoms) for the β*'* phase. For *bcc* vanadium, a 4×4×4 conventional supercell is used. Calculated values of ΔS_f^{vib} for the three structures are given in Table IV.

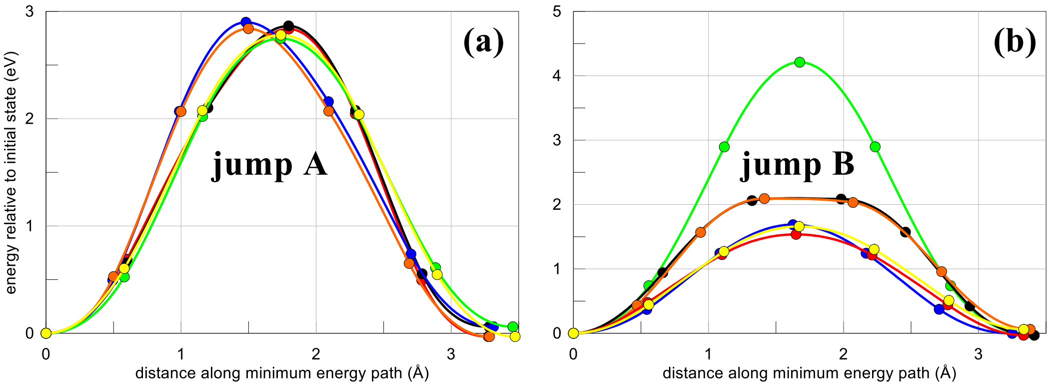

Figure 9-8. Theoretical minimum energy paths (MEPs) for vanadium vacancy migration for (a) in-plane (jump A) and (b) out-of-plane (jump B) migration for the β*'* phase calculated using the climbing-image nudged elastic band method. Different colors correspond to MEPs for different migrating vanadium atoms.

The migration energy is defined as $\Delta E^m = E^{TS} - E^{IS}$, where E^{TS} is the energy of the saddle point along the minimum energy path (MEP) between the two end states and E^{IS} is the energy of the initial state. For the vacancy mechanism considered here, the initial state corresponds to a supercell with a vanadium vacancy, while the final state corresponds to moving one of the 12 nearest-neighbor vanadium atoms to the vacancy site. CI-NEB calculations are performed on a set of interpolated image structures for each of the 12 initial and final state pairs. We find that the migration energies converge rapidly with respect to supercell size; migration energies for a 71-

atom supercell for the β' phase and 95-atom supercells for the two orthorhombic structures are converged to within 0.05 eV.

Carbon atoms at the octahedral sites, see Fig. 9-7(b), impact the local environments of the migrating vanadium atoms, which can result in large differences in the shape of the MEPs and corresponding migration energies for jumps of the same type. Table IV gives the values for ΔE_A^m and ΔE_B^m for the three V_2C structures considered in this work. For the β' phase, ΔE_A^m are found to vary by 0.15 eV, while ΔE_B^m is found to vary by as much as 2.65 eV. The other two orthorhombic structures show similar variation in ΔE_A^m, whereas the variation in ΔE_B^m for the structure belonging to space group *Pnnm* is ~1 eV more than either the β' phase or the α phase, see Table 9-4. This difference can be attributed to the differing arrangements of carbon atoms in the three V_2C structures. Three distinct groups of MEPs are observed for jump B as shown in Fig. 9-8(b). This is also true of the two orthorhombic structures whose MEPs are not shown.

Table 9-4. Formation entropies $\boldsymbol{\Delta S_f^{vib}}$, energies of migration $\boldsymbol{\Delta E_A^m}$ and $\boldsymbol{\Delta E_A^m}$ and effective frequencies $\boldsymbol{v}^*$ for the vacancy-assisted vanadium self-diffusion mechanism for the three different ordered V_2C structures calculated using density functional theory.

Space group (phase)	$Pnnm$	$Pbcn$ (α)	$P\bar{3}1m$ (β')
ΔS_f^{vib} (k)	4.15	5.40	5.16
ΔE_A^m (eV)	2.71	2.64	2.75
	2.71	2.64	2.81
	2.84	2.71	2.86
	2.84	2.72	2.87
	2.86	2.80	2.87
	2.86	2.82	2.90
ΔE_B^m (eV)	1.24	1.47	1.57
	2.09	1.98	1.66
	2.09	1.99	1.69
	2.10	2.00	2.10
	2.11	2.02	2.11
	4.83	4.03	4.21
v_A^* (THz)	9.0-10.4	8.1-10.6	7.7-11.3
v_B^* (THz)	5.6-13.2	5.5-11.2	5.3-11.5

The effective frequencies v^* for an N-atom system are calculated from [45-47]

$$v^* = \prod_{i=1}^{3N-3} \omega_i \Big/ \prod_{j=1}^{3N-4} \omega_j' \tag{5}$$

where the ω_i and ω_j' are the normal mode frequencies for the initial and transition states, respectively. The product over the transition state frequencies is reduced by one relative to the initial state due to the presence of an imaginary mode along the migration direction. We approximate the normal mode frequencies for the entire system by those of the migrating atom only. This is the Einstein (independent oscillator) approximation. Eq. 5 simplifies greatly as the migrating atom contributes only three normal modes to the initial state and two modes to the transition state; the third mode of the transition state is imaginary and does not enter into Eq. 5. The v^* are calculated for each of the 12 MEPs determined by the CI-NEB calculations. Again we use the supercell with the same dimensions as those used in the calculation of ΔS_f^{vib} and ΔE^m. The ranges of v^* for jumps A and B are given in Table 9-4.

Table9-5. Correlation factors for vacancy-assisted self-diffusion in an *hcp* lattice taken from Ref. [38] for a range of typical ratios for the jump frequencies $\boldsymbol{w_A/w_B}$ encountered for the V_2C system.

T (K^{-1})	w_A/w_B	f_{Ax}	f_{Bx} (f_{Bz})
1000	9.25E-04	0.9224	0.6466
1200	3.02E-03	0.9219	0.6470
1400	7.02E-03	0.9210	0.6479
1600	1.32E-02	0.9195	0.6492
1800	2.17E-02	0.9175	0.6511
2000	3.21E-02	0.9151	0.6534
2200	4.44E-02	0.9122	0.6561
2400	5.80E-02	0.9090	0.6592
2600	7.29E-02	0.9055	0.6625
2800	8.85E-02	0.9018	0.6660
3000	1.05E-01	0.8981	0.6697

The correlation factors f for vacancy-assisted diffusion in an *hcp* lattice have been calculated elsewhere [21] and are a function of the ratios of jump frequencies $w_A = v_A^* \exp(-\Delta E_A^m/kT)$ and $w_B = v_B^* \exp(-\Delta E_B^m/kT)$. Table VII gives the correlation factors and ratio of jump frequencies over a temperature range of 1000 to 2800 K, where the jump frequencies are representative of those calculated for V self-diffusion in V_2C in that temperature range. The difference in f_{Bx} and f_{Bz} is negligible for the ranges of jump frequencies considered. The self-diffusion coefficients $D_\perp$

and $D_{\parallel}$ in Eq. 3 are calculated using the values for $\Delta E_f[v_V]$, ΔS_f^{vib}, ΔE_A^m, ΔE_B^m, v_A^* and v_B^* listed in Tables 9-3, 4 and 5. The average values of w_A/w_B are used to calculate the correlation factors. The resultant $D_{\perp}$ and $D_{\parallel}$ are then fit to an Arrhenius expression of the form $D = D_0 \exp(-Q/kT)$. The fitted activation energies Q and diffusion prefactors D_0 for $D_{\perp}$ and $D_{\parallel}$ are given in Table VI for each of the three ordered V_2C structures. Experimental values for Q and D_0 for metal atom diffusion in cubic NbC_x and TiC_x are also given.

Table 9-6. Activation energies $\boldsymbol{Q}$ and diffusion prefactors $\boldsymbol{D_0}$ for vacancy-assisted vanadium self-diffusion for the three different ordered V_2C structures calculated using density functional theory. Experimental values for Nb in cubic NbC_x and Ti in cubic TiC_x are given for comparison.

	This work ($Pnnm$)	This work (α phase)	This work (β' phase)	Nb in NbC_x (expt. [22])	Ti in TiC_x (expt. [23])
$Q_{\perp}$ (kcal/mol)	126.3	134.7	135.9	140.0±2.4	176.4±3.6
$Q_{\parallel}$ (kcal/mol)	126.1	134.2	136.2		
$D_{0,\perp}$ (cm^2/s)	0.04	0.20	0.33	$4.54^{+2.85}_{-1.75}$	$4.36^{+5.02}_{-2.34}$
$D_{0,\parallel}$ (cm^2/s)	0.17	0.73	1.17		

D. Interstitial self-diffusion of carbon in V_2C

In each of the V_2C structures, carbon atoms fill half of the available octahedral interstitial sites, while the other half are vacant. Because the concentration of such structural vacancies dwarfs the concentration of thermal vacancies, we expect carbon self-diffusion to occur through migration of carbon atoms to nearest-neighbor vacant octahedral sites. Altogether the octahedral interstitial sites form a simple hexagonal lattice (ignoring the small distortions for the two orthorhombic structures). Octahedral sites share faces with neighboring octahedral sites in adjacent basal planes, but share edges with neighboring octahedral sites within the same basal plane, see Fig. 9-9(a). Tetrahedral sites share faces with neighboring octahedral sites within the same basal plane, see Fig. 9-9(b).

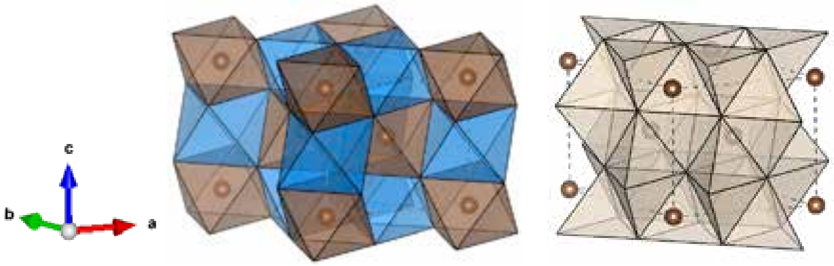

(a) (b)

Figure 9-9. Coordination polyhedra for the (a) octahedral and (b) tetrahedral interstitial sites for the β′ phase of V_2C. Carbon atoms occupy octahedral sites surrounded by brown octahedra, while blue octahedra surround empty sites. All tetrahedral sites are vacant.

It has been argued that in close-packed structures migrating atoms will pass through faces of connecting polyhedra rather than edges due to the larger effective "window" provided by the faces [51,52]. An octahedral-tetrahedral-octahedral (O-T-O) mechanism was proposed [53-54] in which the migrating atom temporarily occupies a nearest-neighbor tetrahedral site before advancing to a vacant octahedral site within the same basal plane. However, no direct evidence of the actual carbon self-diffusion mechanism has been given for V_2C. Therefore, we consider a direct octahedral-octahedral (O-O) mechanism in addition to the O-T-O mechanism in our DFT calculations as it is not clear which is energetically favorable. Between basal planes the octahedral sites share faces and so a direct O-O jump mechanism is almost certain. In total, we consider two O-O and one O-T-O jumps: an O-O jump within the same basal plane (jump A), an O-O jump from one basal plane to another (jump B) and an O-T-O jump in which the two octahedral sites share the same basal plane (jump C). These jumps are shown in Fig. 9-10 for the simple hexagonal lattice of octahedral sites found in V_2C.

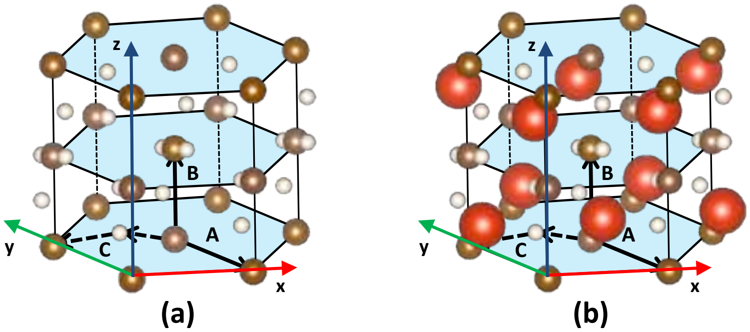

Figure 9-10. Octahedral-octahedral, labeled A and B, and octahedral-tetrahedral-octahedral, labeled C, site jumps considered as likely migration paths for carbon self-diffusion in V_2C (a) without and (b) with the vanadium atoms shown. Only half of the octahedral sites are occupied by carbon atoms, while all tetrahedral sites are vacant. Vanadium atoms are shown as large (red) spheres, octahedral sites as medium-sized (brown) spheres and tetrahedral sites as small (white) spheres.

Based on our DFT calculations, the energy cost of a carbon occupying a tetrahedral site is greater (by ~2 eV) than the migration energy for the in-plane O-O mechanism (jump A). This is true for all three of the ordered V_2C structures used in this work. Therefore, the contribution of the O-T-O mechanism (jump C) to the self-diffusion coefficient of carbon is negligible and in-plane self-diffusion of carbon will occur via the O-O mechanism (jump A). In light of this, the in-plane $D_\perp$ and out-of-plane $D_\parallel$ self-diffusion coefficients for interstitial diffusion of carbon are given by

$$D_{\perp} = \frac{1}{4} C_{v,\perp} f_x \sum_i v_i^* \exp\left(-\frac{\Delta E_{A,i}^m}{kT}\right) d_{\perp,i}^2$$

$$D_{\parallel} = \frac{1}{2} C_{v,\parallel} f_z \sum_i v_i^* \exp\left(-\frac{\Delta E_{B,i}^m}{kT}\right) d_{\parallel,i}^2 \tag{6}$$

where $C_{v,\perp}$ and $C_{v,\parallel}$ are the fractions of vacant octahedral sites surrounding the migrating carbon atom within the same basal plane and in the adjacent basal planes, respectively, v_i^* are the effective frequencies, $\Delta E_{A,i}^m$ and $\Delta E_{B,i}^m$ are the migration energies for jumps of type A and B, respectively and the f's are the correlation factors. In the expression for $D_{\perp}$, the sum is taken over all possible jumps of type A. Similarly, the sum in the expression for $D_{\parallel}$ is taken over jumps of type B. Jumps of type B do not contribute to $D_{\perp}$ while jumps of type A do not contribute to $D_{\parallel}$. For the β' phase, $C_{v,\perp} = 1$ for the low-density carbon plane and $C_{v,\perp} = 1/2$ for the high-density plane. $C_{v,\perp} = 2/3$ for the two orthorhombic structures and $C_{v,\parallel} = 1$ for all three structures.

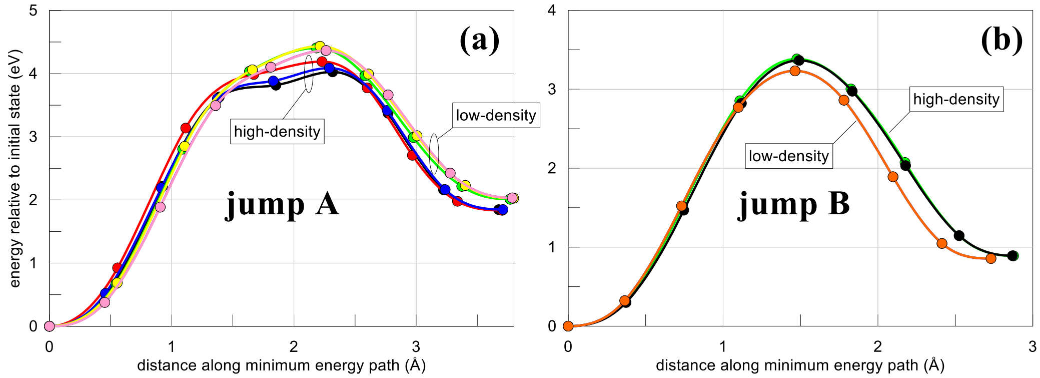

Figure 9-11. Theoretical minimum energy transition paths for carbon interstitial migration (a) in-plane (jump A) and (b) out-of-plane (jump B) for the β' phase calculated using the climbing-image nudged elastic band method. Different colors correspond to MEPs for different migrating carbon atoms.

For the β' phase, there are six possible A jumps for the low-density plane of carbon atoms and three possible A jumps for the high-density plane. There are two possible B jumps for both the low- and high-density planes. The converged MEPs for these jumps are shown in Fig. 9-11. As can be seen from the figure, the MEPs for both the low- and high-density planes are similar for each jump type. As in the case of the CI-NEB calculations for vanadium migration, the saddle points for carbon migration converge rapidly with respect to supercell size. Migration energies for a 72-atom supercell for the β' phase and 96-atom supercells for the two orthorhombic structures are converged to within 0.05 eV. The migration energies ΔE_A^m and ΔE_B^m and ranges for the effective frequencies v_A^* and v_B^* are given in Table VII for all three ordered V_2C structures considered in this work. The v^* for carbon self-diffusion are calculated in the same manner and using the same supercell sizes used in the calculations of the v^* for vanadium self-diffusion. The tetrahedral site energies $\Delta E_{\square}^{m}$ are also given in Table 9-7 for comparison, though they are not used in the calculation of $D_{\perp}$.

Table 9-7. Migration energies $\boldsymbol{\Delta E_A^m}$ and $\boldsymbol{\Delta E_B^m}$ and effective frequencies $\boldsymbol{v}^*$ for carbon self-diffusion for each of the three ordered V_2C structures calculated using density functional theory. The tetrahedral site energy for the O-T-O mechanism $\boldsymbol{\Delta E_C^m}$ is given for comparison.

Space group (phase)	$Pnnm$	$Pbcn$ (α)	$P\bar{3}1m$ (β')
ΔE_A^m (eV)	4.06	4.12	4.37 (low density) 4.03 (high density)
	4.06	4.16	4.37 (low density) 4.09 (high density)
	4.09	4.20	4.41 (low density) 4.19 (high density)
	4.09	4.38	4.41 (low density)
			4.43 (low density)
			4.43 (low density)
ΔE_B^m (eV)	3.56	3.48	3.23 (low density) 3.37 (high density)
	3.56	3.51	3.23 (low density) 3.38 (high density)
ΔE_C^m (eV)	6.06	5.78	5.83 (low density) 6.31 (high density)
v_A^* (THz)	19.4-20.0	21.1-26.0	23.3-27.0 (low density) 19.9-20.9 (high density)
v_B^* (THz)	17.9-18.3	21.3-22.0	21.0-21.7 (low density) 20.5-21.1 (high density)

The correlation factors f for interstitial diffusion in concentrated interstitial alloys, like carbides, nitrides and hydrides, have not been determined and it is out of this scope of this work to do so. The vanadium and carbon atoms do not share a common sublattice: one is *hcp* while the other is simple hexagonal. This is in contrast to *fcc* interstitial compounds, where the octahedral interstitial sites also form an *fcc* lattice. In that case, the correlation factor for interstitial self-diffusion will lie between that for pure vacancy-assisted diffusion and unity. Because there is not a simple one-to-one correspondence for *hcp*, we instead set the correlation factors to unity. The self-diffusion coefficients given in Eq. 7 are calculated using the results in Table IX and then fit to an Arrhenius expression $D = D_0 \exp(-Q/kT)$. The activation energies Q and diffusion prefactors D_0 from these fits are given in Table 9-8.

Table 9-8. Activation energies $\boldsymbol{Q}$ and diffusion prefactors $\boldsymbol{D_0}$ for carbon self-diffusion for each of the three ordered V_2C structures calculated using density functional theory. Experimental values for C in disordered cubic V_6C_5 and C in $NbC_{0.868}$ are given for comparison.

	This work ($Pnnm$)	This work (α phase)	This work (β′ phase)	C in V_6C_5 (expt. [26])	C in $NbC_{0.868}$ (expt. [27])
$Q_\perp$ (kJ/mol)	93.8	96.2	101.3 (low density) 93.9 (high density)	85.0±0.5	100.4±2.2
$Q_\parallel$ (kJ/mol)	82.1	80.5	74.5 (low density) 77.8 (high density)		
$D_{0,\perp}$ $(\mathrm{cm}^2/\mathrm{s})$	1.6E-02	1.7E-02	3.0E-02 (low density) 1.2E-02 (high density)	$2.65^{+0.35}_{-0.31}$	$2.59^{+1.82}_{-1.07}$
$D_{0,\parallel}$ $(\mathrm{cm}^2/\mathrm{s})$	8.4E-03	1.0E-02	9.8E-03 (low density) 9.6E-03 (high density)		

E. Formation energies of extrinsic defects in V_2C

As a first step to determining the diffusion behavior of solute atoms in V_2C, the defect formation energies are calculated to determine the site preference for each atomic species. The elements chosen for the calculations are U representing a major component of the fuel, Nd and Ce representing typical fission products and Fe and Ni representing major components of the cladding. The most likely sites for a solute atom to occupy are a vanadium site or one of the vacant octahedral interstitial sites. Electronic structure calculations show V_2C is metallic (see Sec. A), so the defects will be charge neutral. The formation energy for a neutral defect X is given by Eq. 2. The chemical potentials used in our calculations are those of the pure elements in their ground state crystal structures: *bcc* V, *fcc* Ni, *bcc* Fe, *fcc* Ce, *dhcp* (double hexagonal close-packed) Nd and orthorhombic U.

Table 9-9. Theoretical equilibrium lattice constants, cohesive energies and magnetic moments for elemental Ni, Fe, Ce, Nd and U, which represent typical fuel, fission product and cladding components, respectively. Deltas signify percent differences from experiment.

	Ni	**Fe (α)**	**Ce (α)**	**Nd (α)**	**U (α)**
Structure	*fcc*	*bcc*	*fcc*	*Dhcp*	*ortho*
a (Å)	3.517	2.835	4.713	3.708	2.802
Δ	-0.19%	-1.11%	-2.82%	1.35%	-1.80%

b (Å)	-	-	-	-	5.843
Δ	-	-	-	-	-0.45%
c (Å)	-	-	-	11.906	4.905
Δ	-	-	-	0.92%	-1.01%
E_0 (eV/atom)	-5.468	-8.237	-5.923	-4.713	-11.138
mag (μ_B)	0.62	2.23	-	-	-
Δ	2.30%	0.50%	-	-	-

The equilibrium properties of the ground state crystals of the elemental solids listed above as well as their high-temperature allotropes were calculated using both GGA-PBE and LDA exchange-correlation functionals. The GGA-PBE functional correctly predicts the relative energies of each of the allotropes for each element, whereas LDA incorrectly predicts *fcc* Fe to have a lower energy than *bcc* Fe. Overall the GGA-PBE functional provides better agreement with experiment and is therefore used in the remainder of the calculations on extrinsic defects and solute diffusion. The calculated values for the zero-temperature equilibrium properties for the ground state structure of each element along with their differences from experiment are given in Table 9-9. The calculated magnetic moments for the ferromagnetic elements (Fe and Ni) are also provided along with their differences from experiment.

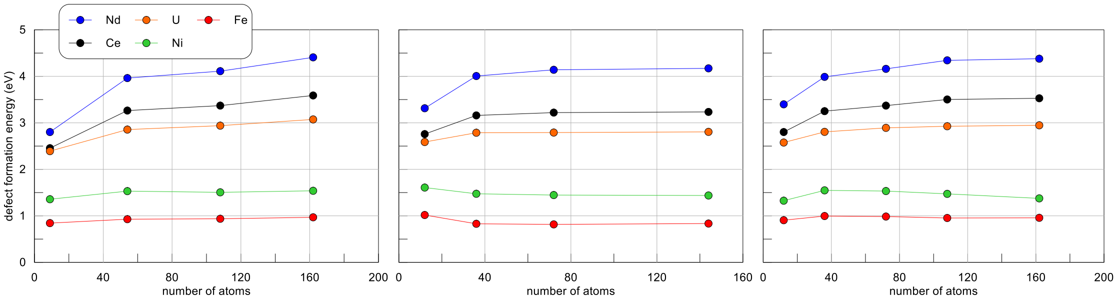

(a) **(b)** **(c)**

Figure 9-12. Defect formation energies for X (=Nd, Ce, U, Ni, Fe) on a vanadium site versus the number of atoms in the supercell for the (a) β*'* phase, (b) α phase and (c) other low-energy orthorhombic structure (SG: *Pnnm*) calculated using density functional theory.

Because the DFT calculations are periodic, the defect atom will interact with its images in neighboring cells. Fortunately, the host material is metallic and so long-range electrostatic interactions will be screened fairly effectively over short distances. This leads to rapid convergence of the defect formation energies with respect to supercell size. Calculated defect energies plotted against the total number of atoms in the supercell are shown in Fig. 9-12 for the vanadium site defect location and in Fig. 9-13 for the interstitial site defect location. Supercells containing ~100 atoms are large enough to converge the defect formation energies to within 0.1 eV.

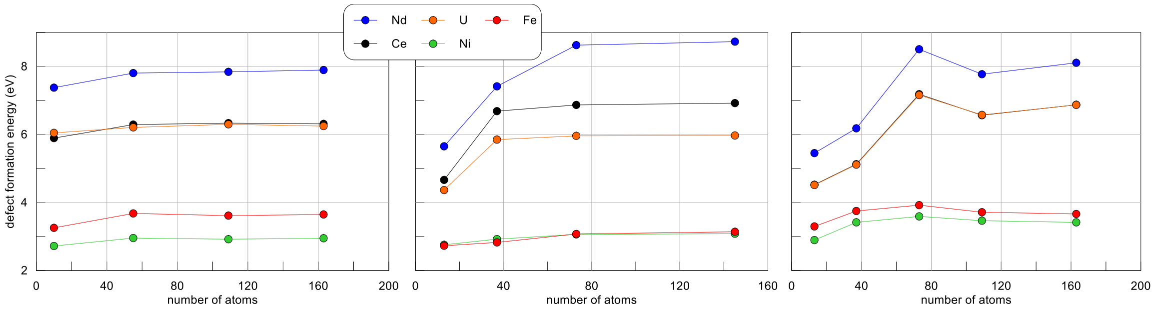

(a) **(b)** **(c)**

Fig 9-13. Defect formation energies for *X* (=Nd, Ce, U, Ni, Fe) on an empty octahedral interstitial site versus the number of atoms in the supercell for the (a) β*'* phase, (b) α phase and (c) other low-energy orthorhombic structure (SG: *Pnnm*) calculated using density functional theory.

The defect formation energies for both the vanadium and interstitial site locations are plotted in Fig. 9-14 as a function of the radius of the defect atom, where the radius is determined based on the calculated equilibrium lattice constants in Table IX. For all atomic species, the vanadium site is energetically favored over the interstitial site. In general, larger defect atoms lead to larger formation energies with the largest atom Nd having a formation energy ~4 times more than the smallest atom Fe for the vanadium site location. The exceptions to this trend are Fe and Ni for the interstitial site location, where the formation energy actually decreases going from the smaller Fe atom to the larger Ni atom, and U and Ce for the vanadium site location, where the formation energy decreases going from the smaller U atom to the larger Ce atom. The latter instance is only observed for the orthorhombic V_2C structure with *Pnnm* symmetry.

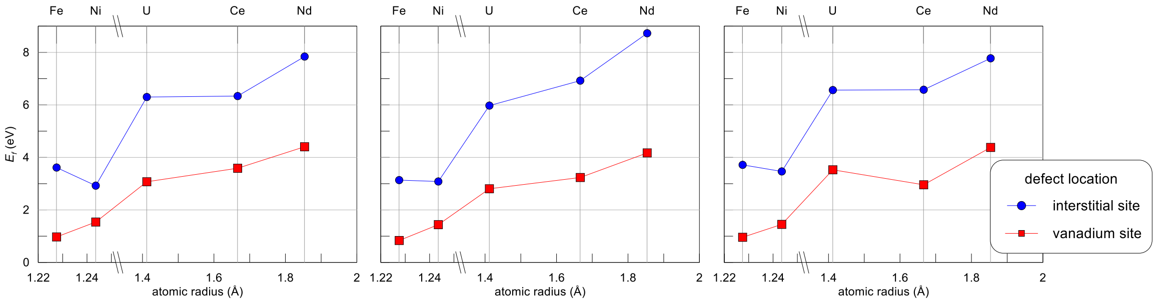

(a) **(b)** **(c)**

Fig 9-14. Defect formation energies as a function of the radius of the defect atom for the (a) β*'* phase, (b) α phase and (c) other low-energy orthorhombic structure (SG: *Pnnm*) calculated using density functional theory.

The next step towards determining the solute diffusion behavior will be to calculate the minimum energy paths for the different jumps that can occur between the defect atom and a vanadium site vacancy. Since the vanadium sublattice is *hcp* for the β*'* phase and approximately *hcp* for the two orthorhombic systems, these calculations will make us of the work done on impurity diffusion in Mg [29] as well as the general first-principles method for calculation of diffusion coefficients described in Refs. [30–33].

10. References

[1] R.L. Klueh, A.T. Nelson, J. Nucl. Mater., 371 (2007) 37-52.

[2] A.B. Cohen, H. Tsai, L.A. Neimark, J. Nucl. Mater., 204 (1993) 244-251.

[3] D.D. Keiser, J.I. Cole, TMS letter, 2 (2005) 79-80.

[4] G. L. Hofman, A. G. Hins, D.L. Porter, L. Lefbowitz, E.L. Wood, in: International Conference on Reliable Fuels for Liquid Metal Reactors, Tucson, Arizona, 1986.

[5] D. Olander, J. Nucl. Mater., 389 (2009) 1-22.

[6] S.T. Zegler, C.M. Walter, AIME Nuclear Metallurgy Symposium on Plutonium Fuels Technology, 13 (1967) 335.

[7] D.D. Keiser, J.I. Cole, in, 2006.

[8] D.D. Keiser, J.I. Cole, in, 2007.

[9] A. B. Cohen, T.C. Wiencek, H. Tsai, in, 1994.

[10] M. Mohammadian, e.a. K. Sridharan, in: American Nuclear Society Annual Conference, Nuclear Fuels and Structural Materials Meeting, San Diego, 2010.

[11] W.-Y. Lo, Y. Yang, J. Nucl. Mater., 451 (2014) 137-142.

[12] W. Yan, W. Wang, Y.Y. Shan, K. Yang, Front. Mater. Sci., 7 (2013) 1.

[13] L. Poirier, O. Richard, M. Ducarroir, M. Nadal, F. Teyssandier, F. Laurent, Thin Solid Film, 249 (1994) 62.

[14] K.L. Choy, Prog. Mater Sci., 48 (2003) 57-170.

[15] M.A. Dayananda, D.A. Behnke, Scripta Metallurgica et Materialia, 25 (1991) 2187-2191.

[16] F. Khatkhatay, J. Jian, L. Jiao, Q. Su, J. Gan, J.I. Cole, H. Wang, J Alloy Compd, 580 (2013) 442-448.

[17] L. Poirier, O. Richard, M. Ducarroir, M. Nadal, F. Teyssandier, F. Laurent, O. Cyr-Athis, R. Choukroun, L. Valade, P. Cassoux, Thin Solid Films, 249 (1994) 62-69.

[18] D. Laverde, T. Gómez-Acebo, F. Castro, Corrosion Science, 46 (2004) 613-631.

[19] L. Poirier, F. Teyssandier, C. Danjoy, L. Valade, F. Sibieude, A. Reynes, J.L. Jauberteau, J. Anal. Appl. Pyrolysis, 36 (1996) 121-136.

[20] D.I. Fotiadis, S. Kieda, K.F. Jensen, J. Cryst. Growth, 102 (1990) 441-470.

[21] D.D. Keiser Jr, J.I. Cole, in: Proceedings of GLOBAL 2007 conference on advanced nuclear fuel cycles and systems, 2007.

[22] D.D. Keiser Jr, J.I. Cole, in: Nuclear Fuels and Structural Materials for the Next Generation Nuclear Reactors, American Nuclear Society Embedded Topical Meeting, Reno, NV, 2006.

[23] H.-S. Choi, S.-W. Rhee, Journal of Electrochemical Society, 141 (1994) 475-479.

[24] L. Djomeni, T. Mourier, S. Minoret, S. Fadloun, F. Piallat, S. Burgess, A. Price, Y. Zhou, C. Jones, D. Mathiot, S. Maitrejean, Microelectronic Engineering, 120 (2014) 127-132.

[25] J. Van den Bosch, A. Almazouzi, G. Mueller, A. Rusanov, Journal of Nuclear Materials, 415 (2011) 276-283.

[26] T.R.G. Kutty, S.K. Rakshit, A. Laik, A. Kumar, H.S. Kamath, C.B. Basak, Journal of Nuclear Materials, 412 (2011) 53-61.

[27] Y. Lee, T.J. McKrell, M.S. Kazimi, Nuclear Engineering and Technology, 45 (2013) 811-820.

[28] E. Rudy and C. E. Brukl, J. Am. Ceram. Soc. **50**, 265 (1967).

[29] V. N. Lipatnikov, Russ. Chem. Rev. **74**, 697 (2005).

[30] O. N. Carlson, a. H. Ghaneya, and J. F. Smith, Bull. Alloy Phase Diagrams **6**, 115 (1985).

[31] S. T. Oyama, *The Chemistry of Transition Metal Carbides and Nitrides* (Springer Science & Business Media, 1996).

[32] K. Yvon, W. Rieger, and H. Nowotny, Monatshefte Für Chemie/Chemical Mon. **97**, 689 (1966).

[33] M. P. Arbuzov, V. G. Fak, and B. V Khaenko, Izv. Akad. Nauk SSSR, Neorg. Mater **12**, 846 (1976).

[34] W. Xing, F. Meng, and R. Yu, Sci. Rep. **6**, 21794 (2016).

[35] X. Chong, Y. Jiang, R. Zhou, and J. Feng, RSC Adv. **4**, 44959 (2014).

[36] L. Wu, T. Yao, Y. Wang, J. Zhang, F. Xiao, and B. Liao, J. Alloys Compd. **548**, 60 (2013).

[37] K. Yvon, H. Nowotny, and R. Kieffer, Monatshefte Für Chemie/Chemical Mon. **98**, 34 (1967).

[38] R. Hill, Proc. Phys. Soc. Sect. A **65**, 349 (2002).

[39] N. W. Ashcroft and N. D. Mermin, *Solid State Physics* (Saunders College, 1976).

[40] S. Lany and A. Zunger, Model. Simul. Mater. Sci. Eng. **17**, 84002 (2009).

[41] C. Freysoldt, B. Grabowski, T. Hickel, J. Neugebauer, G. Kresse, A. Janotti, and C. G. Van De Walle, Rev. Mod. Phys. **86**, 253 (2014).

[42] M. Hagen, Philos. Mag. A **77**, 447 (1998).

[43] C. G. Van De Walle and J. Neugebauer, J. Appl. Phys. **95**, 3851 (2004).

[44] M. T. Dove, *Introduction to Lattice Dynamics* (Cambridge University Press, 1993).

[45] M. Mantina, Y. Wang, R. Arroyave, L. Q. Chen, Z. K. Liu, and C. Wolverton, Phys. Rev. Lett. **100**, 1 (2008).

[46] S. Ganeshan, L. G. Hector, and Z. K. Liu, Comput. Mater. Sci. **50**, 301 (2010).

[47] M. Mantina, Mater. Sci. Eng. **PhD**, 252 (2008).

[48] J. G. Mullen, Phys. Rev. **124**, 1723 (1961).

[49] B. B. Yu and R. F. Davis, J. Phys. Chem. Solids **42**, 83 (1981).

[50] S. Sarian, J. Appl. Phys. **40**, 3515 (1969).

[51] L. V. Azároff, J. Appl. Phys. **32**, 1658 (1961).

[52] L. V. Azároff, J. Appl. Phys. **32**, 1663 (1961).

[53] S. Sarian, J. Phys. Chem. Solids **33**, 1637 (1972).

[54] B. B. Yu and R. F. Davis, J. Phys. Chem. Solids **40**, 997 (1979).

[55] B. C. Zhou, S. L. Shang, Y. Wang, and Z. K. Liu, Acta Mater. **103**, 573 (2016).

[56 M. Mantina, Y. Wang, L. Q. Chen, Z. K. Liu, and C. Wolverton, Acta Mater. **57**, 4102 (2009).

[57] N. Sandberg and R. Holmestad, Phys. Rev. B - Condens. Matter Mater. Phys. **73**, 1 (2006).

[58] S. Huang, D. L. Worthington, M. Asta, V. Ozolins, G. Ghosh, and P. K. Liaw, Acta Mater. **58**, 1982 (2010).

[59] M. Mantina, Y. Wang, R. Arroyave, S. L. Shang, L. Q. Chen, and Z. K. Liu, J. Phys. Condens. Matter **24**, 305402 (2012).

11. Appendix

Publications:

1. S. Huang, W-Y. Lo, and Y. Yang, “Vanadium carbide by MOCVD for mitigating the fuel cladding chemical interaction”, Fusion Engineering and Design, 2017, in press.
2. B J. Demaske, A Chernatynskiy, S. R. Phillpot, “First-Principles Investigation of intrinsic defects and self-diffusion in ordered phases of V2C”, *Journal of Physics: Condensed Matter*, 29, 2017, 245405
3. W-Y Lo, N. Silva, Y. Wu, R. Winmann-Smith and Y. Yang, “Effects of Cr on the interdiffusion between Ce and Fe-Cr alloys”, *Journal of Nuclear Materials*, 458, 2015, 264
4. K. Jeong$_{(g)}$, S. S. Huang, and Y. Yang. 2015. Innovative coating of vanadium carbide on the F/M stainless steel for mitigating fuel cladding chemical interaction. *Transactions of the American Nuclear Society, 113, 2015, 606-607.*
5. W-Y Lo, and Y. Yang, “Vanadium diffusion coating on HT-9 cladding for mitigating the fuel cladding chemical interactions”, *Journal of Nuclear Materials*, 451, 2014, 137
6. W-Y Lo, S Huang, N. Strombom, and Y. Yang, “Low-temperature chemical vapor deposition of vanadium carbide for mitigating the FCCI”, *Transaction of the American Nuclear Society*, 111, 2014, 583-583.

Presentations and Posters:

1. Kookhyun Jeong, and Yong Yang “Nanostructured Vanadium Carbide Coating on the F/M Stainless Steel for Mitigating Fuel Cladding Chemical Interaction”, TMS, February, 2016
2. Kookhyun Jeong, Shaosong Huang, Yong Yang, Innovative Coating of Vanadium Carbide on the F/M stainless steel for mitigating fuel cladding chemical interaction, ANS Winter Meeting, 2015
3. W-Y. Lo, S. Huang, N. Strombom, and Y. Yang**,** “Low-Temperature Chemical Vapor Deposition of Vanadium Carbide for Mitigating the FCCI”, W-Y. 2014 Winter Meeting, November 9-13, 2014 Anaheim, CA
4. W-Y Lo, and Y. Yang, Poster, “Innovative Coating of Nanostructured Vanadium Carbide for Mitigating the Fuel Cladding Chemical Interaction, FCRD Advanced Fuel Campaign, Integration Meeting, INL, August 26-28, 2014